University of Cape Town

Department of Civil Engineering

Computational Continuum Mechanics Research Group

Active Contraction of the Left Ventricle with Cardiac Tissue Modelled as a Micromorphic Medium

Author:
Marina Kamper

Supervisor:
A/Prof Sebastian Skatulla

Thesis presented in partial fulfilment of the requirements for the degree
Master of Science in Engineering.

June, 2019

Declaration of Authorship

I know the meaning of plagiarism and declare that all the work in the document, save for that which is properly acknowledged, is my own. This thesis/dissertation has been submitted to the Turnitin module (or equivalent similarity and originality checking software) and I confirm that my supervisor has seen my report and any concerns revealed by such have been resolved with my supervisor.

Signed: Signed by candidate

Date: 10/03/2019

Acknowledgements

First and foremost, I would like to thank my supervisor, A/Prof Sebastian Skatulla, for all the advice, guidance and patience during my two years at UCT.

To all my postgraduate friends, especially those on the sixth floor, thank you for the fun and interesting lunches, supplying cake during the tea breaks and for always being available for a quick chat. A special thanks to everyone in our research group for all your help and support.

Lastly, a big thank you to my family for your encouragement and never-ending love.

The financial assistance of the National Research Foundation (NRF) of South Africa (Grant Numbers 104839 and 105858) towards this research is hereby acknowledged. Opinions expressed and conclusions arrived at, are those of the author and are not necessarily to be attributed to the NRF.

Abstract

Active Contraction of the Left Ventricle with Cardiac Tissue Modelled as a Micromorphic Medium

Marina Kamper

The myocardium is composed of interconnected cardiac fibres which are responsible for contraction of the heart chambers. There are several challenges related to computational modelling of cardiac muscle tissue. This is due in part to the anisotropic, non-linear and time-dependent behaviour as well as the complex hierarchical material structure of biological tissues.

In general, cardiac tissue is treated as a non-linear elastic and incompressible material. Most computational studies employ the theories of classical continuum mechanics to model the passive response of the myocardium and typically assume the myocardium to be either a transversely isotropic material or an orthotropic material. In this study, instead of a classical continuum formulation, we utilise a micromorphic continuum description for cardiac tissue. The use of a micromorphic model is motivated by the complex microstructure and deformations experienced by cardiac fibres during a heartbeat. The micromorphic theory may be viewed as an extension of the classical continuum theory. Within a micromorphic continuum, continuum particles are endowed with extra degrees of freedom by attaching additional vectors, referred to as directors, to the particles. In this study the directors are chosen such that they represent the deformation experienced by the cardiac fibres.

In addition to the passive stresses, the myocardium experiences active stresses as a result of the active tension generated by cardiac fibres. The active tension in the heart is taken to be a function of the sarcomere length, intracellular calcium concentration and the time after the onset of contraction. Experimental studies show that the active behaviour of the myocardium is highly dependent on the tissue arrangement in the heart wall. With a classical continuum description, the sarcomere length is usually defined as a function of the stretch in the initial fibre direction. To allow for a more realistic description of the active behaviour, we define the sarcomere orientation, and consequently also the sarcomere stretch, as a function of the director field. Furthermore, we use the director field to describe the direction in which contraction takes place.

The intent of this study is to use a micromorphic continuum formulation and an active-stress model to investigate the behaviour of the left ventricular myocardium during a heartbeat. The simulated results presented here correspond well with typical ventricular mechanics observed in clinical experiments. This work demonstrates the potential of a micromorphic formulation for analysing and better understanding ventricular mechanics.

Contents

List of Figures

List of Tables

Chapter 1

Introduction

Computational modelling of biological phenomena has attracted a great deal of attention over the last few decades. It allows researchers to predict the behaviour of complex biological systems and has the advantage that thousands of computational experiments can be performed to investigate the responses of these systems [7].

One of the most important biological structures in the human body is the heart. Computer-based cardiac[1] models provide insight into the interactions between physical phenomena and anatomical structures of the heart and there has been a steady rise in the accuracy and complexity of these models [106]. With the improvement and advent of new imaging modalities, it has become possible to accurately reconstruct the geometry and structure of the human heart. Furthermore, an increase in computer power has led to faster and easier simulations [76].

Extensive computational heart modelling in the last half-century has brought about a variety of cardiac models utilised in different applications. Cardiac models are typically used to simulate the electrical activity and analyse the mechanical performance of the heart or to model the electromechanical coupling in heart fibres, see for example studies conducted by Trayanova [120], Göktepe et al. [41] and Wong et al. [134]. The ultimate goal is to have these models be used in the medical environment to provide guidance to physicians treating heart diseases. The rationale is that individual patients will respond differently to the same clinical intervention. Rather than applying a clinical treatment that suits the average patient, a physician can use a computational model to predict how a patient will respond to a specific intervention [43]. This is referred to as *patient-specific* treatment since a treatment is designed to fit the individual instead of the average patient.

1.1 Background

1.1.1 The Heart and Its Function

The heart is responsible for pumping blood through the cardiovascular system[2]. As blood travels through the body, it supplies the organs with vital nutrients and also assists in the removal of

[1] Cardiac: relating to the heart.

[2] Cardiovascular system: system in the body that circulates blood.

metabolic waste [33]. The heart is composed of two pumps, a right and a left pump [78]. The right pump receives oxygen-poor blood from the body and pumps it to the lungs for the blood to become oxygenated. Oxygen-rich blood travels from the lungs to the left pump from where it is distributed to the rest of the body. As the blood moves through the body its oxygen content decreases and it returns to the right pump for the cycle to repeat. This path of blood flow is vital for survival.

Each pump is composed of an atrium and a ventricle. The two atria are responsible for receiving blood, whereas the two ventricles perform the main pumping action of the heart. By raising the blood pressure, the ventricles are able to distribute the blood through the cardiovascular system. The increase in blood pressure is accomplished by the contraction of interconnected cardiac muscle fibres found in the heart wall. The natural pacemaker of the heart, the sinoatrial node, generates electrical impulses that regulate the contraction of these fibres.

1.1.2 Modelling the Behaviour of Cardiac Tissue

Many studies related to cardiac modelling centre around simulating the behaviour of cardiac muscle tissue. Soft biological tissues, such as cardiac tissue, are anisotropic and heterogeneous materials that display time-dependent and non-linear behaviour [3, 37, 84]. Cardiac muscle fibres may experience changes in lengths of more than 20% during a heartbeat. It is therefore necessary to analyse its behaviour using a large (finite) deformation theory [84].

The mechanical response of cardiac tissue is typically separated into two components, the passive response and the active response. The former is usually described and predicted with the theories of classical continuum mechanics. Within the field of classical continuum mechanics, one neglects the intrinsic microstructure and considers only the macroscopic system [52]. Atomic-scale properties are averaged and the discontinuous atomic and molecular microstructures are replaced by a smooth continuum body. According to Holzapfel [52], a classical continuum is a body composed of a continuous collection of point particles. Figure 1.1(a) illustrates the motion of a classical continuum body from its undeformed state (initial configuration) to its deformed state (current configuration) in the two-dimensional space.

The behaviour of all continua is governed by so-called balance laws, while material models enable us to describe the responses of specific materials [98]. Material models for passive cardiac tissue have been documented extensively in the literature. Initially, the passive response was described with simple isotropic models [22, 81], but more recent analyses employ transversely isotropic materials models [46, 56] or orthotropic materials models [53, 122].

The active component of the mechanical behaviour of cardiac tissue may be included in a number of ways. The active behaviour or active response refers to the ability of cardiac tissue to generate its own tension and contract when it is electrically stimulated. The contraction of cardiac tissue occurs as a result of a series of phenomena that take place on different length scales. To avoid over-complexity, an active model should yield results that are in line with experimental observations, but not explicitly include all the underlying mechanics [100]. The most common approach to incorporate the active response in a continuum formulation is with an *active-stress* model [2]. With this approach the stress experienced by the heart wall is additively decomposed into active and passive components and the active component is then simply included in the balance laws [2].

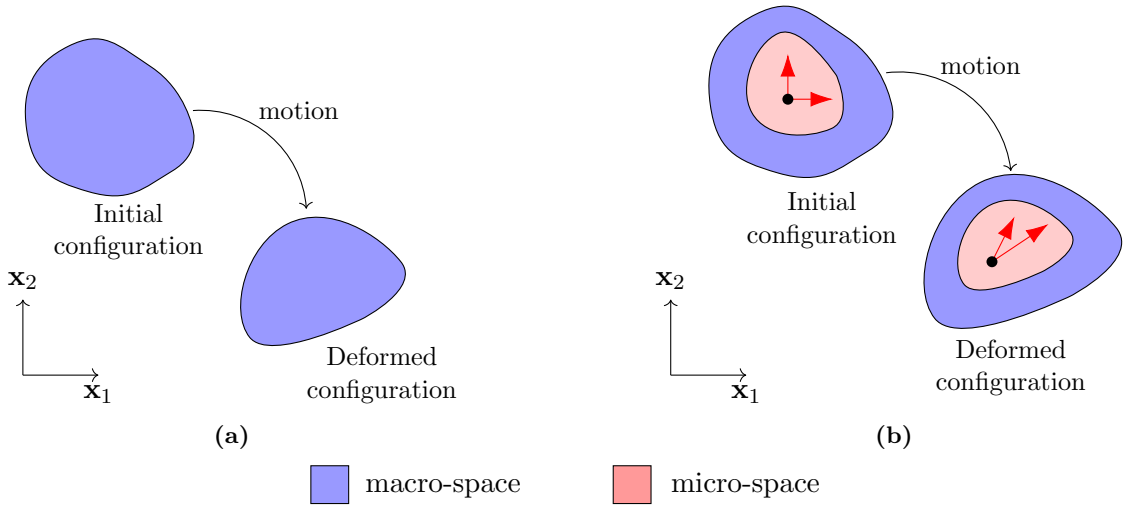

Figure 1.1: The difference between (a) the classical continuum that consists of a collection of point particles and (b) the micromorphic continuum composed of deformable particles.

1.1.3 Classical Continuum Theories vs Microcontinuum Modelling

Although the theories of classical continuum mechanics are valid for a wide range of scientific and engineering problems, there are a number of cases in which a classical theory will produce inadequate results. Classical continuum theories will fail to accurately predict the response of a body whose characteristic length is comparable to the size of the body constituents. This is because these constituents may have individual responses that differ from the overall response of the body [26]. One such example is the flow of blood through capillaries. The size of the capillaries (characteristic length) is of the same order as the size of cells found in blood. The use of a classical continuum formulation to describe this behaviour yields results that are not in agreement with experimental observations. Other cases in which classical continuum mechanics might give unsatisfactory results include modelling materials such as foams, solids with micro-cracks, bones and materials with large porous structures [28].

To overcome some of the drawbacks, classical continuum theories can be extended to so-called *microcontinuum* theories where, instead of having infinitesimally small point particles, a continuum consists of a set of *deformable* particles. This is achieved by attaching additional vectors (also referred to as *directors*) to the point particle, as illustrated by the red vectors in Figure 1.1(b). These vectors represent the deformation of the particle and as the microcontinuum experiences deformation, the directors also deform. The benefit is that a microcontinuum model takes into account material properties on the micro-scale and therefore gives further insight into multiscale phenomena.

One of the first studies to propose the idea of deformable particles was conducted by the Cosserat brothers [18]. To include characteristics of the material microstructure, the Cosserat brothers introduced the concept of a rigid micro-particle. In this formulation a continuum particle is endowed with three additional degrees of freedom to describe the rotation of the particle. Therefore, the particle is able to experience macroscopic displacement as well as micro-rotation. Materials that exhibit this type of behaviour are referred to as *micropolar* or *Cosserat* continua.

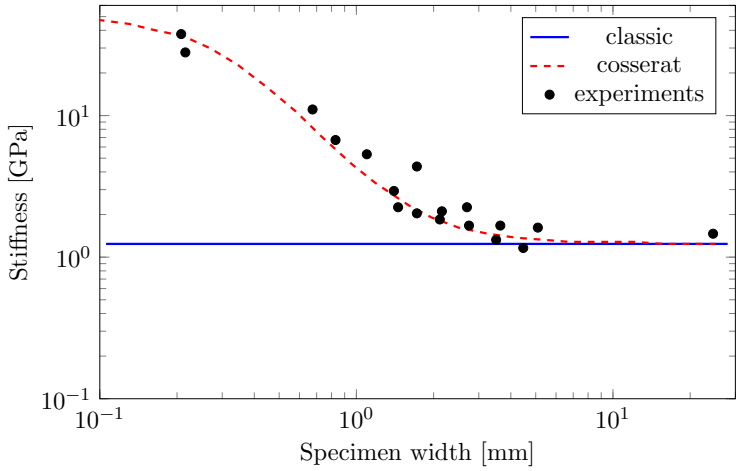

Figure 1.2: A collection of several datasets where the shear stiffness of bone were experimentally obtained using different sample sizes, adapted from [11].

The micropolar theory is fairly popular in bone mechanics [28, 90, 105, 138]. Bone, like cardiac tissue, has a hierarchical material structure. At the millimetre-scale, bone appears to be a homogeneous material, but if one considers scales closer to the micron-scale, the heterogeneous structure becomes more evident [77]. Figure 1.2 presents experimental results from torsional testing performed on bone samples. The torsional stiffness of bone was obtained from specimens with different diameters. With bigger specimen samples, the stiffness is fairly well predicted by classical continuum mechanics. The reason is that as the specimen size becomes larger, the heterogeneity on the micro-scale becomes less dominant [77]. However, if one considers smaller sample sizes, the predicted classical stiffness deviates significantly from the actual stiffness. This is because the classical theory is only valid if the size of the micro-constituents is much smaller than the specimen size [11]. Since a micropolar formulation accounts for size-dependent material responses, it performed much better in predicting the torsional stiffness. The figure clearly demonstrates the advantage of a microcontinuum formulation.

Apart from the micropolar theory, there are two other subclasses of microcontinuum theories, namely *microstretch* and *micromorphic*. A subclass is based on the constraints placed on the deformation of the particle [27]. In the case of a microstretch medium, a continuum particle is allowed to experience micro-rotation and micro-stretch. In the more general case of a micromorphic material, a particle is allowed to experience micro-rotation, micro-stretch as well as micro-shear.

1.2 Aims and Objectives

In this work we investigate the behaviour of a healthy heart, more specifically its bio-mechanical behaviour, i.e. we study the deformations and stresses experienced by the heart wall during a heartbeat. The left ventricle has to sustain much higher pressures compared to the right ventricle and is considered by some to be of higher importance [13]. Moreover, right ventricular infarction[3] is very rare. Therefore, this study, like many other computational studies of the heart, focuses on the left ventricle.

[3]Myocardial infarction (known as a heart attack): a sudden event when cardiac muscle is deprived of blood [78].

We propose the use of a micromorphic formulation to model the behaviour of a patient-specific left ventricle. A micromorphic model allows us to include features of the microstructure and to model relative deformation between the cardiac fibres and the surrounding tissue. Microcontinuum modelling has only recently been extended to modelling the responses of soft biological tissue, see for example Sack et al. [108], Thurieau et al. [118] and Von Hoegen et al. [129]. This work, therefore, aims to investigate whether a micromorphic model is suitable for describing the behaviour of cardiac tissue.

The layout and orientation of cardiac muscle fibres in the heart wall have a significant effect on the mechanical response and deformation of the heart [121]. With a micromorphic model, this project aims to capture more realistic responses of the left ventricle during the different stages of a heartbeat. In this work one micro-director is defined for each continuum particle and the directors are chosen to align with the cardiac fibres. The directors in a micromorphic medium are allowed to distort [32], and therefore this formulation provides additional information about the deformation experienced by cardiac fibres.

A micromorphic material model that describes passive cardiac tissue has previously been implemented by the Computational Continuum Mechanics (CCM) Research Group at the University of Cape Town, see [24]. The main goal of this project is to develop and implement an active-stress model that couples with the existing micromorphic model. To this end, we define the following objectives:

1. Review the literature on the mechanical behaviour of the heart, including constitutive models, heart geometries and the physiology of a healthy heart.
2. Develop and implement an active contraction model on SESKA, an in-house finite element software, that can be used together with the existing micromorphic model to simulate the mechanical behaviour of cardiac tissue. The main task is to determine the additional contributions to the finite element stiffness matrix and force vectors.
3. Perform simulations on SESKA:
   (a) Simulate a heartbeat by applying applicable boundary and loading conditions.
   (b) Calibrate the material model to match experimental pressure-volume data.
   (c) Examine the deformation of the left ventricle and the ventricular wall stresses.
4. Determine the suitability of the micromorphic model by comparing the results to a heart simulation that uses a classical continuum formulation.

1.3 Thesis Outline

The thesis is structured as follows. In Chapter 2 the physiology of a healthy heart is discussed. While we largely consider the macroscopic structure and mechanics of the heart, we also look at the structure and behaviour of cardiac tissue at lower scales. Chapter 3 outlines the theories of classical continuum mechanics and introduces important terminology and nomenclature that are used throughout the remainder of this work. Additionally, Chapter 3 briefly explains the finite element procedure used when dealing with non-linear elastic materials. A number of cardiac models, including passive and active models, are reviewed in Chapter 4. The evolution of heart

geometries used in computational models is also addressed. Chapter 5 serves as a basic introduction to the subject of micromorphic modelling and presents a constitutive model for passive cardiac tissue. Chapter 6 provides the formulation of an active-stress model. The objective is to adapt a model documented in the literature and make it compatible with the existing micromorphic model. Chapter 7 explains the methodology used to simulate the different phases of the heart cycle and briefly explains how the ventricular geometry was reconstructed from magnetic resonance images. In Chapter 8 we present the results from the micromorphic model and the classical continuum model. Finally, the thesis is concluded in Chapter 9 with a summary and suggestions for future work.

Chapter 2

Heart Physiology

This chapter reviews the workings of a healthy heart, including the mechanics of the ventricles, the different phases of the cardiac cycle, the layout of cardiac tissue in the heart wall and the contraction of cardiac fibres. The purpose is to present the medical nomenclature that is relevant to subsequent chapters.

2.1 Gross Structure of the Heart

The heart is often described as a muscular pump with its main purpose being to supply the organs of the body with blood [9, 65, 123]. Oxygen-rich blood provides cells with food while at the same time also removing left-over products from metabolic processes [33].

Figure 2.1 presents a cross-sectional view of the human heart. This muscular organ, located between the two lungs, consists of four chambers: the right and left atria and the right and left ventricles. The interventricular septum, a thick muscular wall, separates the two ventricles. Together the right atrium and right ventricle form the right pump of the heart and similarly the left atrium and left ventricle serve as the left pump.

Four one-way valves are found in the heart. The mitral valve and tricuspid valve, also referred to as the atrioventricular valves, separate the two atria from their adjoining ventricles. In a healthy heart, these valves permit blood flow in one direction only (from the atrium to its ventricle), thereby preventing blood from flowing back into the atria. The semilunar valves, the pulmonary valve and the aortic valve, open to allow blood flow away from the ventricles to the body.

2.2 Circulation of Blood

As blood travels through the body it becomes partially depleted of oxygen. The oxygen-depleted blood returns to the heart and enters the right atrium at a low pressure. The blood passes from the atrium through the tricuspid valve into the right ventricle. Contraction of the right ventricle increases the blood pressure and the blood is ejected into the pulmonary artery. The pulmonary arteries transfer the blood to the lungs where it is enriched with oxygen. Pulmonary veins then return the blood to the left atrium. The blood moves through the left atrium and mitral valve and fills the left ventricle. The ventricle contracts and blood is ejected into the aorta from where it is

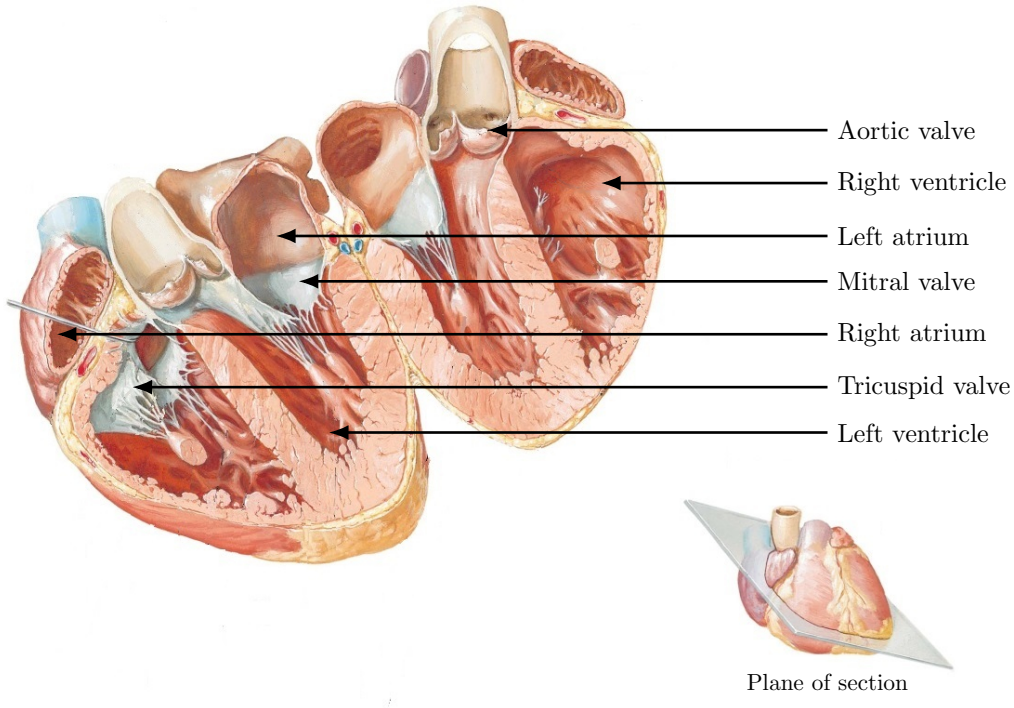

Figure 2.1: Cross-section of the human heart showing the four heart chambers, adapted from [85].

transported to the rest of the organ system. The phase in which the relaxed ventricles fill with blood is referred to as diastole and the phase in which the ventricles contract is termed systole.

The cardiovascular system can be separated into two main circulation loops: the pulmonary circuit and the systemic circuit. The pulmonary circuit is the path of blood as it moves from the right ventricle to the lungs and back to the left atrium. Blood passes through the systemic circuit as it travels from the left ventricle to the rest of the body and returns to the right atrium. The right ventricle is responsible for blood flow in the pulmonary circuit and likewise the left ventricle pumps blood through the systemic circuit.

2.3 Ventricular Mechanics

The main pumping power of the heart is supplied by the ventricles and as a result the ventricular walls are subjected to pressures that are much higher than the pressures experienced by the atrial walls. In this section we consider the function of the ventricles, specifically the pressure and volume changes during a heartbeat.

2.3.1 Ventricular Geometry

The idealised shape of the left ventricle is similar to an elongated ellipsoid truncated at its top, while the right ventricle forms a crescent-like shape around the left ventricle [62, 84, 110]. Since the ventricles develop higher pressures than the atria, the heart wall surrounding the ventricles is much thicker compared to that surrounding the atria [84]. Overall, the heart wall is thickest in the

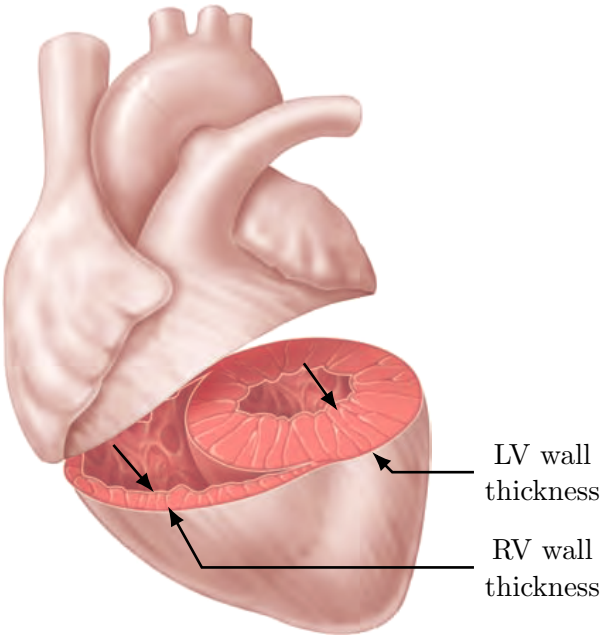

Figure 2.2: Cross-sectional view of the two ventricles illustrating the difference in wall thickness of the left ventricle (LV) and the right ventricle (RV), adapted from [78].

left ventricle, as illustrated in Figure 2.2. This is because the left ventricle is responsible for blood flow in the systemic circuit. The systemic circuit offers greater resistance to blood flow than the pulmonary circuit. The left ventricle has to develop high pressures to overcome this resistance and as a result left ventricular pressure at the end of contraction is about three times as high as the pressure in the right ventricle [62]. The thick wall of the left ventricle ensures that the ventricle can sustain these high pressures.

2.3.2 Pressure-Volume Relationship

The pressure-volume loop shown in Figure 2.3 provides the relationship between the cavity volume and cavity pressure of a ventricle. It is a simple method to represent a full heartbeat. The curve is divided into four distinct phases namely (i) diastolic filling, (ii) isovolumetric contraction, (iii) ejection and (iv) isovolumetric relaxation.

At the start of diastolic filling (point A), the atrioventricular valve (inlet valve) of the ventricle opens and blood enters the chamber from the atrium. Ventricular filling continues until the ventricle reaches its final volume, known as the end-diastolic volume (EDV). At this point the atrioventricular valve closes, preventing any blood from further entering the ventricle. Point B marks the beginning of isovolumetric contraction. An electrical impulse activates the cardiac fibres and causes the ventricle to contract. Because the inlet and outlet valves are closed, the ventricular volume remains constant. This phase is also characterised by a rapid increase in pressure. Once the pressure in the ventricle reaches that of the great artery, the semilunar valve (outlet valve) opens. Blood is ejected into the artery from where it is distributed to the body. The closing of the semilunar valve marks the end of ejection (Point D). At the end of ejection the ventricular volume is at its lowest. This volume is known as the end-systolic volume (ESV). After the closing of the semilunar valve, the ventricle relaxes while its volume remains constant. The ventricular

pressure decreases until it is below that of the atrium. The pressure difference between the atrium and ventricle causes the atrioventricular valve to open. The opening of the inlet valve allows blood to flow into the ventricle and indicates the start of a new cycle. It is important to note that the pressure-volume curves for the left and right ventricles are similar in shape. However, the pressure and volume values of points A through D are different for the two ventricles.

The stroke volume (SV) is defined as the difference between the end-diastolic volume and end-systolic volume,

$$\mathrm{SV} = \mathrm{EDV} - \mathrm{ESV}\,. \tag{2.1}$$

The stroke volume is an important measurement to determine cardiac output [65]. The ejection fraction (EF) is a popular measure of ventricular function. It is the amount of blood ejected divided by the end-diastolic volume, that is

$$\mathrm{EF} = \frac{\mathrm{SV}}{\mathrm{EDV}}\,. \tag{2.2}$$

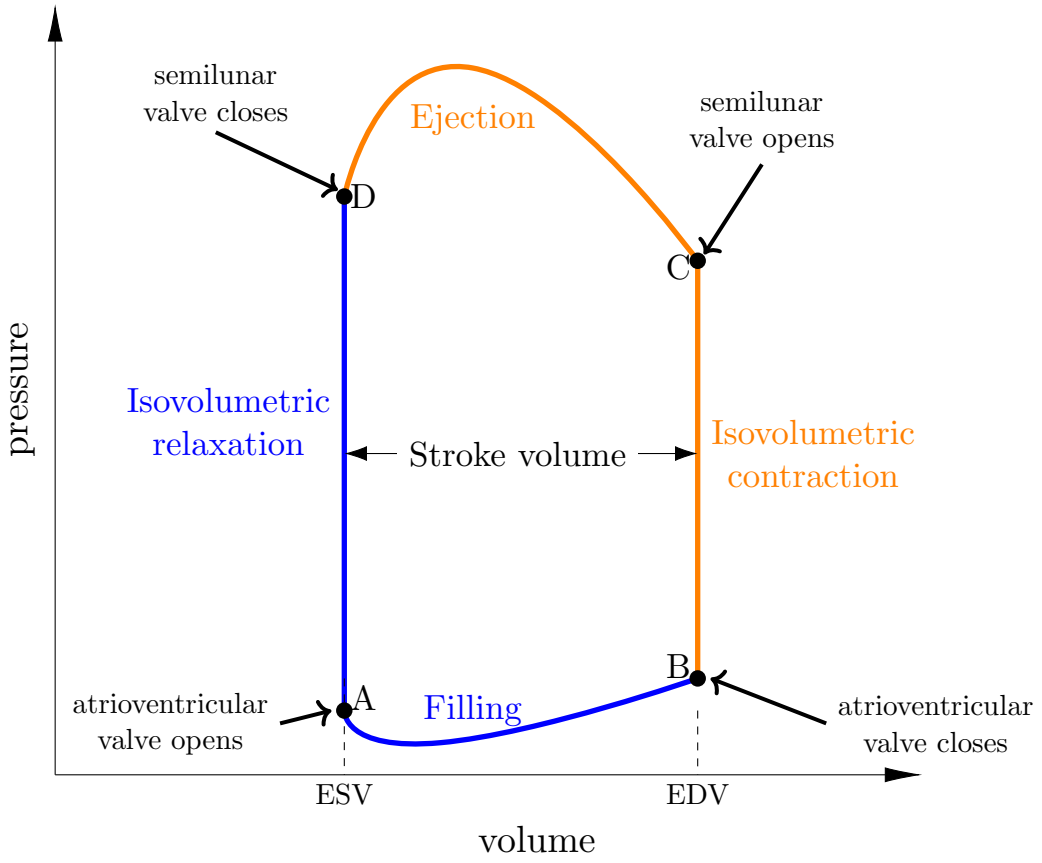

Figure 2.3: The pressure-volume relationship for the ventricle consists of four distinct phases. Diastole, indicated in blue, refers to the period during which the ventricle relaxes and subsequently fills. Systole, denoted in orange, comprises the contraction and ejection phases.

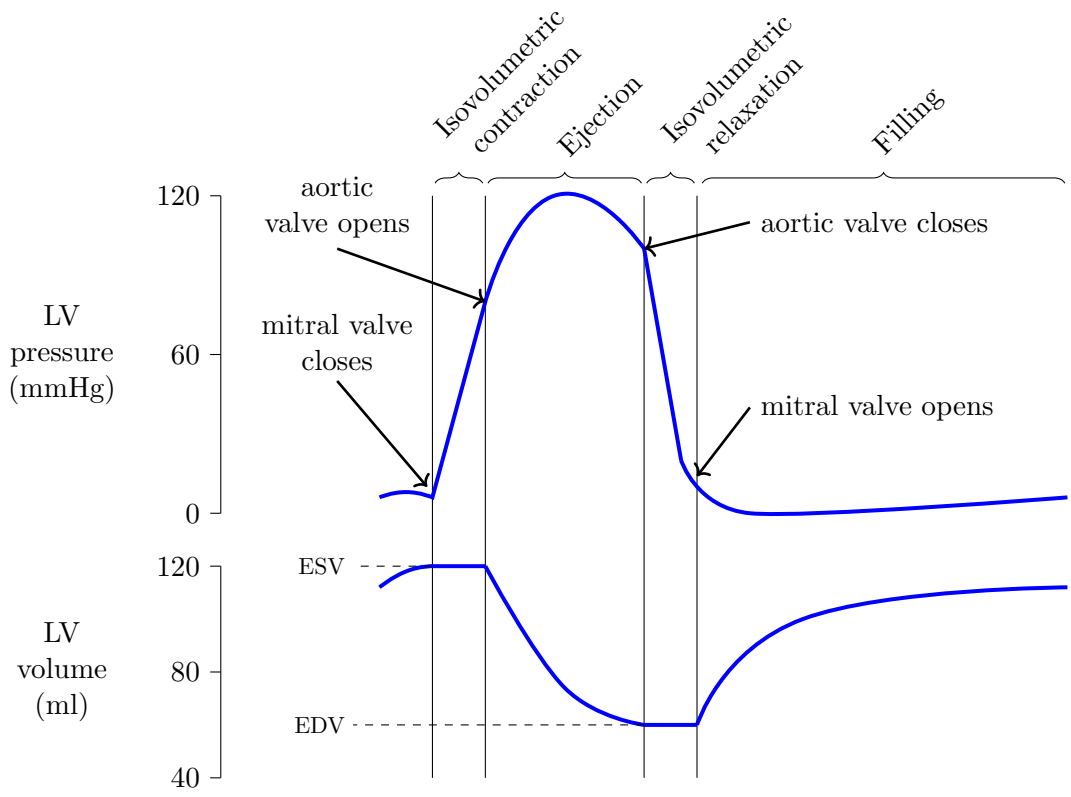

Figure 2.4: Variation in the left ventricular (LV) pressure and volume over time.

Figure 2.4 presents the temporal variation in the pressure and volume of the left ventricle. Similar to the pressure-volume loop, Figure 2.4 is divided into the four phases of the cardiac cycle, that is ventricular filling, isovolumetric contraction, ejection and isovolumetric relaxation. From Figure 2.4 we see that isovolumetric contraction and relaxation occur over relatively short time periods while the period of ventricular filling is the longest phase of the cardiac cycle.

2.3.3 Ventricular Motion

During systole the walls of the ventricles thicken [115] and the left ventricle makes a twisting motion about its long axis [82, 110]. Buchalter et al. [8] used magnetic resonance image tagging to measure the torsion experienced by the left ventricle. They found that when viewed from the apex the ventricle experiences a counterclockwise rotation, as seen in Figure 2.5. Studies have also observed longitudinal displacement of the ventricular base [104]. The base moves down towards the apex, causing a decrease in the distance between the base and apex. This results in an overall long-axis shortening of the ventricles. Additionally, Codreanu et al. [17] observed an upward motion of the apex during systole.

In early diastole, the ventricles begin to relax [65] and the left ventricle untwists [96]. As the ventricles fill with blood, they expand, the ventricular walls move outward and the distance between the apex and the base increases. The ventricular motions during systole and diastole may be explained by the arrangement of cardiac fibres in the heart wall [17].

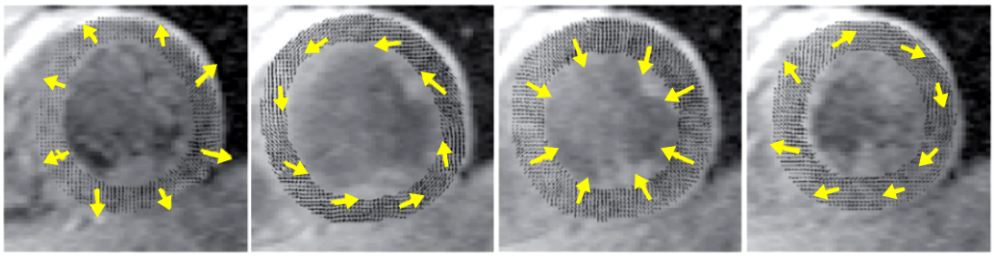

Figure 2.5: Short axis images of the mid-ventricle from [61] showing the motion of the left ventricle during diastolic filling, isovolumetric contraction (IVC), ejection and isovolumetric relaxation (IVR). Arrows represent the in-plane velocity field of the ventricle.

2.4 Cardiac Muscle Tissue

The wall of the heart is divided into three layers: the endocardium, myocardium and epicardium [62]. The endocardium (*endo* = within) is the thin inner layer of the heart wall. It is a serous membrane that lines the inside of the atria and ventricles. The thick middle layer, or myocardium (*myo* = muscle), consists of contracting muscle tissue and makes up the largest part of the heart wall. Cardiac muscle fibres are joined together to form the complex structure of the myocardium and it is these fibres that are responsible for the pumping action of the heart. The myocardium has a non-uniform thickness: it is thickest in the left ventricle and thinnest in the atria. The final layer, the epicardium (*epi* = above), forms the thin outer layer of the heart wall.

2.4.1 Structure of Cardiac Tissue

The three major types of muscle tissue found in the body are skeletal, smooth and cardiac muscle tissue. The latter is found only in the heart [33]. Cardiac muscle tissue consists of short branched cardiac muscle fibres, also referred to as cardiac muscle cells or myocytes. The length of a cardiac muscle fibre varies between 80 and 100 μm while its diameter ranges from 10 to 20 μm.

The fibres are connected at intercalated discs, which appear as dark lines under a microscope, see Figure 2.6. Because intercalated discs form a mechanical and electrical connection between adjacent cells, the myocardium functions as a single unit [33]. Figure 2.6 also shows the striated appearance (alternating light and dark lines) of cardiac muscle tissue. The light and dark lines are referred to as I-bands and A-bands respectively.

A single muscle fibre consists of subunits called fibrils. The striated appearance of the muscle tissue is a result of different filaments found in a fibril. The dark A-bands contain so-called thick filaments, which consist mainly of the protein myosin, while the light I-bands contain thin filaments, composed of the protein actin. The thick filaments cause the darker appearance of the A-band. Figure 2.7 illustrates the hierarchical structure of a cardiac fibre. The dark line in the middle of the I-band is called a Z-line. As indicated in Figure 2.7, a subunit from Z-line to Z-line is referred to as a sarcomere. Titin, a large protein, joins the thick filaments to the Z-lines. The ends of the thin filaments do not stop at the edge of the I-band. Rather, they extend into the A-band and overlap with the thick filaments, as shown in Figure 2.8(a).

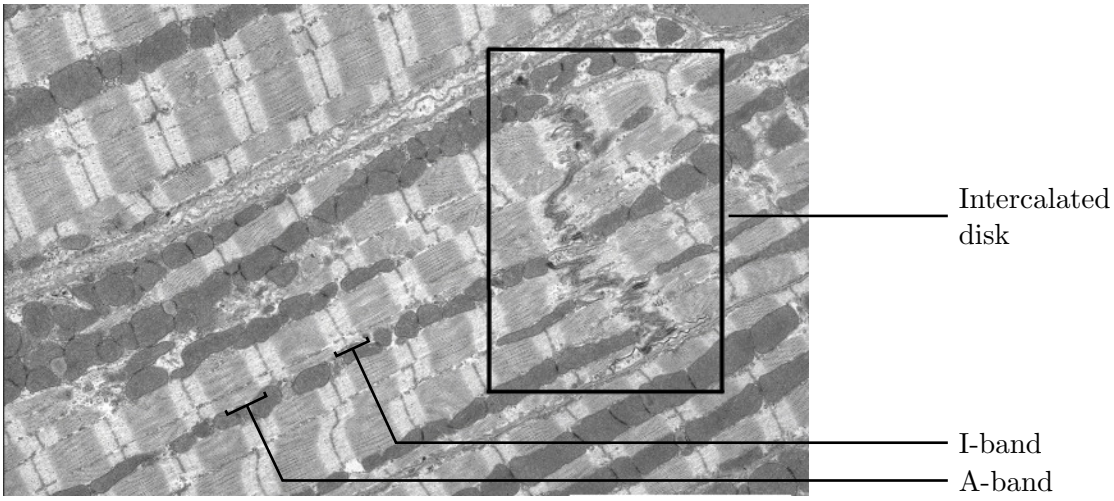

Figure 2.6: Cardiac muscle tissue as seen from under an electron microscope, modified from [89]. The electron micrograph shows the branched shape and striated appearance of cardiac muscle tissue.

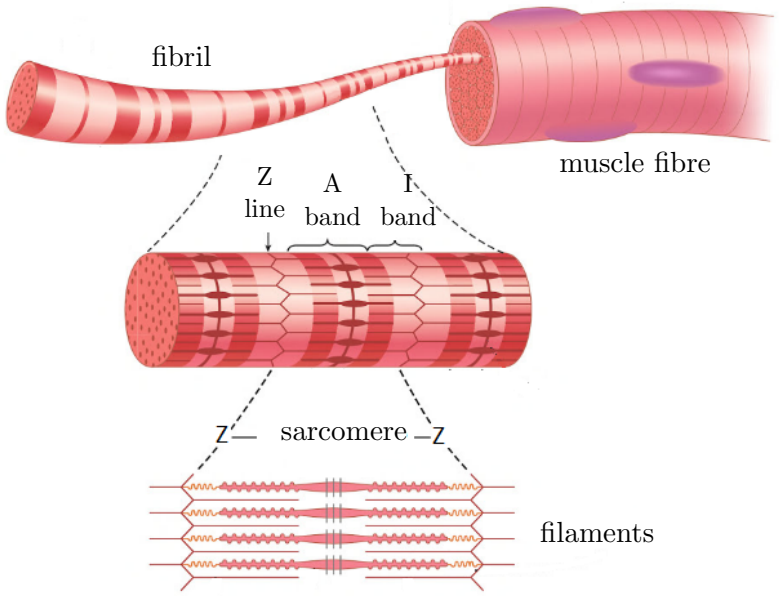

Figure 2.7: Schematic diagram modified from [48] showing the hierarchical structure of muscle tissue. The alternating thick and thin filaments give cardiac muscle tissue its striated appearance. A sarcomere extends form Z-line to Z-line and is the contractile unit of a muscle fibre.

2.4.2 Contraction of Cardiac Tissue

Contraction of muscle tissue is accomplished by the contraction of individual fibres. At the microscopic level, the contraction of fibres is often described with the *sliding filament theory* [33]. To produce fibre contraction, the thin filaments slide further in between the thick filaments, as illustrated in Figure 2.8(a). Because the overlap between the thick and thin filaments increases, the dark A-bands move closer together. It is important to note that the lengths of the filaments remain unchanged. Crossbridges (also referred to as myosin heads), which form part of the thick filaments, pull the thin filaments to achieve this sliding motion. As the distance between neighbouring Z-lines decreases, the sarcomeres and hence the fibrils shorten. The shortening of the fibrils results in the contraction of the muscle fibre.

Contractile proteins in the heart regulate the contraction and relaxation of the cardiac muscle fibres. Apart from actin, thin filaments also contain tropomyosin and the three proteins of the troponin complex, namely troponin-I (TN-I), troponin-T (TN-T) and troponin-C (TN-C). These proteins are shown in Figure 2.8(b). For a fibre to contract, crossbridges have to interact with binding sites on the actin protein. In the relaxed muscle, the tropomyosin is held in position by the troponin complex such that it inhibits the crossbridges from attaching to the thin filaments.

Calcium ions are produced when the fibre is stimulated by an electrical impulse. The calcium ions bind to troponin-C causing the tropomyosin to move away and expose active binding sites for the crossbridges. Conversely, when the calcium ions are removed, the tropomyosin resumes its inhibitory position. It is clear that energy is spent on the micro-scale to obtain deformation on the macro-scale [2].

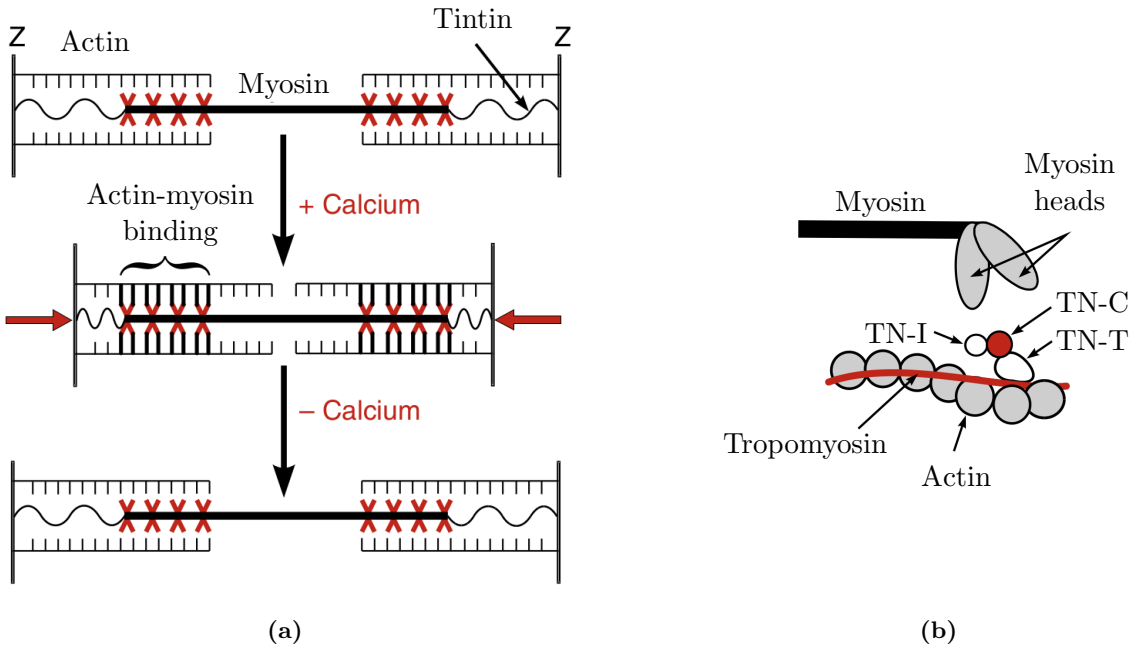

Figure 2.8: Schematic diagrams illustrating (a) the sliding filament theory that is used to explain the mechanics of muscle contraction on the microscopic level and (b) the different proteins found in the muscle filaments, from [65].

2.4.3 Electrical Conduction

To contract, cardiac muscle fibres need to be electrically excited [94]. In a healthy heart, the electrical activity is regulated by the natural pacemaker of the heart, the sinoatrial node, which is located in the right atrium. The sinoatrial node consists of special cells that are capable of generating electrical impulses. The electrical impulse travels from fibre to fibre across the atria causing the right and left atria to contract. The atria are separated from the ventricles through a layer of connective tissue that surrounds the atrioventricular valves. This layer prevents the impulse from travelling directly to the ventricles and special conducting tissue is therefore required [33]. This conducting tissue allows the impulse to travel through the ventricles. The left and right ventricles contract approximately 0.1 to 0.2 seconds after the atria [33].

2.4.4 Tissue Layout in the Ventricles

The cardiac muscle fibres are arranged in a complex pattern in the myocardium. Surrounding the muscle fibres are types I and II collagen, which make up the majority of the extracellular matrix [55]. The organisation of the muscle fibres in the myocardium is often described in one of two ways [40, 53]. The first considers the heart to be one continuous muscle that is coiled into two loops or helices [10]. The second assumes the heart to consist of layers (or sheets) that contain predominately cardiac muscle fibres [140]. The layers are usually three to four fibres thick and are allowed to slide with respect to each other during contraction and filling [73]. Several authors adopt the latter approach, see for example [3, 41, 53, 84]. Figure 2.9 illustrates the layout of fibres in the ventricle and depicts the muscle layers as red lines. A micrograph of cardiac tissue is given in Figure 2.10 and clearly shows its laminar structure.

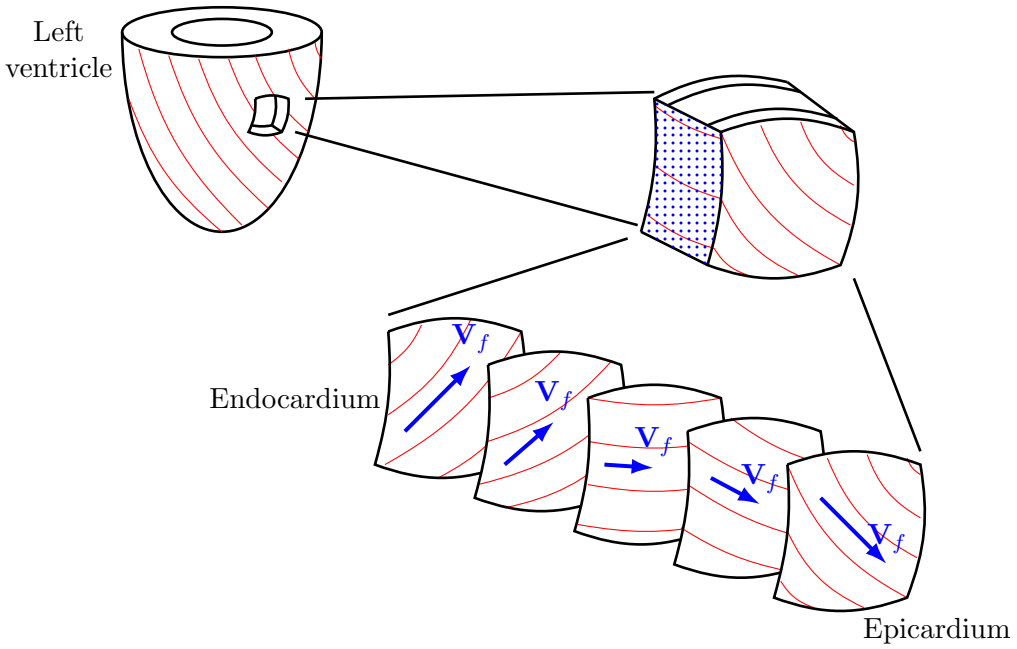

Figure 2.9: Schematic illustration of the tissue layout in the left ventricle as well as the transmural variation in the fibre direction $\mathbf{V}_f$, adapted from [95].

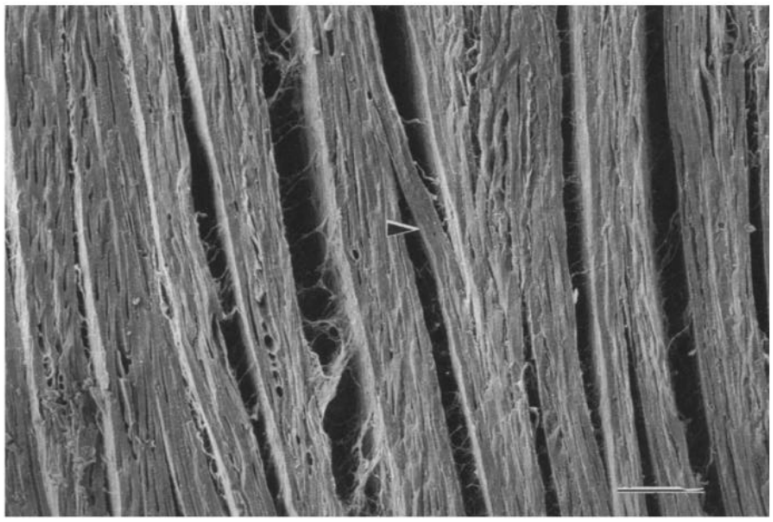

Figure 2.10: Electron micrograph showing the layered organisation of cardiac tissue in the heart wall, from [72].

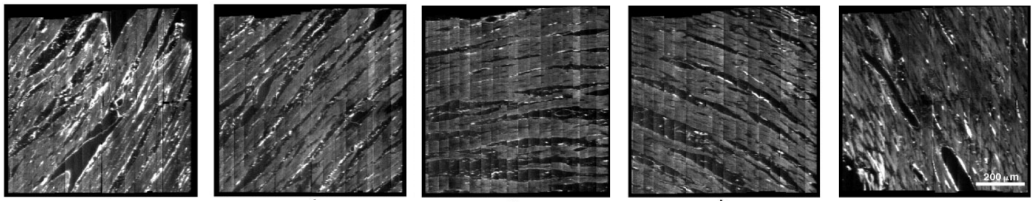

Endocardium Epicardium

Figure 2.11: Microscopic images of cardiac tissue reproduced from [140] showing the variation in the fibre direction across the ventricular wall.

The longitudinal axis of the muscle fibre is referred to as the fibre direction. Since the electrical impulse travels approximately 3 times faster along the longitudinal axis of the fibre than in the transverse direction, the propagation of the impulse is highly dependent on the fibre layout [15]. At the epicardial region, the fibres are arranged in a left-handed spiral, which gradually changes to a right-handed spiral pattern near the endocardium. Cross-sectional images of the ventricular wall in Figure 2.11 show the variation in the fibre orientation through the myocardial wall. At the epicardium, the fibre angle is between -50° and -70°. The angle changes through the wall to an angle of +50° to +70° at the endocardial region [55, 115, 140].

2.4.5 Extracellular Matrix

Two thirds of the myocardial volume consist of cardiac muscle tissue. The remaining one third is occupied by other cellular components, the extracellular matrix and tissue fluid [16, 101].

Figure 2.12 shows bundles of cardiac tissue surrounded by the extracellular matrix. The epimysium, perimysium and endomysium are the main components of the extracellular matrix and contribute to the overall mechanical behaviour of the myocardium [25]. The endomysium surrounds individual heart muscle fibres and laterally joins adjacent fibres. The perimysium is composed of weaves of collagen fibres and surrounds groups of cardiac fibres. Larger structures, also part of the

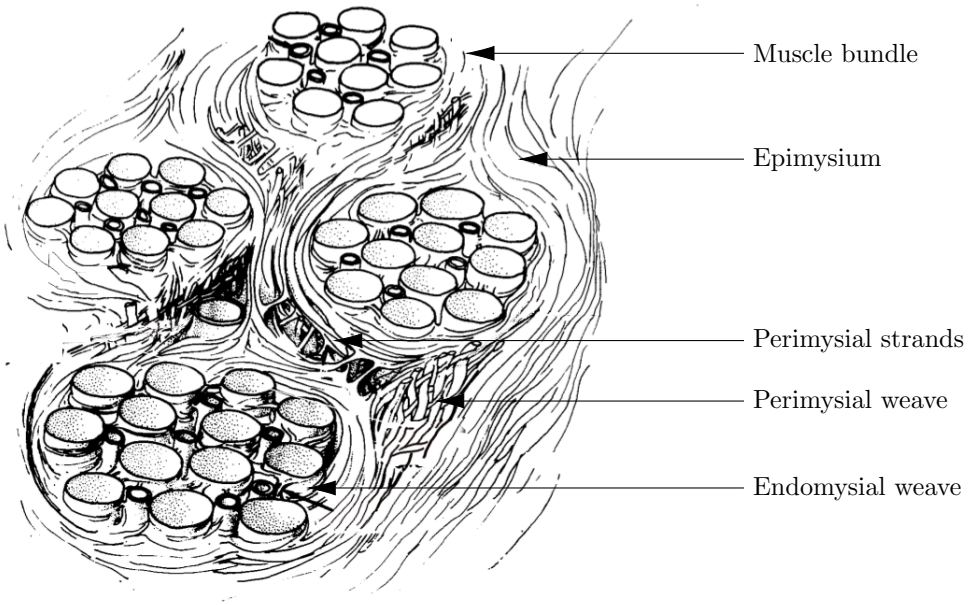

Figure 2.12: The endomysium, perimesium and epimysium form part of of the extracellular matrix that surrounds the cardiac muscle tissue, adapted from [25].

perimysium, join groups of muscle fibres. The endocardium and epicardium of the heart wall are surrounded by epimysial collagen fibres, which protect the cardiac fibres from being overstretched and thereby adding to the overall stiffness of the myocardium [25]. For a material model to be a good representation of myocardial material, it must feature both the muscle fibres and the extracellular matrix.

2.5 Summary of the Cardiac Physiology

The purpose of this chapter was to review the function of a healthy heart and to discuss briefly the micro-mechanics of fibre contraction. We noted that a heartbeat is divided into four phases with distinct pressure-volume relations. To perform a computational investigation of the heart it is necessary to determine an appropriate method to simulate these phases, as presented in later chapters.

For cardiac tissue one finds internal structures at different length scales. The macroscopic behaviour of the heart is determined by the dynamics of cardiac tissue on the micro-scale. For example, the sliding of filaments on the micro-scale is responsible for the contraction of muscle fibres and therefore also the contraction of the heart chambers.

We also discussed the layout of cardiac fibres in the heart and noted that the direction of the fibres varies across the ventricular wall. For example, at the outer surface of the left ventricle, the fibres form a left-handed helix whereas the cardiac fibres near the inner surface are arranged in a right-handed helix. Cardiac function is highly dependent on this arrangement. The layout of the cardiac fibres causes the ventricles to experience different types of motions such as twisting, wall thickening and untwisting.

Chapter 3

Non-Linear Continuum Mechanics

The theories of classical continuum mechanics are utilised extensively in the engineering environment to describe the behaviour of structures and materials. A classical continuum formulation neglects features on the anatomic and molecular scales and assumes that a body is composed of a continuous, rather than a discrete, distribution of continuum particles. A comprehensive overview of continuum mechanics can be found in [52].

In general, the continuum mechanics approach consists of (i) deriving general principles that are valid for all materials be it solids or fluids and (ii) developing constitutive models to describe the behaviour of individual materials. Both of these components are dealt with in subsequent sections. Because we ultimately want to simulate the behaviour of cardiac tissue, this chapter also introduces the concept of hyperelasticity, a popular type of constitutive model used to describe non-linear elastic material behaviour. Finally, the chapter reviews the finite element method and briefly describes curvilinear coordinate systems.

3.1 Tensor Preliminaries

A second-order tensor $\mathbf{T}$ is a mathematical entity that linearly maps a vector to another vector,

$$\mathbf{b} = \mathbf{T}\mathbf{a}\,. \tag{3.1}$$

In the above, the tensor $\mathbf{T}$ acts on vector $\mathbf{a}$ to produce vector $\mathbf{b}$. Vectors are also referred to as first-order tensors. We can extend Equation (3.1) to higher order tensors, for example

$$\mathbf{A} = \mathbb{C}\mathbf{B}\,, \tag{3.2}$$

where $\mathbb{C}$ is a fourth-order tensor and $\mathbf{A}$ and $\mathbf{B}$ are second-order tensors. In the Cartesian space, we express tensors in terms of their components as follows,

scalar (zeroth-order): ρ	second-order: $\mathbf{A} = A_{ij}\ \mathbf{e}_i \otimes \mathbf{e}_j$
first-order: $\mathbf{a} = a_i \mathbf{e}_i$	fourth-order: $\mathbb{A} = \mathbb{A}_{ijkl}\ \mathbf{e}_i \otimes \mathbf{e}_j \otimes \mathbf{e}_k \otimes \mathbf{e}_l$

where $\otimes$ is the dyadic or tensor product. Scalars are usually denoted with lower case Greek symbols, first-order tensors with lower case boldface Roman letters, second-order tensors with upper case boldface Roman letters and fourth-order tensors with blackboard bold letters.

The previous expressions utilise the Einstein summation convention where a repeated index denotes a summation over that index,

$$a_i b_i c_j = \sum_{i=1}^{n} a_i b_i c_j \,. \tag{3.3}$$

The repeated index i is referred to as the dummy index while indices that appear only once are called free indices.

3.1.1 Symmetry

Any tensor $\mathbf{T}$ can be additively decomposed into a symmetric component $\mathbf{S}$ and a skew-symmetric component $\mathbf{W}$. That is,

$$\mathbf{T} = \mathbf{S} + \mathbf{W} \,, \tag{3.4}$$

where $\mathbf{S}$ and $\mathbf{W}$ are defined as

$$\mathbf{S} = \mathbf{T}^{\text{symm}} = \frac{1}{2}(\mathbf{T} + \mathbf{T}^T) \,, \tag{3.5}$$

$$\mathbf{W} = \mathbf{T}^{\text{skew}} = \frac{1}{2}(\mathbf{T} - \mathbf{T}^T) \,. \tag{3.6}$$

$\mathbf{T}^T$ in the above denotes the transpose of the tensor $\mathbf{T}$. A symmetric tensor $\mathbf{S}$ and skew-symmetric tensor $\mathbf{W}$ satisfy the following,

$$\mathbf{S} = \mathbf{S}^T \qquad \text{and} \qquad \mathbf{W} = -\mathbf{W}^T \,. \tag{3.7}$$

3.1.2 Scalar Invariants

A second-order tensor $\mathbf{T}$ has the following property,

$$\mathbf{T}\mathbf{n} = \lambda \mathbf{n} \,, \tag{3.8}$$

where $\mathbf{n}$ is the eigenvector and λ the eigenvalue of $\mathbf{T}$. Equation (3.8) is known as the eigenvalue problem and to solve it we rewrite the expression as

$$(\mathbf{T} - \lambda \mathbf{I})\mathbf{n} = \mathbf{0} \,, \tag{3.9}$$

where $\mathbf{I}$ is the identity matrix. For non-trivial solutions of $\mathbf{n}$, the inverse of $(\mathbf{T} - \lambda \mathbf{I})$ does not exist and as a result

$$\det(\mathbf{T} - \lambda \mathbf{I}) = 0 \,. \tag{3.10}$$

Solving Equation (3.10) leads to the characteristic equation,

$$\lambda^3 - I_1 \lambda^2 + I_2 \lambda - I_3 = 0 \,, \tag{3.11}$$

where I_i are the scalar invariants of $\mathbf{T}$. The scalar invariants remain unchanged irrespective of the coordinate system in which the tensor is defined. This is an important property that is frequently exploited in continuum mechanics. For example, material laws are often defined in terms of the scalar invariants to ensure that it is independent of the chosen coordinate system.

The invariants of $\mathbf{T}$ are given as

$$\begin{aligned} I_1 &= \mathrm{tr}\mathbf{T}\,, \\ I_2 &= \frac{1}{2}\big((\mathrm{tr}\mathbf{T})^2 - \mathrm{tr}\mathbf{T}^2\big)\,, \\ I_3 &= \det\mathbf{T}\,. \end{aligned} \tag{3.12}$$

The tensor $\mathbf{T}$ can also be expressed in terms its eigenvalues,

$$\mathbf{T} = \sum_{i=1}^{3} \lambda_i\, \mathbf{n}_i \otimes \mathbf{n}_i \tag{3.13}$$

3.2 Kinematics

The deformation of a three-dimensional continuum body in the Euclidean reference frame is shown in Figure 3.1. At time t_0 the body is in its undeformed state and occupies the space $\mathcal{B}_0$. The underformed state is also called the initial or reference configuration. The body undergoes deformation and at some time t, it occupies the space $\mathcal{B}$. The deformed state is referred to as the current or spatial configuration. The motion $\boldsymbol{\varphi}$ from the reference position to the current position is given by

$$\mathbf{x} = \boldsymbol{\varphi}(\mathbf{X}, t)\,. \tag{3.14}$$

The displacement of the continuum particle P is defined as

$$\mathbf{u}(\mathbf{X}, t) = \mathbf{x}(\mathbf{X}, t) - \mathbf{X}\,, \tag{3.15}$$

where $\mathbf{X}$ is the initial position of the particle and $\mathbf{x}$ the current position at time t.

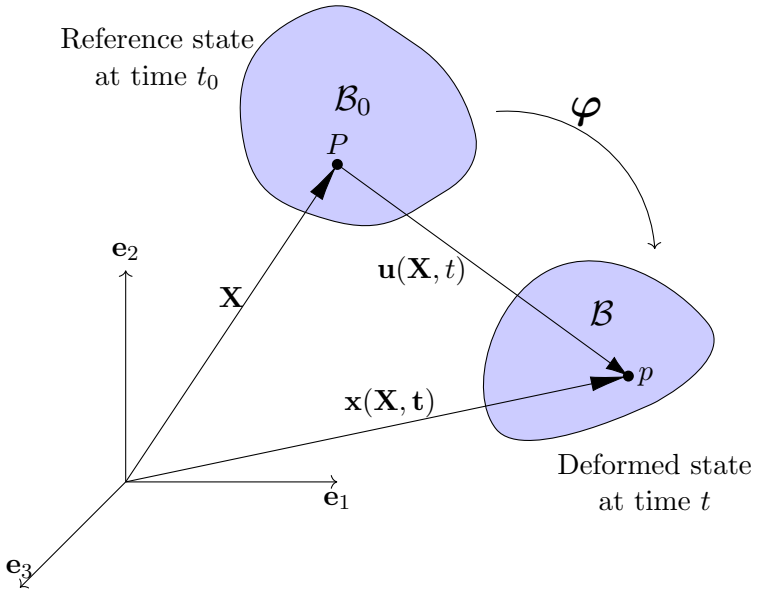

Figure 3.1: Motion of a continuum body in the Euclidean space.

The convention is to use upper case letters to denote the initial configuration and lower case letters to denote the current configuration. The gradient of a field $(\bullet)$ may be with respect to either the reference or the current configuration,

$$\text{Grad}(\bullet) = (\bullet) \otimes \nabla_{\mathbf{X}} = \frac{\partial(\bullet)}{\partial X_j} \otimes \mathbf{e}_j \,, \qquad \text{grad}(\bullet) = (\bullet) \otimes \nabla_{\mathbf{x}} = \frac{\partial(\bullet)}{\partial x_j} \otimes \mathbf{e}_j \,. \tag{3.16}$$

The divergence of a vector field $(\bullet)$ is defined as the scalar product of the gradient operator and the vector field,

$$\text{Div}(\bullet) = (\bullet) \cdot \nabla_{\mathbf{X}} = \frac{\partial(\bullet)}{\partial X_j} \cdot \mathbf{e}_j \,, \qquad \text{div}(\bullet) = (\bullet) \cdot \nabla_{\mathbf{x}} = \frac{\partial(\bullet)}{\partial x_j} \cdot \mathbf{e}_j \,. \tag{3.17}$$

The deformation gradient $\mathbf{F}$ is the derivative of the spatial position $\mathbf{x}$ with respect to the reference position,

$$\mathbf{F}(\mathbf{X}, t) = \frac{\partial \mathbf{x}}{\partial \mathbf{X}} = \frac{\partial(\mathbf{X} + \mathbf{u})}{\partial \mathbf{X}} = \mathbf{I} + \frac{\partial \mathbf{u}}{\partial \mathbf{X}} \,, \tag{3.18}$$

where $\mathbf{I}$ is the identity matrix. From the definition of differential $\mathrm{d}\mathbf{x}$,

$$\mathrm{d}\mathbf{x} = \frac{\partial \mathbf{x}}{\partial \mathbf{X}} \mathrm{d}\mathbf{X} = \mathbf{F}\mathrm{d}\mathbf{X}, \tag{3.19}$$

we see that the deformation gradient maps an infinitesimal line element in the reference configuration to a line element in the deformed configuration. The determinant of the deformation gradient provides a relationship between an infinitesimal volume element in the current state and the volume element in the reference state,

$$J = \det\mathbf{F} = \frac{\mathrm{d}v}{\mathrm{d}V} \,, \tag{3.20}$$

where J is known as the Jacobian and $\mathrm{d}v$ and $\mathrm{d}V$ are the infinitesimal volumes in the current and the reference configuration respectively. Values of J$\leq$0 result in either negative or zero volumes, i.e. unrealistic motion, and as a consequence only motions where J$>$0 are allowed. In the case of no volume change, we find that $\mathrm{d}v = \mathrm{d}V$ and consequently J = 1.

Nanson's formula provides a relationship between an infinitesimal area element defined in the reference configuration and an area element defined in the current configuration,

$$\boldsymbol{\nu}\mathrm{d}a = J\mathbf{F}^{-T}\mathbf{n}\mathrm{d}A \,, \tag{3.21}$$

where $\mathrm{d}A$ and its unit normal $\mathbf{n}$ are defined in the reference configuration and $\mathrm{d}a$ along with its unit normal $\boldsymbol{\nu}$ is defined in the current configuration. Another useful identity is

$$\frac{\mathrm{D}J}{\mathrm{D}t} = \dot{J} = J\text{div}\dot{\mathbf{x}} \,, \tag{3.22}$$

where $\dot{J}$ is the material time derivative of the Jacobian and $\dot{\mathbf{x}} = \frac{\mathrm{dx}}{\mathrm{dt}}$ is the velocity field.

3.2.1 Time Derivatives

The velocity field $\dot{\mathbf{x}}$ and acceleration field $\ddot{\mathbf{x}}$ in the material description, i.e. expressed in terms of the reference coordinates $\mathbf{X}$, are given by

$$\dot{\mathbf{x}}(\mathbf{X},t) = \frac{\partial \mathbf{x}(\mathbf{X},t)}{\partial t}\,, \qquad \ddot{\mathbf{x}}(\mathbf{X},t) = \frac{\partial \dot{\mathbf{x}}(\mathbf{X},t)}{\partial t}\,. \tag{3.23}$$

If a scalar field ϕ is expressed in terms of the spatial coordinates $\mathbf{x}$, the chain rule is used to obtain the material time derivative,

$$\dot{\phi}(\mathbf{x},t) = \frac{\mathrm{D}\phi}{\mathrm{D}t} = \frac{\partial \phi}{\partial t} + \frac{\partial \phi}{\partial \mathbf{x}}\frac{\partial \mathbf{x}}{\partial t}\,. \tag{3.24}$$

Similarly, for a vector field $\mathbf{v}$ defined in the current configuration, we have

$$\begin{aligned} \dot{\mathbf{v}}(\mathbf{x},t) = \frac{\mathrm{D}\mathbf{v}}{\mathrm{D}t} &= \frac{\partial \mathbf{v}}{\partial t} + \frac{\partial \mathbf{v}}{\partial \mathbf{x}}\frac{\partial \mathbf{x}}{\partial t} \\ &= \frac{\partial \mathbf{v}}{\partial t} + (\mathrm{grad}\mathbf{v})\dot{\mathbf{x}}\,. \end{aligned} \tag{3.25}$$

The symmetric part of the velocity gradient is known as the rate of deformation $\mathbf{d}$ and the skew-symmetric part is referred to as the spin $\boldsymbol{\omega}$,

$$\mathbf{d} = \mathbf{l}^{\mathrm{symm}} = \frac{1}{2}(\mathbf{l} + \mathbf{l}^T)\,, \tag{3.26}$$

$$\boldsymbol{\omega} = \mathbf{l}^{\mathrm{skew}} = \frac{1}{2}(\mathbf{l} - \mathbf{l}^T)\,, \tag{3.27}$$

where $\mathbf{l} = \mathrm{grad}\dot{\mathbf{x}}$ is the velocity gradient. The material time derivative of the deformation gradient can be expressed in terms of the velocity gradient as

$$\dot{\mathbf{F}} = \mathbf{l}\mathbf{F}\,. \tag{3.28}$$

3.3 Strain Measures

Strain is a measure of the deformation experienced by the continuum body. If $\mathrm{d}s$ and $\mathrm{d}S$ represent the magnitudes of the infinitesimal line elements $\mathrm{d}\mathbf{x}$ and $\mathrm{d}\mathbf{X}$ then we have

$$(\mathrm{d}s)^2 = \mathrm{d}\mathbf{x}\cdot\mathrm{d}\mathbf{x} \qquad \text{and} \qquad (\mathrm{d}S)^2 = \mathrm{d}\mathbf{X}\cdot\mathrm{d}\mathbf{X}\,, \tag{3.29}$$

where $\mathrm{d}\mathbf{x}$ and $\mathrm{d}\mathbf{X}$ are defined in the current and the reference configuration respectively. Consider the difference between the squares of the magnitudes,

$$\begin{aligned} (\mathrm{d}s)^2 - (\mathrm{d}S)^2 &= \mathrm{d}\mathbf{x}\cdot\mathrm{d}\mathbf{x} - \mathrm{d}\mathbf{X}\cdot\mathrm{d}\mathbf{X} \\ &= \mathbf{F}\mathrm{d}\mathbf{X}\cdot\mathbf{F}\mathrm{d}\mathbf{X} - \mathrm{d}\mathbf{X}\cdot\mathrm{d}\mathbf{X} \\ &= \mathrm{d}\mathbf{X}\cdot\mathbf{F}^T\mathbf{F}\mathrm{d}\mathbf{X} - \mathrm{d}\mathbf{X}\cdot\mathrm{d}\mathbf{X} \\ &= \mathbf{F}^T\mathbf{F} : \mathrm{d}\mathbf{X}\otimes\mathrm{d}\mathbf{X} - \mathbf{I} : \mathrm{d}\mathbf{X}\otimes\mathrm{d}\mathbf{X} \\ &= (\mathbf{F}^T\mathbf{F} - \mathbf{I}) : d\mathbf{X}\otimes d\mathbf{X}\,. \end{aligned} \tag{3.30}$$

Two deformation tensors frequently found in continuum mechanics texts are the right Cauchy-Green deformation tensor $\mathbf{C}$ and the Green-Lagrange strain tensor $\mathbf{E}$. These tensors are defined as

$$\mathbf{C} = \mathbf{F}^T\mathbf{F}\,, \tag{3.31}$$

$$\mathbf{E} = \frac{1}{2}(\mathbf{F}^T\mathbf{F} - \mathbf{I}) = \frac{1}{2}(\mathbf{C} - \mathbf{I})\,. \tag{3.32}$$

We can write Equation (3.30) in term of the deformation tensors as

$$\begin{aligned}(\mathrm{d}s)^2 - (\mathrm{d}S)^2 &= (\mathbf{C} - \mathbf{I}) : d\mathbf{X} \otimes d\mathbf{X} \\ &= 2\mathbf{E} : d\mathbf{X} \otimes d\mathbf{X}\,. \end{aligned} \tag{3.33}$$

3.4 Stress Measures

Forces acting on the body cause deformation. Within the framework of continuum mechanics, we identify two main types of forces. A *body force* $\mathbf{b}$ acts throughout the entire volume of the body while a *traction* or *surface force* $\mathbf{t}$ acts on some surface (external or internal) of the body.

Consider the surface shown in Figure 3.2 that passes through a point q in the body $\mathcal{B}$. At q the surface has a unit normal $\boldsymbol{\nu}$. If $\Delta\mathbf{f}$ is the resultant force acting on an infinitesimal area element Δa on the surface, then Cauchy's stress principle states that the traction $\mathbf{t}^{(\boldsymbol{\nu})}$ is given by

$$\mathbf{t}^{(\boldsymbol{\nu})}(\mathbf{x}, t) = \lim_{\Delta a \to 0} \frac{\Delta\mathbf{f}}{\Delta a} = \frac{\mathrm{d}\mathbf{f}}{\mathrm{d}a}\,. \tag{3.34}$$

The traction at the current position of point q is a function of the unit normal $\boldsymbol{\nu}$. This dependence can be expressed with a linear transformation,

$$\mathbf{t}^{(\boldsymbol{\nu})}(\mathbf{x}, t) = \boldsymbol{\sigma}(\mathbf{x}, t)\boldsymbol{\nu}(\mathbf{x}, t)\,. \tag{3.35}$$

The linear transformation $\boldsymbol{\sigma}$ is known as the Cauchy stress tensor.

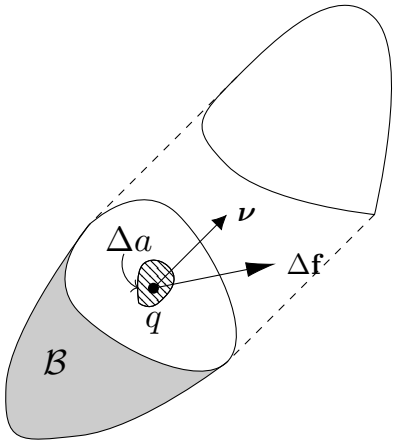

Figure 3.2: Force acting on a plane that passes through an arbitrary point in the body.

The stress may also be expressed in the reference configuration,

$$\mathbf{t}^{(\mathbf{n})}(\mathbf{X},t) = \mathbf{P}(\mathbf{X},t)\mathbf{n}(\mathbf{X})\,, \tag{3.36}$$

where $\mathbf{X}$ is the position in the reference state and $\mathbf{n}$ the unit normal of the area element $\mathrm{d}A$ in the reference configuration. The linear transformation $\mathbf{P}$ in Equation (3.36) is called the first Piola-Kirchhoff stress tensor. To relate the first Piola-Kirchhoff stress to the Cauchy stress, we define $\mathbf{P}$ such that the force $\mathrm{d}\mathbf{f}$ acting on $\mathrm{d}a$ is the same as the force acting on $\mathrm{d}A$. That is,

$$\mathrm{d}\mathbf{f} = \mathbf{P}\mathbf{n}\mathrm{d}A = \boldsymbol{\sigma}\boldsymbol{\nu}\mathrm{d}a = \boldsymbol{\sigma}J\mathbf{F}^{-T}\mathbf{n}\mathrm{d}A\,, \tag{3.37}$$

where we have utilised Nanson's formula. Therefore, the first Piola-Kirchhoff stress tensor expressed in terms of the Cauchy stress tensor is

$$\mathbf{P} = J\boldsymbol{\sigma}\mathbf{F}^{-T}\,. \tag{3.38}$$

The Cauchy stress tensor is symmetric and is defined in the current configuration, whereas the first Piola-Kirchhoff stress tensor is generally not symmetric and is defined in both the reference and current configurations. The symmetry of the Cauchy stress tensor is a result of the conservation of angular momentum, see [67]. Another useful stress tensor, the second Piola-Kirchhoff stress $\mathbf{S}$, is given by

$$\mathbf{S} = \mathbf{F}^{-1}\mathbf{P} = J\mathbf{F}^{-1}\boldsymbol{\sigma}\mathbf{F}^{-T}\,. \tag{3.39}$$

$\mathbf{S}$ is a symmetric tensor that is defined in the reference configuration.

3.5 Conservation Laws

Balance laws are the fundamental laws that govern the behaviour of all continua. In this section the continuity equation and Cauchy's first equation of motion are derived from the principle of mass conservation and the principle of linear momentum conservation.

3.5.1 Conservation of Mass

The principle of mass conservation states that the mass of any body or arbitrary subdomain stays constant. Therefore, the rate of mass change of the subdomain is zero,

$$\underbrace{\frac{\mathrm{D}}{\mathrm{Dt}}\int_{\mathcal{B}}\rho\,\mathrm{d}v}_{rate\,of\,mass\,change} = 0\,, \tag{3.40}$$

where $\frac{\mathrm{D}}{\mathrm{Dt}}$ denotes the total derivative and ρ the density of the continuum at time t. Using Equation (3.20), the preceding equation may be written with respect to the reference configuration $\mathcal{B}_0$. This allows one to take the derivative of the integrand since the reference configuration is independent of time,

$$\frac{\mathrm{D}}{\mathrm{Dt}}\int_{\mathcal{B}}\rho\,\mathrm{d}v = \frac{\mathrm{D}}{\mathrm{Dt}}\int_{\mathcal{B}_0}\rho J\,\mathrm{d}V = \int_{\mathcal{B}_0}\frac{\mathrm{D}}{\mathrm{Dt}}(\rho J)\,\mathrm{d}V = 0\,. \tag{3.41}$$

We expand the previous expression using the product rule,

$$\begin{aligned}\int_{\mathcal{B}_0} \frac{\mathrm{D}}{\mathrm{Dt}}(\rho J)\mathrm{d}V &= \int_{\mathcal{B}_0} \left(\frac{\mathrm{D}\rho}{\mathrm{Dt}}J + \rho\frac{\mathrm{D}J}{\mathrm{Dt}}\right)\mathrm{d}V \\ &= \int_{\mathcal{B}_0} (\dot{\rho}J + \rho J \mathrm{div}\dot{\mathbf{x}})\,\mathrm{d}V \\ &= \int_{\mathcal{B}} (\dot{\rho} + \rho\mathrm{div}\dot{\mathbf{x}})\,\mathrm{d}v\,, \end{aligned} \tag{3.42}$$

where we have utilised Equation (3.22). Since the principle of mass conservation is valid for any domain, the integrand is zero,

$$\dot{\rho} + \rho\mathrm{div}\dot{\mathbf{x}} = 0\,. \tag{3.43}$$

This expression is known as the continuity equation.

3.5.2 Conservation of Linear Momentum

The principle of linear momentum conservation states that the rate of change of linear momentum of any subdomain $\mathcal{B}$ is equal to the forces that act on the subdomain. That is,

$$\underbrace{\frac{\mathrm{D}}{\mathrm{D}t}\int_{\mathcal{B}} (\rho\dot{\mathbf{x}})\,\mathrm{d}v}_{rate\ of\ change\ of\ linear\ momentum} = \underbrace{\int_{\partial\mathcal{B}} \mathbf{t}^{(\boldsymbol{\nu})}\,\mathrm{d}a}_{surface\ force} + \underbrace{\int_{\mathcal{B}} \rho\mathbf{b}\,\mathrm{d}v}_{body\ force}\,, \tag{3.44}$$

where $\partial\mathcal{B}$ is the surface that bounds the domain $\mathcal{B}$. The body force $\mathbf{b}$ is defined per unit mass. As in the previous section, the left-hand side of Equation (3.44) may be expressed with respect to the reference configuration,

$$\frac{\mathrm{D}}{\mathrm{D}t}\int_{\mathcal{B}} (\rho\dot{\mathbf{x}})\,\mathrm{d}v = \frac{\mathrm{D}}{\mathrm{D}t}\int_{\mathcal{B}_0} (\rho\dot{\mathbf{x}}J)\,\mathrm{d}V = \int_{\mathcal{B}_0} \frac{\mathrm{D}}{\mathrm{D}t}(\rho\dot{\mathbf{x}}J)\,\mathrm{d}V\,. \tag{3.45}$$

Applying the product rule and making use of Equation (3.43) yield,

$$\begin{aligned}\int_{\mathcal{B}_0} \frac{\mathrm{D}}{\mathrm{D}t}(\rho\dot{\mathbf{x}}J)\,\mathrm{d}V &= \int_{\mathcal{B}_0} \left(\frac{\mathrm{D}\dot{\mathbf{x}}}{\mathrm{D}t}\rho J + \underbrace{\dot{\mathbf{x}}J\frac{\mathrm{D}\rho}{\mathrm{D}t} + \dot{\mathbf{x}}\rho\frac{\mathrm{D}J}{\mathrm{D}t}}_{\dot{\mathbf{x}}J(\dot{\rho}+\rho\mathrm{div}\dot{\mathbf{x}})=0}\right)\mathrm{d}V \\ &= \int_{\mathcal{B}_0} \frac{\mathrm{D}\dot{\mathbf{x}}}{\mathrm{D}t}\rho J\,\mathrm{d}V \\ &= \int_{\mathcal{B}} \ddot{\mathbf{x}}\rho\,\mathrm{d}v\,, \end{aligned} \tag{3.46}$$

Using Equation (3.35) and the divergence theorem, the right-hand side of Equation (3.44) can be restated as,

$$\int_{\partial\mathcal{B}} \mathbf{t}^{(\boldsymbol{\nu})}\,\mathrm{d}a + \int_{\mathcal{B}} \rho\mathbf{b}\,\mathrm{d}v = \int_{\partial\mathcal{B}} \boldsymbol{\sigma}\boldsymbol{\nu}\,\mathrm{d}a + \int_{\mathcal{B}} \rho\mathbf{b}\,\mathrm{d}v = \int_{\mathcal{B}} \mathrm{div}\boldsymbol{\sigma}\,\mathrm{d}v + \int_{\mathcal{B}} \rho\mathbf{b}\,\mathrm{d}v\,. \tag{3.47}$$

Substituting Equations (3.46) and (3.47) back into Equation (3.44) leads to

$$\int_{\mathcal{B}} (\rho\ddot{\mathbf{x}} - \mathrm{div}\boldsymbol{\sigma} - \rho\mathbf{b})\mathrm{d}v = \mathbf{0}\,. \tag{3.48}$$

The preceding equation has to be valid for all $\mathcal{B}$, hence the integrand is zero. This gives Cauchy's first equation of motion,

$$\rho\ddot{\mathbf{x}} - \mathrm{div}\boldsymbol{\sigma} - \rho\mathbf{b} = \mathbf{0}\,. \tag{3.49}$$

If the body is in static equilibrium, Equation (3.49) becomes

$$\mathrm{div}\boldsymbol{\sigma} + \rho\mathbf{b} = \mathbf{0}\,, \tag{3.50}$$

which is referred to as the equation of equilibrium.

A boundary condition on a solid is categorised as either a Dirichlet or a Neumann boundary condition. The Dirichlet (or essential) boundary conditions are

$$\mathbf{u} = \bar{\mathbf{u}} \qquad \text{on} \qquad \partial\mathcal{B}_D \tag{3.51}$$

where $\bar{\mathbf{u}}$ is the prescribed displacement on the Dirichlet boundary $\partial\mathcal{B}_D$. The Neumann (or natural) boundary condition is given by

$$\mathbf{P}\mathbf{n} = \bar{\mathbf{t}}^{(\mathbf{n})} \qquad \text{on} \qquad \partial\mathcal{B}_N \tag{3.52}$$

where $\bar{\mathbf{t}}^{(\mathbf{n})}$ is the prescribed traction on the Neumann boundary $\partial\mathcal{B}_N$. Together with the boundary conditions, the governing equation forms the so-called *strong form* of the problem definition.

3.6 Hyperelasticity

The kinematic relations, stresses and balance laws stated in the previous sections are valid for any continuum body, regardless of whether it is a solid or fluid. To distinguish one material from another and to characterise its behaviour, material models or constitutive laws are required. A constitutive law should match the real behaviour of the material.

Biological tissue, including passive cardiac tissue, is usually modelled as a hyperelastic material [19]. Hyperelasticity refers to the ability of a material to respond elastically when subjected to large deformations, i.e. the material has the ability to recover its original configuration once the applied load is removed.

3.6.1 Strain Energy Functions

In the context of hyperelasticity, one assumes the existence of a strain energy function ψ defined per unit volume. The strain energy function is a scalar-valued function that relates the amount of elastic energy stored to the deformation experienced by a continuum. The strain energy is often expressed as a function of the right Cauchy-Green deformation tensor or the Green-Lagrange strain tensor,

$$\psi = \psi(\mathbf{E}) = \psi(\mathbf{C})\,. \tag{3.53}$$

Expressions for the stress tensors may be derived from the strain energy function with the use of

the Clausius-Planck inequality [52]. For perfectly elastic materials without any thermal effects, the Clausius-Planck inequality reduces to

$$W_{int} - \dot{\psi} = 0\,, \tag{3.54}$$

where $\dot{\psi}$ is the rate of internal energy and W_{int} is the rate of mechanical energy. The rate of internal energy is expressed with work conjugate pairs, for example

$$W_{int} = \mathbf{S} : \dot{\mathbf{E}}\,, \qquad W_{int} = \mathbf{P} : \dot{\mathbf{F}}\,, \qquad W_{int} = \boldsymbol{\sigma} : \dot{\mathbf{d}}\,. \tag{3.55}$$

Considering the first conjugate pair, Equation (3.54) can be restated as

$$\begin{aligned} 0 &= \mathbf{S} : \dot{\mathbf{E}} - \dot{\psi} \\ 0 &= \mathbf{S} : \dot{\mathbf{E}} - \frac{\partial \psi}{\partial \mathbf{E}} : \frac{\partial \mathbf{E}}{\partial t} \\ 0 &= (\mathbf{S} - \frac{\partial \psi}{\partial \mathbf{E}}) : \dot{\mathbf{E}}\,. \end{aligned} \tag{3.56}$$

If there are no constraints on the motion, then the above expression is valid for all $\mathbf{E}$, hence

$$\mathbf{S} - \frac{\partial \psi}{\partial \mathbf{E}} = 0 \qquad \Rightarrow \qquad \mathbf{S} = \frac{\partial \psi}{\partial \mathbf{E}}\,. \tag{3.57}$$

Using Equation (3.32) we find that,

$$\mathbf{S} = 2\frac{\partial \psi}{\partial \mathbf{C}}\,. \tag{3.58}$$

In the subsequent sections we restrict ourselves to three types of hyperelastic material models, namely isotropic, transversely isotropic and orthotropic models.

3.6.2 Isotropy

Isotropic materials behave the same in all directions. To ensure the strain energy is invariant under rotation, it is often expressed in terms of the strain invariants of $\mathbf{C}$. That is

$$\psi = \psi(I_1^C, I_2^C, I_3^C)\,, \tag{3.59}$$

where I_i^C are the strain invariants of $\mathbf{C}$ as defined in Equation (3.12). Using the chain rule we find the second Piola-Kirchhoff stress to be

$$\mathbf{S} = 2\left(\frac{\partial \psi}{\partial I_1^C}\frac{\partial I_1^C}{\partial \mathbf{C}} + \frac{\partial \psi}{\partial I_2^C}\frac{\partial I_2^C}{\partial \mathbf{C}} + \frac{\partial \psi}{\partial I_3^C}\frac{\partial I_3^C}{\partial \mathbf{C}} \right). \tag{3.60}$$

3.6.3 Transverse Isotropy

If a material has a distinct response in one direction it is called transversely isotropic. As shown in Figure 3.3(a), the preferred direction is normal to the plane of isotropy. Apart from the three invariants I_1^C, I_2^C and I_3^C, it is necessary to compose additional invariants to take into account

the preferred material direction $\mathbf{V}_f$. In this way, the preferred direction is included in the strain energy function, i.e. $\psi(\mathbf{C}, \mathbf{V}_f)$. This is accomplished with a fourth and fifth invariant,

$$I_4^C = \mathbf{V}_f \cdot \mathbf{C}\mathbf{V}_f = \mathbf{C} : \mathbf{V}_f \otimes \mathbf{V}_f \,, \tag{3.61}$$
$$I_5^C = \mathbf{V}_f \cdot \mathbf{C}^2\mathbf{V}_f = \mathbf{C}^2 : \mathbf{V}_f \otimes \mathbf{V}_f \,. \tag{3.62}$$

The strain energy function for a transversely isotropic material is often given in the following form,

$$\psi = \psi_{iso}(I_1^C, I_2^C, I_3^C) + \psi_f(I_4^C, I_5^C) \,, \tag{3.63}$$

where ψ_{iso} is the isotropic component and ψ_f the transversely isotropic contribution to the strain energy. In terms of the strain invariants the second Piola-Kirchhoff stress tensor is given as

$$\mathbf{S} = 2\sum_{i=1}^{5} \frac{\partial \psi}{\partial I_i^C} \frac{\partial I_i^C}{\partial \mathbf{C}} \tag{3.64}$$

3.6.4 Orthotropy

An orthotropic material responds differently in three mutually orthogonal directions $\mathbf{V}_f$, $\mathbf{V}_s$ and $\mathbf{V}_n$, see Figure 3.3(b). As with a transversely isotropic material, these orthogonal directions need to be included in the strain energy function. Apart from the previously defined invariants we define additional invariants to account for orthotropy,

$$I_6^C = \mathbf{V}_s \cdot \mathbf{C}\mathbf{V}_s = \mathbf{C} : \mathbf{V}_s \otimes \mathbf{V}_s \,, \tag{3.65}$$
$$I_7^C = \mathbf{V}_s \cdot \mathbf{C}^2\mathbf{V}_s = \mathbf{C}^2 : \mathbf{V}_s \otimes \mathbf{V}_s \,. \tag{3.66}$$
$$I_8^C = \mathbf{V}_n \cdot \mathbf{C}\mathbf{V}_n = \mathbf{C} : \mathbf{V}_n \otimes \mathbf{V}_n \,, \tag{3.67}$$
$$I_9^C = \mathbf{V}_n \cdot \mathbf{C}^2\mathbf{V}_n = \mathbf{C}^2 : \mathbf{V}_n \otimes \mathbf{V}_n \,. \tag{3.68}$$

Because

$$I_4^C + I_6^C + I_8^C = \mathbf{C} : (\mathbf{V}_f \otimes \mathbf{V}_f + \mathbf{V}_s \otimes \mathbf{V}_s + \mathbf{V}_n \otimes \mathbf{V}_n) = \mathbf{C} : \mathbf{I} = I_1^C, \tag{3.69}$$

only three of the invariants I_1^C, I_4^C, I_6^C and I_8^C are independent.

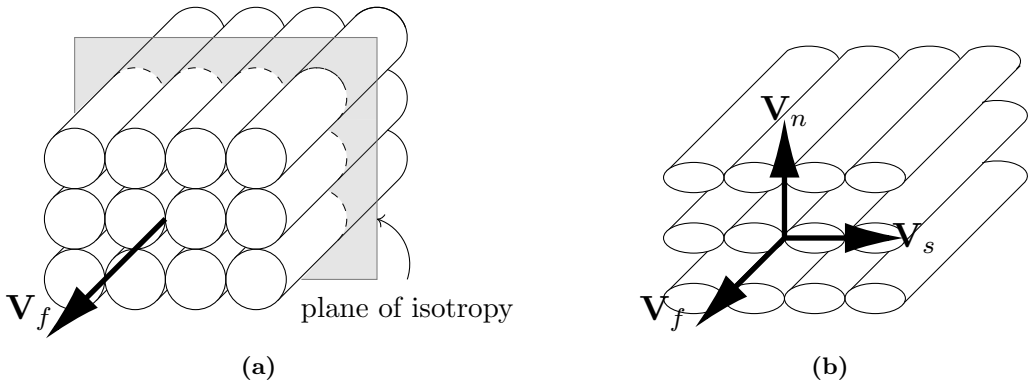

Figure 3.3: Illustration of (a) a transversely isotropic material with one preferred material direction and (b) an orthotropic material with three orthogonal material directions.

3.7 The Finite Element Method for Non-Linear Elasticity

When dealing with complex geometries, loading conditions or material behaviour, it is not always possible to analytically solve the governing equations [75]. The finite element method is a numerical method used to find approximate solutions to partial differential equations. This section discusses the general finite element framework for non-linear elastic continua in static equilibrium.

The finite element method for non-linear problems generally consists of (i) casting the governing equation into a weak (variational) form, (ii) discretising the weak formulation by approximating field variables with shape functions, (iii) linearising the weak form using a Taylor expansion and (iv) solving the system with an iterative scheme such as a Newton-Raphson algorithm.

3.7.1 Principle of Virtual Work

The finite element formulation is based on the weak form of the governing equation. In solid mechanics, the weak form is also referred to as the principle of virtual work. To obtain the weak form, we first consider a body subjected to an arbitrary displacement $\delta\mathbf{u}$. Equation (3.50) is multiplied by $\delta\mathbf{u}$ and integrated over the continuum domain $\mathcal{B}$,

$$\int_{\mathcal{B}} (\mathrm{div}\boldsymbol{\sigma} + \rho\mathbf{b}) \cdot \delta\mathbf{u} \, \mathrm{d}v = 0 \,, \tag{3.70}$$

where $\delta\mathbf{u}$ is also referred to as the virtual displacement. To ensure the boundary conditions are satisfied, $\delta\mathbf{u}$ vanishes on the Dirichlet boundary $\partial\mathcal{B}_D$. Using the product rule,

$$\mathrm{div}(\boldsymbol{\sigma}\delta\mathbf{u}) = \mathrm{div}\boldsymbol{\sigma} \cdot \delta\mathbf{u} + \boldsymbol{\sigma} : \mathrm{grad}\delta\mathbf{u} \,, \tag{3.71}$$

we can expand the integrand in Equation (3.70),

$$\int_{\mathcal{B}} \big(\mathrm{div}(\boldsymbol{\sigma}\delta\mathbf{u}) - \boldsymbol{\sigma} : \mathrm{grad}\delta\mathbf{u} + \rho\mathbf{b} \cdot \delta\mathbf{u}\big) \, \mathrm{d}v = 0 \,. \tag{3.72}$$

Applying the divergence theorem we obtain the weak form of the governing equation as

$$\int_{\partial\mathcal{B}} \boldsymbol{\sigma}\delta\mathbf{u} \cdot \boldsymbol{\nu} \, \mathrm{d}a - \int_{\mathcal{B}} \boldsymbol{\sigma} : \mathrm{grad}\delta\mathbf{u} \, \mathrm{d}v + \int_{\mathcal{B}} \rho\mathbf{b} \cdot \delta\mathbf{u} \, \mathrm{d}v = 0 \,. \tag{3.73}$$

The above can also be expressed in the reference configuration using Equations (3.20), (3.36) and (3.39),

$$\int_{\mathcal{B}_0} \mathbf{S} : \mathbf{F}^T \mathrm{Grad}\delta\mathbf{u} \, \mathrm{d}V - \int_{\partial\mathcal{B}_0} \bar{\mathbf{t}}^{(\mathbf{n})} \cdot \delta\mathbf{u} \, \mathrm{d}A - \int_{\mathcal{B}} \rho_0\mathbf{b} \cdot \delta\mathbf{u} \, \mathrm{d}V = 0 \,. \tag{3.74}$$

Noting that

$$\delta\mathbf{F} = \delta\left(\frac{\partial\mathbf{x}}{\partial\mathbf{X}}\right) = \delta\left(\frac{\partial(\mathbf{X}+\mathbf{u})}{\partial\mathbf{X}}\right) = \delta\left(\mathbf{I} + \frac{\partial\mathbf{u}}{\partial\mathbf{X}}\right) = \frac{\partial\delta\mathbf{u}}{\partial\mathbf{X}} \,, \tag{3.75}$$

we write Equation (3.74) as

$$\int_{\mathcal{B}_0} \mathbf{S} : \mathbf{F}^T\delta\mathbf{F} \, \mathrm{d}V - \int_{\partial\mathcal{B}_0} \bar{\mathbf{t}}^{(\mathbf{n})} \cdot \delta\mathbf{u} \, \mathrm{d}A - \int_{\mathcal{B}} \rho_0\mathbf{b} \cdot \delta\mathbf{u} \, \mathrm{d}V = 0 \,. \tag{3.76}$$

To rewrite the weak form in terms of the Green-Lagrange strain tensor, the first term in Equation (3.76) is expanded using symmetric and skew-symmetric parts,

$$\int_{\mathcal{B}_0} \mathbf{S} : \mathbf{F}^T \delta\mathbf{F} \mathrm{d}V = \int_{\mathcal{B}_0} \mathbf{S} : \big((\mathbf{F}^T \delta\mathbf{F})^{\mathrm{symm}} + (\mathbf{F}^T \delta\mathbf{F})^{\mathrm{skew}} \big) \mathrm{d}V \,. \tag{3.77}$$

Since the scalar product of a symmetric tensor and skew-symmetric tensor is zero we have

$$\begin{aligned} \int_{\mathcal{B}_0} \mathbf{S} : \mathbf{F}^T \delta\mathbf{F} \mathrm{d}V &= \int_{\mathcal{B}_0} \mathbf{S} : \big((\mathbf{F}^T \delta\mathbf{F})^{\mathrm{symm}} \big) \mathrm{d}V \\ &= \int_{\mathcal{B}_0} \mathbf{S} : \frac{1}{2} \big(\delta\mathbf{F}^T \mathbf{F} + \mathbf{F}^T \delta\mathbf{F} \big) \mathrm{d}V \\ &= \int_{\mathcal{B}_0} \mathbf{S} : \delta\mathbf{E} \mathrm{d}V \,, \end{aligned} \tag{3.78}$$

where we have used the definition of the strain tensor in Equation (3.32). Therefore, the weak form of the equilibrium equation in terms of the Green-Lagrange strain tensor reads

$$\int_{\mathcal{B}_0} \mathbf{S} : \delta\mathbf{E} \, \mathrm{d}V - \int_{\partial\mathcal{B}_0} \bar{\mathbf{t}}^{(\mathbf{n})} \cdot \delta\mathbf{u} \, \mathrm{d}A - \int_{\mathcal{B}_0} \rho_0 \mathbf{b} \cdot \delta\mathbf{u} \, \mathrm{d}V = 0 \,. \tag{3.79}$$

3.7.2 Discretisation

The geometry of the body $\mathcal{B}$ is discretised into a finite number of elements, as illustrated in the Figure 3.4. We divide the domain $\mathcal{B}$ into n_e elements, such that

$$\mathcal{B} \approx \mathcal{B}^h = \bigcup_{e=1}^{n_e} \Omega_e, \tag{3.80}$$

where $\mathcal{B}^h$ is the approximated body and Ω_e is the e^{th} element. The chosen element type depends on the problem at hand. Figure 3.5 shows examples of different element types.

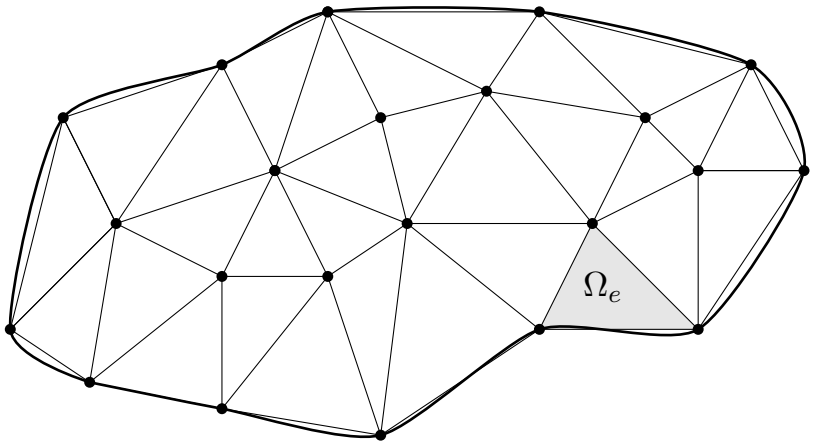

Figure 3.4: Discretisation of a continuum body into a finite number of elements.

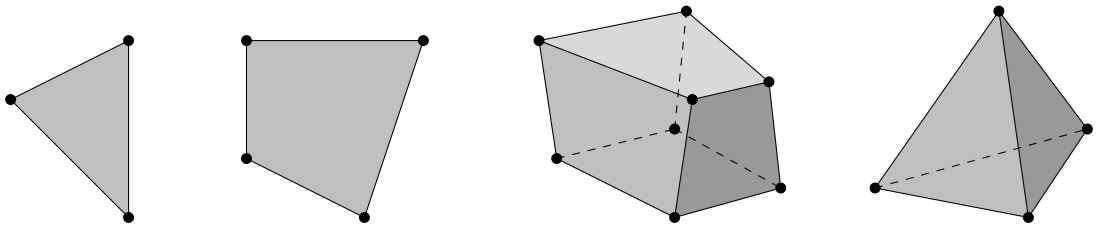

(a) **(b)**

Figure 3.5: Examples of finite elements used to discretise the problem domain include (a) elements for two dimensional problems, such as triangular and quadrilateral elements and (b) elements for three-dimensional problems, such as hexahedral and tetrahedral elements.

We not only approximate the geometry but also the primary field variables, in this case the displacement. The exact displacement solution is approximated using interpolation functions,

$$\mathbf{u}_{exact} \approx \sum_{I=1}^{n} N^I(\mathbf{X})\mathbf{u}^I \,, \tag{3.81}$$

where $\mathbf{u}^I$ is the unknown displacements at the nodes of an element with n nodes and N^I are the shape functions. Similarly, we approximate the gradient of the displacement with

$$\text{Grad}\mathbf{u}_{exact} = \mathbf{u}_{exact} \otimes \nabla_{\mathbf{X}} \approx \sum_{I=1}^{n} \mathbf{u}^I \otimes \frac{\partial N^I(\mathbf{X})}{\partial \mathbf{X}} \,. \tag{3.82}$$

With the Galerkin formulation, the virtual displacement is approximated using the same shape functions, that is

$$\delta\mathbf{u}_{exact} \approx \sum_{I=1}^{n} N^I(\mathbf{X})\delta\mathbf{u}^I \,, \qquad \text{Grad}\delta\mathbf{u}_{exact} \approx \sum_{I=1}^{n} \delta\mathbf{u}^I \otimes \frac{\partial N^I(\mathbf{X})}{\partial \mathbf{X}} \,. \tag{3.83}$$

3.7.3 Linearisation of the Weak Formulation

Finite deformations (large strains) and non-linear material behaviour introduce non-linearities into the system. We therefore linearise the weak form and use an iterative method, such as the Newton-Raphson scheme, to find an approximate solution to the displacement field. Discretisation and linearisation are often more convenient to perform in index notation. With index notation we avoid complex tensor rules since the components of the tensors are scalars.

First, let us define the residual G using the weak form in Equation (3.74),

$$\mathrm{G} = \int_{\mathcal{B}_0} S_{ij}F_{ri}\frac{\partial \delta u_r}{\partial X_j}\,\mathrm{d}V - \int_{\partial\mathcal{B}_0} \bar{t}_r^{(\mathbf{n})}\delta u_r\,\mathrm{d}A - \int_{\mathcal{B}} \rho_0 b_r \delta u_r\,\mathrm{d}V = 0 \,. \tag{3.84}$$

The objective is to find the displacement field that minimises the residual. To find a solution that minimises the above, we consider a first-order Taylor expansion of the residual,

$$\mathrm{G}_{k+1} = \mathrm{G}_k + \frac{\partial \mathrm{G}_k}{\partial \mathbf{u}} \cdot \Delta\mathbf{u}_k = \mathrm{G}_k + \Delta\mathrm{G}_k \,, \tag{3.85}$$

where $\Delta\mathbf{u}$ is the displacement increment, k is the current iteration step and $\Delta\mathrm{G}$ is the variation in the residual. The updated or new displacement is the sum of the current displacement and the displacement increment, that is

$$\mathbf{u}_{k+1} = \mathbf{u}_k + \Delta\mathbf{u}_k \,. \tag{3.86}$$

If we assume that the traction and body forces are conservative, i.e. do not depend on the displacement, then the variation in the residual is given as

$$\Delta\mathrm{G} \;=\; \int_{\mathcal{B}_0} (\Delta S_{ij}) F_{ri} \frac{\partial \delta u_r}{\partial X_j} \,\mathrm{d}V + \int_{\mathcal{B}_0} S_{ij} (\Delta F_{ri}) \frac{\partial \delta u_r}{\partial X_j} \,\mathrm{d}V \,, \tag{3.87}$$

where $\Delta\mathbf{F}$ and $\Delta\mathbf{S}$ are the variations in the deformation gradient and second Piola-Kirchhoff stress. Furthermore,

$$\Delta\mathrm{G} \;=\; \int_{\mathcal{B}_0} (\mathbb{C}_{ijkl} \Delta E_{kl}) F_{ri} \frac{\partial \delta u_r}{\partial X_j} \,\mathrm{d}V + \int_{\mathcal{B}_0} S_{ij} \left(\frac{\partial \Delta u_r}{\partial X_i} \right) \frac{\partial \delta u_r}{\partial X_j} \,\mathrm{d}V \,, \tag{3.88}$$

where $\Delta\mathbf{F} = \mathrm{Grad}\Delta\mathbf{u}$, see Equation (3.75). The fourth-order elasticity tensor $\mathbb{C} = \frac{\partial \mathbf{S}}{\partial \mathbf{E}}$ is a measure of the change in stress that occurs as a result of a change in strain. It has both major and minor symmetries. Using the definition of the strain tensor $\mathbf{E}$ and exploiting the symmetry of $\mathbb{C}$, we find that

$$\Delta\mathrm{G} = \int_{\mathcal{B}_0} \left(\mathbb{C}_{ijkl} F_{sk} \frac{\partial \Delta u_s}{\partial X_l} \right) F_{ri} \frac{\partial \delta u_r}{\partial X_j} \,\mathrm{d}V + \int_{\mathcal{B}_0} S_{ij} \left(\frac{\partial \Delta u_r}{\partial X_i} \right) \frac{\partial \delta u_r}{\partial X_j} \,\mathrm{d}V \,, \tag{3.89}$$

Discretising the domain and using the approximations provided in Equations (3.80) through (3.83) lead to

$$\Delta\mathrm{G} = \bigcup_{e=1}^{n_e} \sum_{I=1}^{n} \sum_{J=1}^{n} \int_{\Omega_e} \left(\mathbb{C}_{ijkl} F_{sk} \Delta u_s^J \frac{\partial N^J}{\partial X_l} F_{ri} \delta u_r^I \frac{\partial N^I}{\partial X_j} + S_{ij} \Delta u_r^J \frac{\partial N^J}{\partial X_i} \delta u_r^I \frac{\partial N^I}{\partial X_j} \right) \mathrm{d}\Omega \,. \tag{3.90}$$

Note that we use $\bigcup$ to denote an assembly process. Similarly, discretising the residual in Equation (3.84) we obtain

$$\mathrm{G} = \bigcup_{e=1}^{n_e} \sum_{I=1}^{n} \int_{\Omega_e} S_{ij} F_{ri} \delta u_r^I \frac{\partial N^I}{\partial X_j} \,\mathrm{d}\Omega - \bigcup_{t=1}^{n_t} \sum_{I=1}^{m} \int_{\Gamma_t} \bar{t}_r^{(\mathbf{n})} \delta u_r^I N^I \,\mathrm{d}\Gamma - \bigcup_{e=1}^{n_e} \sum_{I=1}^{n} \int_{\Omega_e} \rho_0 b_r \delta u_r^I N^I \,\mathrm{d}\Omega = 0 \,, \tag{3.91}$$

where n_t is is the number of element boundaries with traction loads and m is the number of nodes on the traction surface Γ_t.

Finally, combining Equations (3.90) and (3.91), we obtain the final expression for the linearised residual as

$$\mathrm{G}_{k+1} = \delta u_r^I \underbrace{\left\{ \bigcup_{e=1}^{n_e} \sum_{I=1}^{n} \int_{\Omega_e} S_{ij} F_{ri} \frac{\partial N^I}{\partial X_j} \,\mathrm{d}\Omega \right\}}_{[f_r^{int}]} - \delta u_r^I \underbrace{\left\{ \bigcup_{t=1}^{n_t} \sum_{I=1}^{m} \int_{\Gamma_t} \bar{t}_r^{(\mathbf{n})} N^I \,\mathrm{d}\Gamma + \bigcup_{e=1}^{n_e} \sum_{I=1}^{n} \int_{\Omega_e} \rho_0 b_r N^I \,\mathrm{d}\Omega \right\}}_{[f_r^{ext}]}$$
$$+ \delta u_r^I \underbrace{\left\{ \bigcup_{e=1}^{n_e} \sum_{I=1}^{n} \sum_{J=1}^{n} \int_{\Omega_e} \left(\mathbb{C}_{ijkl} F_{sk} \frac{\partial N^J}{\partial X_l} F_{ri} \frac{\partial N^I}{\partial X_j} + S_{ij} \frac{\partial N^J}{\partial X_i} \frac{\partial N^I}{\partial X_j} \delta_{rs} \right) \mathrm{d}\Omega \right\}}_{[K_{rs}]} \Delta u_s^J \,. \tag{3.92}$$

In Equation (3.92) we have indicated the components of the internal force vector $\mathbf{f}^{int}$, the external force vector $\mathbf{f}^{ext}$ and the stiffness matrix $\mathbf{K}$. It is often more convenient for computational purposes to utilise Voigt notation. The Voigt forms of the stiffness matrix and force vectors are derived in Appendix A. In terms of the stiffness matrix and the force vectors, the residual is given as

$$\mathrm{G}_{k+1} = \delta \mathbf{u}^I \cdot \left(\mathbf{f}^{ext} - \mathbf{f}^{int} + \mathbf{K} \Delta \mathbf{u}^J \right) . \tag{3.93}$$

3.7.4 Newton-Raphson Algorithm

Consider the linearised residual in Equation (3.93). If we assume a solution at $\mathbf{u}_{k+1}$ (i.e. $\mathrm{G}_{k+1} = 0$) we find that,

$$0 = \delta \mathbf{u}^I \cdot \left(\mathbf{f}^{ext} - \mathbf{f}^{int} + \mathbf{K} \Delta \mathbf{u}^J \right) . \tag{3.94}$$

Since the virtual displacement is arbitrary, it allows us to write the following,

$$\mathbf{0} = \left(\mathbf{f}^{ext} - \mathbf{f}^{int} + \mathbf{K} \Delta \mathbf{u}^J \right) , \tag{3.95}$$

and we find the displacement increment as

$$\Delta \mathbf{u}^J = -[\mathbf{K}]^{-1} (\mathbf{f}^{ext} - \mathbf{f}^{int}) \,, \tag{3.96}$$

where the force vectors and the stiffness matrix are as defined in Equation (3.92). The displacement is then updated according to

$$\mathbf{u}_{k+1} = \mathbf{u}_k + \Delta \mathbf{u}_k \,. \tag{3.97}$$

Once the solution is updated, a new stiffness matrix and new force vectors are calculated using the new displacement. Equations (3.96) and (3.97) are then repeated iteratively until the displacement increment is sufficiently small. This iterative process is know as the Newton-Raphson method.

We can summarise the basic approach for the Newton-Raphon method as follows,

1. Assume a solution at $\mathbf{u}_{k+1}$, leading to $\mathrm{G}_{k+1} = 0$.
2. Calculate the stiffness matrix $\mathbf{K}$ and the force vectors, $\mathbf{f}^{ext}$ and $\mathbf{f}^{int}$, for the current iteration step using the expressions in Equation (3.92).

3. Calculate the displacement increment with Equation (3.96).
4. Update the displacement with Equation (3.97).
5. Check for convergence:
   (a) if $||\Delta \mathbf{u}_k|| <$ specified tolerance, terminate iteration.
   (b) if $||\Delta \mathbf{u}_k|| >$ specified tolerance, repeat steps 1 through 5 for new values of $\mathbf{u}$.

3.8 Brief Introduction to Curvilinear Coordinates

In previous sections we only dealt with Cartesian tensors, i.e. tensors that are defined in a coordinate system with base vectors $\mathbf{e}_i$ that are unit vectors and mutually orthogonal. However, in some cases it might be advantageous to utilise more general bases, also referred to as curvilinear coordinate systems. For later usage, this section gives a brief introduction to curvilinear bases. Curvilinear bases are often used when the problem domain is of a specific shape, such as a domain that resembles a sphere or cylinder [63].

3.8.1 Base Vectors in a General Curvilinear Coordinate System

Figure 3.6 compares the coordinate curves for a Cartesian coordinate system and a curvilinear coordinate system in the two-dimensional space. As shown, the coordinate curves in a curvilinear system need not necessarily be straight or orthogonal as in the case of a Cartesian system.

Let Θ^i be the curvilinear coordinates where $i = 1, 2, 3$ for the three-dimensional space. The curvilinear base vectors $\mathbf{g}_i$ are tangent to the coordinate curves as illustrated in Figure 3.7. That is

$$\mathbf{g}_i = \frac{\partial \mathbf{x}(\Theta^i)}{\partial \Theta^i} \,, \tag{3.98}$$

where $\mathbf{g}_i$ are the covariant base vectors, denoted with a subscript. The base vectors are non-parallel and are in general neither mutually orthogonal nor of unit length [52].

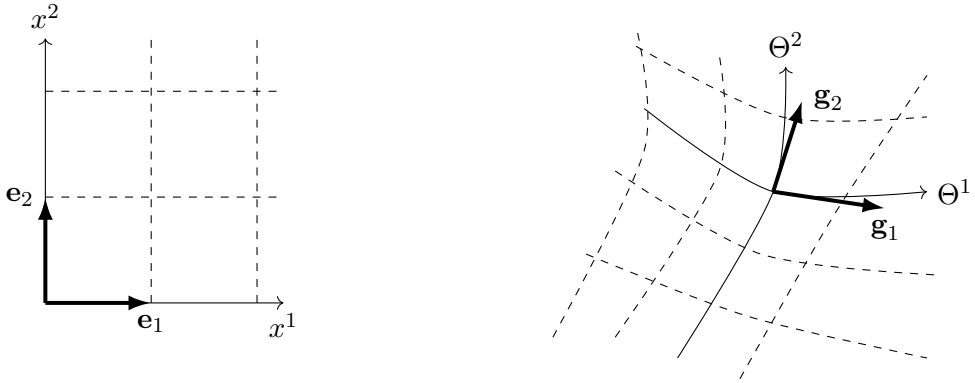

Figure 3.6: Difference between the coordinate curves of (a) a Cartesian coordinate system and (b) a curvilinear coordinate system, adapted from [63].

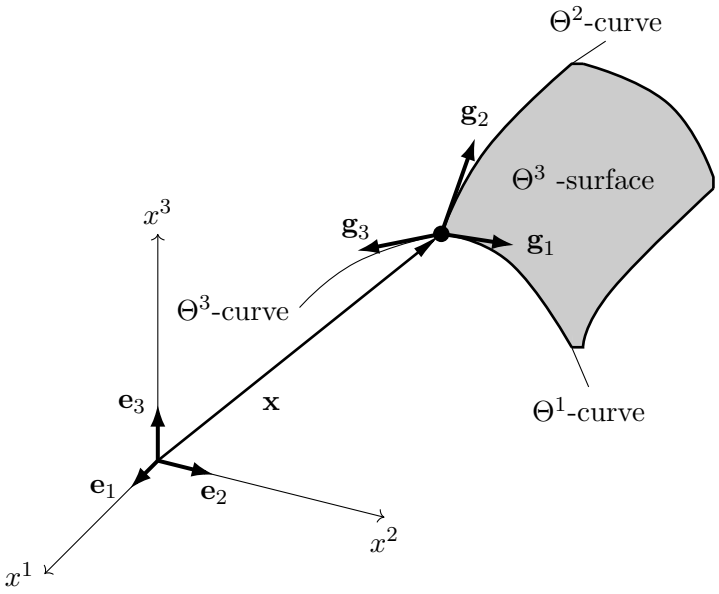

Figure 3.7: The coordinate curve is generated by varying Θ^1 while keeping Θ^2 and Θ^3 constant, modified from [63].

Furthermore, we introduce $\mathbf{g}^i$, the dual (or reciprocal) base of $\mathbf{g}_j$, such that

$$\mathbf{g}^i \cdot \mathbf{g}_j = \delta^i_j = \begin{cases} 1 & \text{if } i = j \\ 0 & \text{if } i \neq j \end{cases} , \tag{3.99}$$

where δ^i_j is the kronecker delta and $\mathbf{g}^i$ are known as the contravariant base vectors. Since the base vectors of a curvilinear system are not necessarily perpendicular, the scalar product of two base vectors is not automatically zero or one. The metric coefficients g_{ij} and g^{ij} describe the geometric properties of the particular basis and are defined as

$$g_{ij} = \mathbf{g}_i \cdot \mathbf{g}_j \,, \qquad g^{ij} = \mathbf{g}^i \cdot \mathbf{g}^j \,. \tag{3.100}$$

When the indices are the same, i.e. $i = j$, we obtain the length of the base vector,

$$g_{ii} = |\mathbf{g}_i|^2 \,, \qquad g^{ii} = |\mathbf{g}^i|^2 \,. \tag{3.101}$$

For different indices, the metric coefficient represents the angle between the base vectors,

$$g_{ij} = |\mathbf{g}_i||\mathbf{g}_j| \cos\theta \,. \tag{3.102}$$

3.8.2 Contraviant and Covariant Components of Vectors and Tensors

A vector $\mathbf{a}$ in the curvilinear space is given by

$$\mathbf{a} = a^k \mathbf{g}_k \,, \tag{3.103}$$

where a^k are the contravariant components of $\mathbf{a}$, denoted with a superscript.

A vector can also be represented using the contravariant base vectors,

$$\mathbf{a} = a_k \mathbf{g}^k \,, \tag{3.104}$$

where a_k are the covariant components of $\mathbf{a}$, denoted with a subscript. Using Equations (3.99) and (3.100), the magnitude of $\mathbf{a}$ is given as

$$|\mathbf{a}| = (\mathbf{a} \cdot \mathbf{a})^{\frac{1}{2}} = (g^{ij} a_i a_j)^{\frac{1}{2}} = (g_{ij} a^i a^j)^{\frac{1}{2}} = (a^i a_j)^{\frac{1}{2}} \,. \tag{3.105}$$

A second-order tensor $\mathbf{A}$ in the curvilinear space is represented as

$$\mathbf{A} = A_{ij} \ \mathbf{g}^i \otimes \mathbf{g}^j = A^{ij} \ \mathbf{g}_i \otimes \mathbf{g}_j = A^i_j \ \mathbf{g}_i \otimes \mathbf{g}^j = A^j_i \ \mathbf{g}^i \otimes \mathbf{g}_j \,, \tag{3.106}$$

where A_{ij}, A^{ij}, A^i_j and A^j_i are respectively the covariant, contravariant, right-covariant mixed and left-covariant mixed components of $\mathbf{A}$.

If the base vectors are unit vectors and orthogonal, as in a Cartesian system, then $\mathbf{g}_i$ and $\mathbf{g}^i$ coincide and therefore $\mathbf{g}_i = \mathbf{g}^i$. Cylindrical and spherical coordinate systems are also special cases of curvilinear systems where the base vectors are orthogonal.

3.9 Summary of Continuum Mechanics

In this chapter we introduced the concept of a tensor which was defined as a linear map between two other tensors. We reviewed the kinematics of a continuum body and presented several tensors commonly used to measure the stress and deformation experienced by a continuum. We also derived the continuity equation from the balance of mass as well as Cauchy's first equation of motion from the balance of linear momentum.

We noted that biological tissues are typically modelled as hyperelastic materials. For this reason we discussed strain energy functions as well as isotropic, transversely isotropic and orthotropic materials. These are typically formulated in terms of the scalar invariants of the strain tensor. Additionally, we described the finite element method that is used to obtain approximate solutions to the governing equation. Finally, we gave a brief overview of curvilinear coordinate systems.

Chapter 4

Computational Cardiac Modelling

Computational cardiac modelling deals with mathematical representations of the heart and using computational resources to simulate the heart's behaviour. The literature is abundant with research dedicated to computational cardiac models. Each cardiac model has a specific purpose, such as investigating the electrophysiology, analysing the mechanical behaviour or simulating the electromechanical coupling in cardiac tissue. The present work focuses on the biomechanical behaviour of the heart. This chapter, therefore, is aimed at providing a literature review of the main components required to create a biomechanical model of the heart. The reader is referred to Perez et al. [76] who compiled a list of cardiac models developed over a time period spanning nearly half a century. Apart from discussing a variety of applications of cardiac models, Perez et al. also provide a general overview of whole heart modelling.

The mechanical behaviour of cardiac tissue is often separated into two parts, a passive and an active component. The passive component is related to the elastic behaviour of cardiac tissue, while the active response is a result of the ability of cardiac tissue to generate its own tension when stimulated. This chapter presents a number of material models from the literature that are used to model passive cardiac tissue. In addition to these material models, methods to simulate the active response are also discussed. We also highlight some of the approaches used to approximate the left and right ventricular geometries. Finally, this chapter concludes with a discussion on the Windkessel model, a popular lumper-parameter model that allows one to model the interaction between the ventricles and the arterial system.

4.1 Modelling the Passive Behaviour of Cardiac Tissue

During diastole the heart behaves passively, i.e cardiac muscles fibres are in a state of rest and are not electrically activated. A classical continuum model is a popular choice when it comes to modelling the elastic behaviour of biological tissue. In this section we first consider some experimental findings related to cardiac tissue and secondly, we provide a number of classical continuum material models for passive heart behaviour.

4.1.1 Experimental Findings

Prior to the study by Demer and Yin [21], material models were mainly based on uniaxial material test data. Because of the environment in which the heart operates, cardiac tissue is subjected to

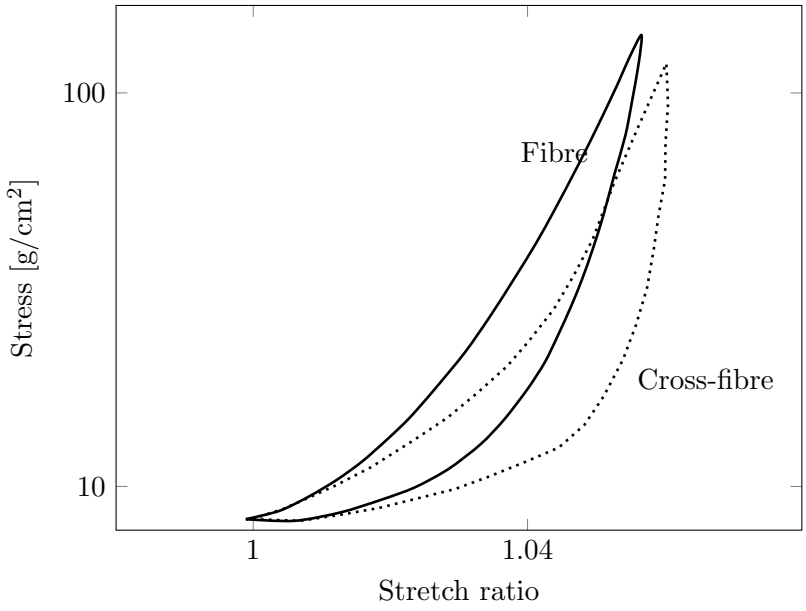

Figure 4.1: Stress-stress curve for cardiac tissue subjected to biaxial loading conditions, reproduced from [21].

multiaxial loading. Therefore, measured data from uniaxial studies are inadequate and cannot be extended to describe the behaviour of the intact heart [21]. Demer and Yin [21] and Yin et al. [139] studied the mechanical properties of the heart by subjecting sheets of cardiac tissue to loading in the fibre and the cross-fibre direction, i.e. biaxial loading. Figure 4.1 provides the stress-strain curve for one of the specimens from [21]. The results show that the material response in the fibre direction is different from that in the cross-fibre direction. This is indicative of anisotropic behaviour. From biaxial studies, Demer and Yin [21] and Yin et al. [139] concluded that cardiac tissue exhibits viscoelastic behaviour, is highly non-linear and behaves stiffer when subjected to biaxial loading than uniaxial loading.

Although biaxial material testing highlights some anisotropic features, biaxial test data does not necessarily provide a complete description of the myocardial response. LeGrice et al. [72] used scanning electron microscopy to investigate the arrangement of cardiac muscle fibres in the heart, specifically the architecture of cardiac muscle sheets. The study confirmed the existence of discrete tissue layers in the ventricular wall. Each layer contained tightly connected heart muscle fibres and was loosely connected to its adjacent layers. The study by LeGrice et al. [72] suggests that the heart has an orthotropic material structure. That is, the laminar structure can be characterised locally with three orthogonal directions: the fibre direction, the cross-fibre or sheet direction and the sheet-normal direction. LeGrice et al. also found that the myocardium is not a homogeneous structure. They observed a variation in the branch density, number of branches and perimysial fibre length across the ventricular wall.

Because of the orthotropic nature of cardiac tissue, deformations measured from uniaxial and biaxial testing data are not sufficient to characterise the response of the myocardium [19, 53, 56]. Holzapfel and Ogden [53] proposed the use of a combination of measured data from biaxial and shear tests for a more complete description of cardiac material properties.

Other studies have also verified the orthotropic nature of cardiac tissue. Dokos et al. [23] performed shear tests on samples of cardiac tissue obtained from pig hearts. The samples, consisting of $3 \times 3 \times 3$ mm blocks, were taken from the mid-wall of the left ventricle with the edges aligned with the local material directions. The shear deformation modes are illustrated in Figure 4.2(a). The experimental results, reproduced in Figure 4.2(b), show that the shear properties depend on the loading direction. Note that, according to Holzapfel and Ogden [53], the FS and FN labels are not consistent with the other graphs in the paper, therefore these two labels are switched. A similar study, conducted by Sommer et al. [113], was performed on human heart specimens to determine tri-axial shear properties with similar findings to that of [23].

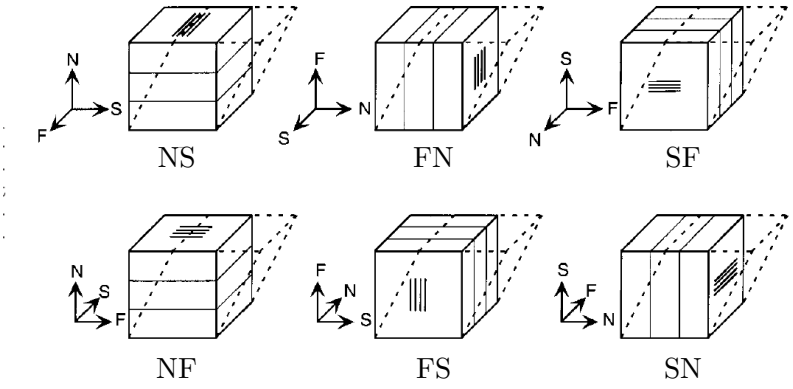

(a)

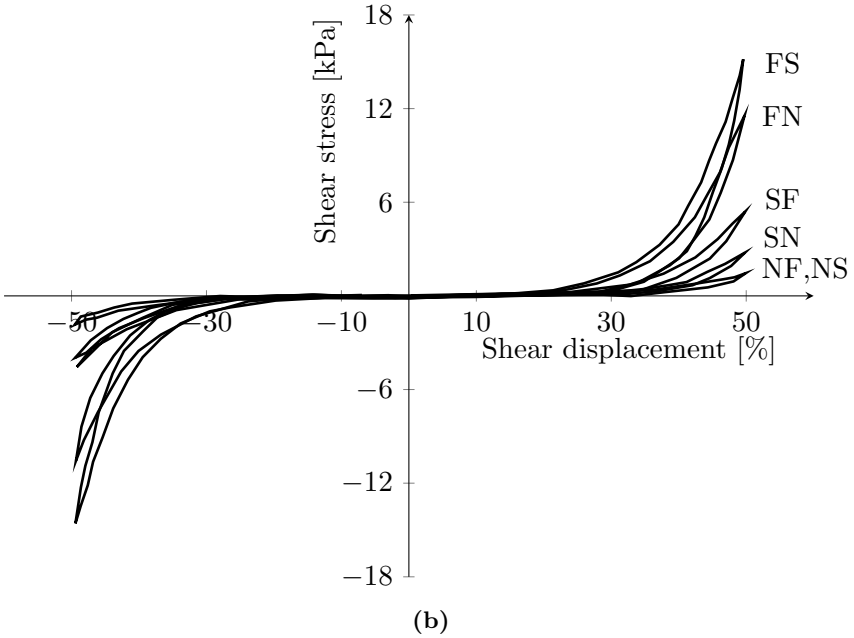

(b)

Figure 4.2: Results form tri-axial experiments performed on pig myocardium, including the (a) shear deformation modes where F, S and N are fibre, sheet and normal directions respectively and (b) the non-linear relationship between stress and deformation for the different deformation modes, reproduced from [23].

4.1.2 Classical Continuum Models

From experimental data and morphological studies we know that cardiac tissue is an anisotropic material. Isotropic material models, such as those used by Mirsky [81], Demiray [22] and Wong [133], are therefore inappropriate to describe the behaviour of the heart. In this section we review only transversely isotropic and orthotropic models.

Transversely Isotropic Model by Humphrey and Yin [56]

Transversely isotropic models assume that the material behaviour depends only on the fibre direction, but not on the sheet or sheet-normal directions.

As stated in Chapter 2, a mathematical model for cardiac tissue should take into account the contributions from the muscle fibres as well as the extracellular matrix that surrounds the fibres [3, 37]. Humphrey and Yin [56] proposed a phenomenological strain energy function of the form

$$\psi = \psi_m(\mathbf{C}) + \psi_f(\lambda)\,, \tag{4.1}$$

where ψ_m and ψ_f are the energy contributions from the surrounding matrix and muscle fibres respectively. ψ_m is a function of the the right Cauchy-Green deformation tensor $\mathbf{C}$ while ψ_f is taken to be a function of the fibre stretch λ. In this way the surrounding matrix contribution is assumed to be isotropic while the fibre contribution represents the transversely isotropic component of the strain energy function. The strain energy function of Humphrey and Yin is given by

$$\psi = \underbrace{c(e^{b(I_1-3)}-1)}_{\psi_m} + \underbrace{A(e^{a(\lambda^2-1)^2}-1)}_{\psi_f}\,, \tag{4.2}$$

where c, b, A and a are material parameters. Because this model is phenomenological, the parameters do not necessarily have any physical meaning.

Transversely Isotropic Model by Guccione et al. [46]

A commonly-used strain energy function for soft biological tissue is a Fung-type model [38], which has the form

$$\psi_{fung} = \frac{C}{2}(e^Q - 1)\,, \tag{4.3}$$

where Q is a function of the Green-Lagrange strain tensor $\mathbf{E}$. To quantify the material properties of the intact myocardium, Guccione et al. [46] based their transversely isotropic material model on the Fung-type strain energy function. The strain energy in [46] is given by Equation (4.3) with Q defined as

$$Q = 2b_1(E_{rr}+E_{ff}+E_{cc}) + b_2E_{ff}^2 + b_3(E_{cc}^2+E_{rr}^2+E_{cr}^2+E_{rc}^2) + b_4(E_{rf}^2+E_{fr}^2+E_{fc}^2+E_{cf}^2)\,, \tag{4.4}$$

where b_i are material parameters and E_{ij} are the components of the Green-Lagrange strain tensor. The indices f, r and c refer to the fibre, radial and cross-fibre directions.

Orthotropic Model by Usyk et al. [122]

Orthotropic material models for cardiac tissue improve on transversely isotropic models since they capture the distinct responses in the fibre, cross-fibre and normal directions [86]. The study conducted by LeGrice et al. [72] supports the view that transversely isotropic material models are not necessarily sufficient to describe the behaviour of the intact heart.

Usyk et al. [122] modelled the myocardium as an orthotropic and nearly incompressible material using the following strain energy function,

$$\psi = \frac{C}{2}(e^Q - 1) + C_{comp}(J \ln J - J + 1), \tag{4.5}$$

with

$$Q = b_{ff}E_{ff}^2 + b_{ss}E_{ss}^2 + b_{nn}E_{nn}^2 + b_{fs}(E_{fs}^2 + E_{sf}^2) + b_{fn}(E_{fn}^2 + E_{nf}^2) + b_{ns}(E_{ns}^2 + E_{sn}^2), \tag{4.6}$$

where J is the Jacobian and b_{ij} are material constants. The second term in Equation (4.5) is included to ensure nearly-incompressible behaviour. The subscripts f, s and n refer to the fiber, sheet and sheet-normal axes respectively. Usyk et al. compared the orthotropic model to the transversely isotropic model described in [46] and found that the orthotropic model produced results that were in better agreement with experimental data.

Orthotropic Model by Holzapfel and Ogden [53]

Holzapfel and Ogden [53] developed a material model based on the orthotropic structure of heart tissue. The strain energy function is given by

$$\psi = \frac{a}{2b}e^{b(I_1-3)} + \sum_{i=f,s}\frac{a_i}{2b_i}\left(e^{b_i(I_{4i}-1)^2} - 1\right) + \frac{a_{fs}}{2b_{fs}}\left(e^{b_{fs}I_{8fs}^2} - 1\right). \tag{4.7}$$

The invariants I_{4f} and I_{4s} are measures of strain in the fibre direction $\mathbf{V}_f$ and the sheet direction $\mathbf{V}_s$,

$$I_{4f} = \mathbf{V}_f \cdot (\mathbf{C}\mathbf{V}_f), \qquad I_{4s} = \mathbf{V}_s \cdot (\mathbf{C}\mathbf{V}_s). \tag{4.8}$$

The invariant I_{8fs} accounts for the shear between the sheet and the fibre direction,

$$I_{8fs} = I_{8sf} = \mathbf{V}_f \cdot (\mathbf{C}\mathbf{V}_s). \tag{4.9}$$

The first term in Equation (4.7) is associated with the isotropic behaviour of the matrix material. The invariants I_{4f} and I_{4s} account for the transversely isotropic behaviour and I_{8fs} accounts for the orthotropic nature of cardiac tissue. The material parameters a, b, a_f, a_s, b_f, b_s, a_{fs} and b_{fs} are positive constants that can be obtained by fitting the material law to experimental shear data.

4.2 Active Behaviour of Cardiac Tissue

To understand the behaviour of the heart we need to characterise both passive and active properties [139]. As discussed in Chapter 2, an electrical impulse travels across the heart resulting in ventricular contraction. The focus of this research is not on modelling the conduction system or the distribution of the impulse, but rather on the mechanical behaviour caused by the contraction, i.e. the resulting stresses and deformation caused by the contracting muscle fibres.

The stress resulting from the contraction of fibres can be included in one of two ways [2, 42]. In the first approach, the *active-stress* method, the total stress $\boldsymbol{\sigma}$ is additively decomposed into active and passive stress parts,

$$\boldsymbol{\sigma} = \boldsymbol{\sigma}_p + \boldsymbol{\sigma}_a \,, \tag{4.10}$$

where $\boldsymbol{\sigma}_p$ and $\boldsymbol{\sigma}_a$ are the passive and active stress components respectively. The passive material behaviour is determined in the absence of the active behaviour. That is, a strain energy function is obtained without including the active component. The active component is then simply included in the balance of linear momentum. The equilibrium equation for a classical continuum therefore reads

$$\mathrm{div}(\boldsymbol{\sigma}_p + \boldsymbol{\sigma}_a) + \rho\mathbf{b} = 0 \,. \tag{4.11}$$

A second, less common approach, is to adopt a method of multiplicatively decomposing the deformation gradient,

$$\mathbf{F} = \mathbf{F}_e\mathbf{F}_a \,, \tag{4.12}$$

where $\mathbf{F}$ is the total deformation gradient and $\mathbf{F}_e$ and $\mathbf{F}_a$ represent the deformations of the passive and active contributions. This is referred to as an *active-strain* approach. A number of active-stress and active-strain models are reviewed by Ambrosi and Pezzuto [2].

Although the active-strain approach is considered to be more robust [2], we only consider active-stress models here. The reader is referred to [42, 83, 92, 117] for examples of active-strain models. The active-stress approach has the advantage that the material parameters for the passive and active models can be determined independently, i.e. from different experimental datasets. Passive material parameters are obtained from experiments where there is no electrical stimulation of the cardiac muscle fibres and likewise, the active parameters are determined from experiments where the passive parameters are fixed [42].

Hill model

A number of earlier models describing muscle mechanics were based on the well-known Hill model [50]. Hill's equation, which gives a relationship between force and velocity, reads

$$(v + b)(P + a) = b(P_0 + a), \tag{4.13}$$

where v is the contraction velocity, P is the muscle tension and P_0, a and b are constants. There are several issues with this model as noted by Fung [37]: single muscle twitches, unstimulated muscle behaviour and muscle subjected to time-varying strain cannot be described with Hill's equation.

An improvement on Hill's equation is Hill's three-element model, illustrated in Figure 4.3. The three-element model represents the muscle with a contractile element connected in series with a non-linear spring component. These two components are arranged in parallel with another non-linear spring element, which represents the behaviour of the muscle at rest. The contractile element is responsible for muscle shortening, while the muscle stress is determined by the two non-linear spring elements [36]. This approach allows the total stress to be additively decomposed into active and passive components [42]. A more detailed analysis of the Hill model is found in [37].

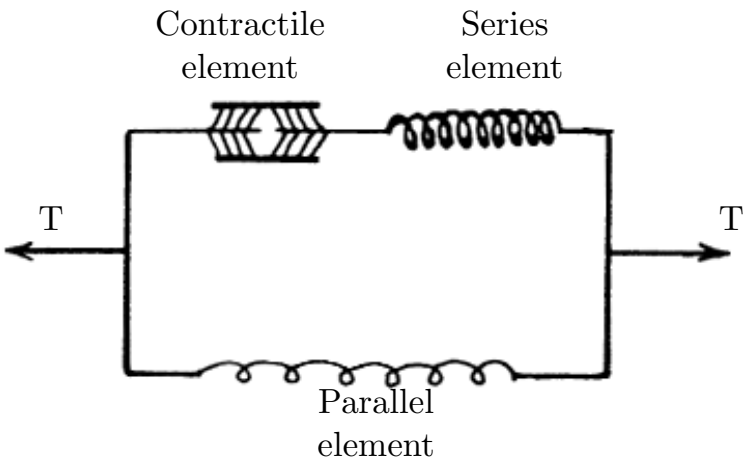

Figure 4.3: Hill's three element model for muscle, from [37].

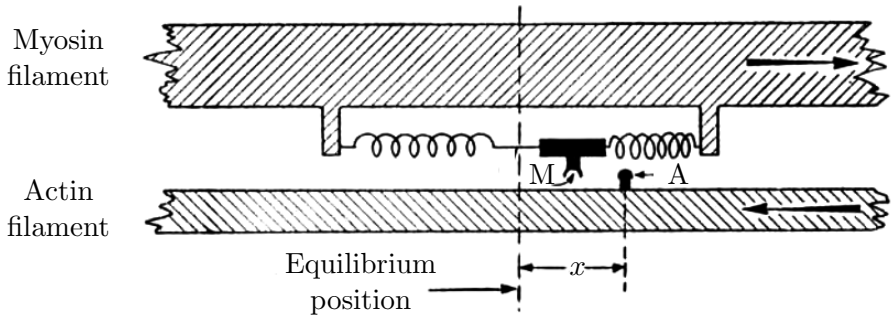

Figure 4.4: Schematic diagram of Huxley's model adapted from [58]. A denotes the binding site and M the myosin head.

The classical Hill model is unsuitable for modelling the active behaviour of cardiac tissue [37, 45]. Despite its shortcomings, some authors have successfully adapted the Hill model to simulate the contraction of the heart. For example, Göktepe et al. [42] generalised the Hill model to accommodate large strains. They used a combination of the active-stress and the active-strain approach: Göktepe et al. not only additively decomposed the strain energy function but also multiplicatively decomposed the deformation gradient into passive and active parts. Göktepe et al. showed that their approach can be employed successfully to model the excitation-contraction of the heart.

Huxley's model

Huxley's model [58] for muscle contraction is based on the sliding filament theory discussed in Chapter 2. From the sliding filament theory we know that muscle contraction depends amongst other things on crossbridge attachment. The rate of crossbridge attachment in Huxley's model is determined by the relative position of the actin-binding site to the nearest crossbridge (or myosin head), see x in Figure 4.4. The crossbridge force is taken to be a linear function of displacement and the crossbridges, therefore, act as springs [58, 99]. Both the Hill model and Huxley model predict a hyperbolic force-velocity relationship.

Elastance Model by Guccione et al. [47]

Guccione and McCulloch [45] derived a constitutive relation for active cardiac tissue that describes isometric[1] and isotonic[2] contractions as well as the so-called deactivation phenomenon observed in cardiac tissue. Guccione et al. [47] evaluated this deactivation model and also considered two simplifications of the model, namely a Hill and a time-varying elastance model. They found that, although the complex deactivation model is considered more accurate, the mechanical behaviour of this complex model was similar to that of the less complicated Hill and elastance models.

Because of its simplicity, the elastance model is often the preferred approach [19]. The elastance model assumes that all the fibres contract simultaneously and that the active stress T_A is a function of the peak intracellular calcium concentration Ca_0, the maximum peak intracellular calcium concentration $(Ca_0)_{max}$ and the sarcomere length l,

$$T_A = T_{max}\frac{Ca_0^2}{Ca_0^2 + ECa_{50}^2}C_t \qquad \text{with} \qquad ECa_{50} = \frac{(Ca_0)_{max}}{\sqrt{e^{B(l-l_0)}-1}}\,, \tag{4.14}$$

where B is a constant and C_t is defined as

$$C_t = \frac{1}{2}(1-\cos\omega) \tag{4.15}$$

$$\omega = \begin{cases} \pi\frac{t}{t_0} & \text{if } 0 \le t < t_0 \\ \pi\frac{t-t_0+t_r}{t_r} & \text{if } t_0 \le t < t_0 + t_r \\ 0 & \text{if } t_0 + t_r \le t \end{cases} \tag{4.16}$$

where t is the time after contraction has started and t_0 is the time required to reach the peak tension. The relaxation duration t_r is given by $t_r = ml + b$, where m and b are constants. The sarcomere length is given by

$$l = l_R\sqrt{2E_{ff}+1} \qquad \text{with} \qquad E_{ff} = \mathbf{E} : \mathbf{V}_f \otimes \mathbf{V}_f\,, \tag{4.17}$$

where $\mathbf{V}_f$ and l_R are the fibre direction and the sarcomere length in the reference configuration.

Figure 4.5 compares the elastance model to measured active tension data. The figure shows the active tension during a contraction in which the sarcomere length is kept constant. The tension development was computed for different sarcomere lengths. GNU Octave was used to compute the active tension and the material constants were chosen in accordance with [47]: $Ca_0 = 4.35\,\mu M$, $(Ca_0)_{max} = 4.35\,\mu M$, $B = 4.75\,\mu\text{m}^{-1}$, $l_0 = 1.58\,\mu\text{m}$, $m = 1.0489\,s\mu\text{m}^{-1}$ and $b = -1.429\,s$. The curves indicate good correlation between the model and experimental measurements.

The active tension is largest along the longitudinal axis of the cardiac fibre [74]. Consequently, a number of models assume that the active tension develops only in the fibre direction [47, 137],

$$\boldsymbol{\sigma}_{A(local)} = T_A\,\mathbf{v}_f \otimes \mathbf{v}_f\,, \tag{4.18}$$

where $\boldsymbol{\sigma}_{A(local)}$ is the active stress tensor in the local coordinate system and $\mathbf{v}_f$ is the fibre direction in the current configuration.

[1] Isometric contraction: contraction at a constant length.
[2] Isotonic contraction: contraction at a constant tension.

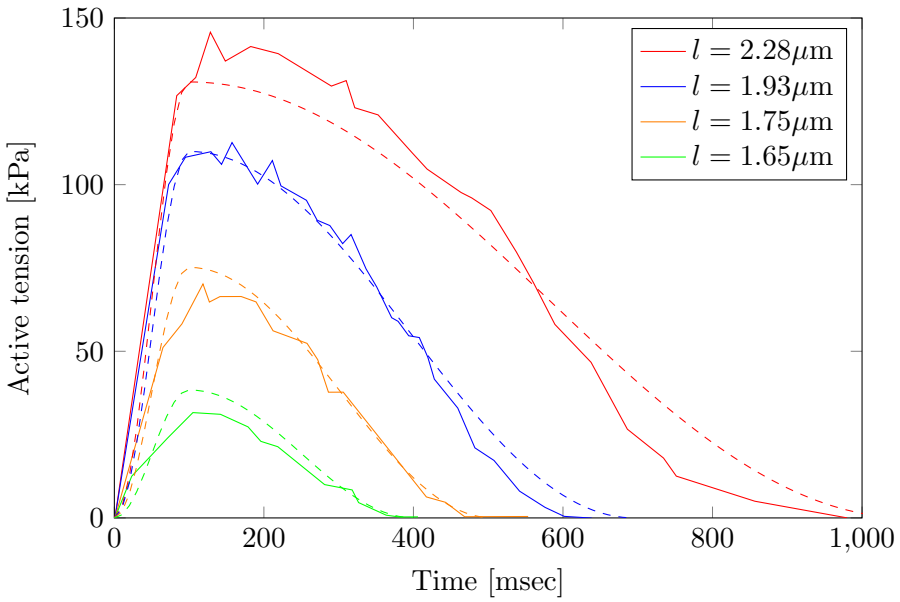

Figure 4.5: Measured active tension (solid lines) from Van Heuningen et al. [127] and the predicted isometric tension (dashed lines) for different sarcomere lengths using the elastance model by Guccione et al. [47].

Some studies have shown that significant tension also develops in the transverse direction (cross-fibre direction) [74, 130]. In most cases the transverse stress is specified to be 40% of the tension in the fibre direction, that is,

$$\boldsymbol{\sigma}_{A(local)} = T_A \, \mathbf{v}_f \otimes \mathbf{v}_f + 0.4 T_A \, \mathbf{v}_s \otimes \mathbf{v}_s \, , \tag{4.19}$$

where $\mathbf{v}_s$ is the cross-fibre direction.

4.3 Heart Geometry

The relationship between the wall stresses of the ventricles and the cavity pressure depends amongst other factors on the chosen geometry [3, 79]. Much of the earlier literature is devoted to investigating the behaviour of the left ventricle. It was only after the improvement of computational resources and imaging modalities that the right ventricle started to appear in cardiac models.

4.3.1 Modelling the Left Ventricle

Simple shapes, such as spheres and cylinders, were first used to investigate left ventricular mechanics. Studies that assume a spherical geometry for the left ventricle include those by Holt et al. [51], Rodbard [102] and Mirsky [81]. Cylindrical models allowed investigators to include the fibre direction and anisotropic material properties. These models made it easier to study large deformations and did not require complicated computational methods, such as finite element methods [47]. Cylindrical models consist of thick-walled cylinders that represent the equatorial region of the left ventricle. These simple models were fairly popular and were used in a number of cardiac models, see for example [3, 46, 47, 57, 60, 126]. Even though the cylindrical model is considered

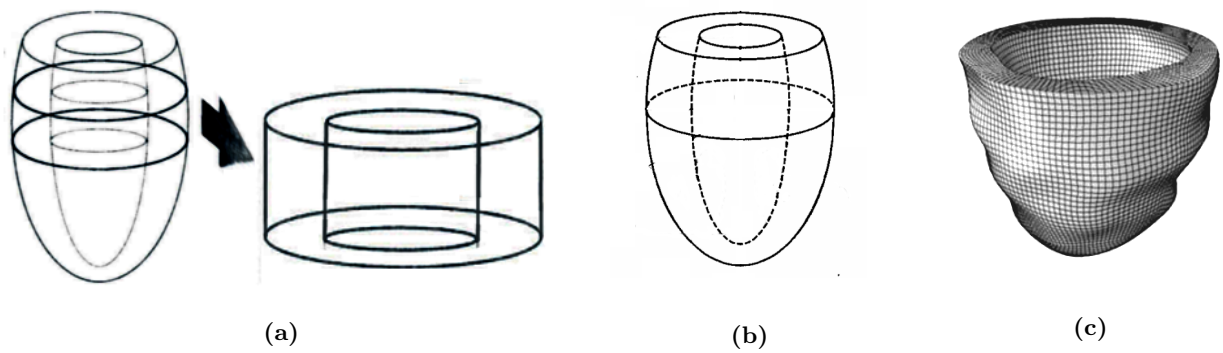

(a) (b) (c)

Figure 4.6: Geometries used to represent the left ventricle include (a) thick-walled cylindrical models only valid if restricted to the equatorial region, from [46] (b) ellipsoidal models, adapted [6] and (c) image-based geometries, from [131].

an improvement on the spherical model [126], results obtained from a cylindrical model can only be used to describe the behaviour of regions close to the equatorial area of the left ventricle [47].

In more recent studies, the left ventricle is often modelled by an ellipse truncated at its top to resemble the base of the heart. Van den Broek and Van den Broek [125] investigated left ventricular contractions with a thick-walled ellipsoidal model. The model consisted of layers and each layer was endowed with a different fibre orientation to simulate the change in fibre angle as one traverse the heart wall. Other studies that used ellipsoidal models include [59, 114, 115, 116, 122, 133]. Because the ellipsoidal geometry approximates the base and equatorial region better than the apical region, the computed deformations near the base and equator are in closer agreement with measured data compared to deformations computed at the apex [122]. Figure 4.6 illustrates examples of cylindrical and ellipsoidal models.

The use of medical imaging modalities allows for accurate reconstruction of the heart geometry. Computed tomography images were utilised by Ordas et al. [88] to construct a statistical shape of the whole human heart. Vinson et al. [128] estimated the three-dimensional geometry of the left ventricle using biplane angiography. Magnetic resonance imaging is another imaging tool widely used to develop three-dimensional models [20]. Figure 4.6(c) shows a finite element mesh that was used in a patient-specific study of the left ventricle. The mesh was created using magnetic resonance images.

4.3.2 Bi-Ventricular Models

A bi-ventricular model includes both the left and right ventricles. One of the most popular methods to create bi-ventricular geometries is with ellipsoids. An idealised bi-ventricular model consists of two ellipsoids truncated at their tops, as shown in Figure 4.7(a). Some of the studies that employ this method include [41, 93, 111]. As in the case of the left ventricle, medical imaging modalities can also be used to create bi-ventricular models. Figure 4.7(b) presents a bi-ventricular model that was reconstructed from magnetic resonance images.

4.3.3 Myocardial Fibre Orientation

One of the major goals in computational cardiac modelling is to gain insight into how the tissue structure affects the pumping performance of the heart [84]. When modelling the mechanical

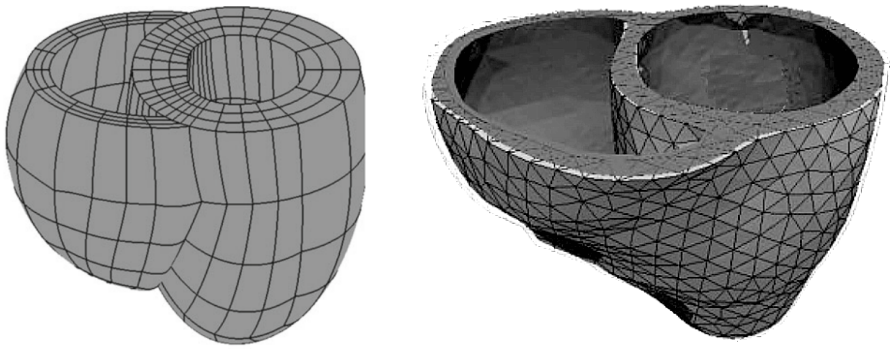

(a) **(b)**

Figure 4.7: Different geometries for bi-ventricular heart models, including (a) a generic bi-ventricular model that approximates both ventricles as two truncated ellipsoids, from [93] and (b) an image based model used for patient specific simulations, from [31].

action of the heart, two important quantities are deformation and stress [123]. Non-linear finite element modelling of the left ventricle performed by Van Campen et al. [123] and Bovendeerd et al. [6] showed that the spatial variation of the wall stress depends on the orientation of the cardiac muscle fibres in the ventricle.

The fibre orientation is assigned either through rule-based or image-based approaches [4]. Rule-based methods are based on mathematical expressions that describe the fibre direction, while imaging techniques typically use diffusion tensor imaging (DTI) to obtain the fibre arrangement. DTI is based on measurements of the diffusion of water molecules in biological tissues [87, 112]. Because diffusion in tissues depends on the fibre direction, DTI gives information about the degree of anisotropy and the structural layout of the fibres [112]. DTI is often applied in studies to characterise brain tissue [1] but can also be used to obtain the fibre arrangement in the heart, see for example [35, 39, 91].

Bayer et al. [4] developed a Laplace-Dirichlet rule-based algorithm that was used to define the fibre arrangement in a cardiac model. The method is based on solving the Laplace equation with Dirichlet boundaries. Figure 4.8 compares the DTI-derived fibre orientation with the rule-based method developed by Bayer et al. Wong and Kuhl [135] utilised Poison interpolation to generate a vector field that described the fibre direction. Wong and Kuhl successfully applied this method to a bi-ventricular heart as well as a patient-specific heart, thereby demonstrating the flexibility and robustness of their method.

4.4 Hemodynamics

Although diastolic filling, isovolumetric contraction and isovolumetric relaxation are modelled using pressure loads and deformation constraints, see for example [111], there are a number of possibilities to simulate blood ejection. These typically include models that describe the interaction between the ventricles and the arterial system. The objective for this study is not to model the wave propagation, pressure or flow within the arterial tree, but rather the flow of blood from the ventricles and the corresponding effect on the ventricular pressure and volume.

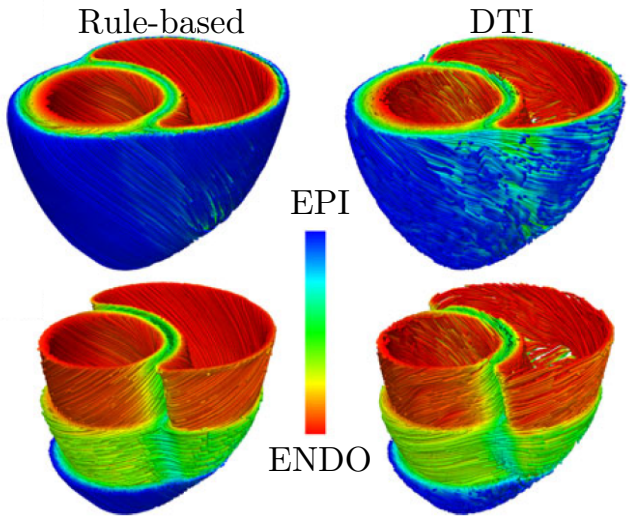

Figure 4.8: Longitudinal fibre direction obtain from diffusion tensor imaging and a rule-based method, from [4].

Among the simpler models that are used to incorporate the arterial system are tube and lumped parameter models [70]. In the former, an elastic or viscoelastic tube is used to model the arterial tree [12]. The tube has an effective length and is either straight or tapered. Tube models can account for the elasticity of the arterial walls as well as its geometry [124].

A widely used lumped parameter model is the Windkessel model. The arterial Windkessel model draws an analogy between the flow of blood from the heart and an electrical circuit, see Table 4.1. A Windkessel model describes the arterial system with resistances, capacitors and inductors, with each of these components representing a different feature of the arterial system [70]. Since we are only interested in the overall effect of the arterial system, the Windkessel model is sufficient [124] and is therefore discussed in more detail below.

The two-element Windkessel or Frank model, formulated by Frank Otto [34], is the simplest form of the Windkessel model. The two-element circuit consists of a resistive and a compliant element. As blood is ejected, small arterioles and capillaries resist the flow of blood [124]. The peripheral resistance R in the circuit represents the sum of all the individual resistances. The large compliant arteries are thought of as chambers and are represented by the capacitor C. The current I(t) and potential difference P(t) are analogous to blood flow and the aortic pressure respectively. The two-element model predicts the aortic pressure decay during diastole as

$$\mathrm{P(t)} = \mathrm{P}_0 e^{-\frac{\mathrm{t}}{RC}} \,, \tag{4.20}$$

where P_0 is the end-systolic pressure, or the pressure at the start of diastole. To improve the predicted relation between pressure and blood flow, a third element, the characteristic impedance Z_c, is added. This component represents the impedance of the aorta, but is also sometimes thought of as the resistance that the flow encounters as it moves through the semilunar valve [132]. The expression that governs the flow and pressure is given by

$$\big(1 + \frac{Z_c}{R}\big)\mathrm{I(t)} + CZ_c\frac{\mathrm{dI(t)}}{\mathrm{dt}} = \frac{\mathrm{P(t)}}{R} + C\frac{\mathrm{dP(t)}}{\mathrm{dt}} \,. \tag{4.21}$$

Table 4.1: Hydraulic and electrical representations of the two- and three-element Windkessel models, figures adapted from [132].

	2-element Windkessel	3-element Windkessel
Hydraulic analogue	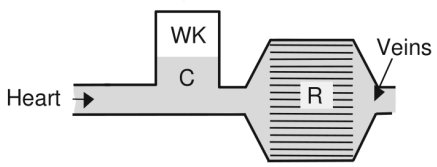	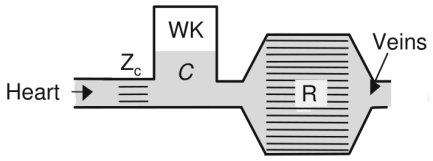
Electrical analogue	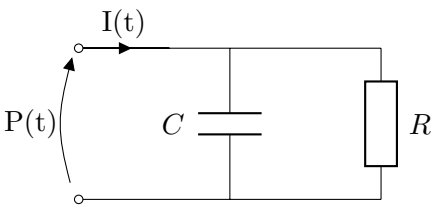	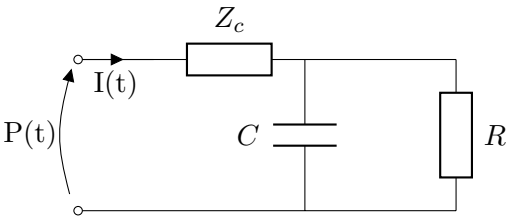

4.5 Summary of Computational Cardiac Modelling

Material testing and morphological studies show that the myocardium is a heterogeneous structure that exhibits non-linear and anisotropic material behaviour. This chapter listed a number of constitutive laws to describe the behaviour of cardiac tissue, including the transversely isotropic model by Humphrey and Yin [56], the Fung-type model by Guccione et al. [46] and the orthotropic models by Usyk et al. [122] and Holzapfel and Ogden [53].

There exists a variety of mathematical models that can be employed to simulate the active contraction of cardiac fibres. We noted that the active tension is typically included using either an active-stress or an active-strain approach. In Section 4.2 we presented three models to simulate the active behaviour, namely the Hill model, Huxley's model and the elastance model by Guccione et al [47].

In this chapter we also discussed the heart geometries used in cardiac models. Initially, the left ventricle was approximated using simple geometric shapes, however recent studies employ imaging techniques to obtain the realistic geometries of the heart chambers.

Chapter 5

Introduction to Micromorphic Modelling

Classical continuum mechanics can be applied to describe a variety of macroscopic phenomena. However, classical theories are often inadequate when dealing with phenomena that occur on lower scales. To address this issue, one can utilise so-called generalised continuum theories. Generalised continuum theories are well suited to describe materials with granular or fibrous structures [138]. According to Madeo [77], there are two methods with which classical theories may be generalised. In the first, the kinematic expressions remain the same but the chosen constitutive law depends on higher gradients of the displacement field. In the second method, the kinematic expressions are extended by adding additional degrees of freedom to the existing displacement degrees of freedom. In this chapter we consider the microcontinuum, a specific case of the latter approach.

Microcontinuum theories enhance the classical approach by attaching additional vectors (called directors) to the continuum particle. The directors allow one to describe the micro-deformation of the particle. Therefore, a microcontinuum is often described as a body that consists of a continuous set of deformable particles [27]. This approach makes it possible to account for the deformation of micro-constituents since the continuum particles themselves are now considered deformable.

A simple method to determine whether the microcontinuum theory is appropriate is to consider the ratio of the characteristic length L of the continuum and its intrinsic length λ [27]. If the characteristic length is much greater than the intrinsic length, i.e. $\frac{L}{\lambda} > 1$, then a classical continuum formulation is appropriate and will give reasonable results. If, however, the two lengths are comparable, i.e. $\frac{L}{\lambda} \approx 1$, then a classical formulation will give erroneous results since the micro-constituents in this case will have a significant effect on the macroscopic behaviour of the body.

We propose the use of a micromorphic model, a subclass of the microcontinuum, to describe the passive response of cardiac tissue. The goal of this chapter is to give a brief introduction to the micromorphic theory and to outline the kinematics and strain measures. The theory discussed in the remainder of this chapter is heavily based on the works of Sansour et al. [109] and Von Hoegen et al. [129].

5.1 The 3M Continua

The term *3M continua* refers to the three subclasses of the microcontinuum, namely micropolar, microstretch and micromorphic. As mentioned before, to include the micro-deformation of a continuum particle, we attach directors to the particle and as a consequence introduce additional degrees of freedom. The microcontinuum subclass depends on how these directors are allowed to deform [27].

A microcontinuum whose material particles are allowed to experience micro-stretch, micro-rotation and micro-shear is referred to as a micromorphic continuum. This is the most general case of the microcontinuum. When a micromorphic continuum is constrained such that its particles experience only micro-rotation and micro-stretch it is referred to as a microstretch continuum. If the microcontinuum is further restricted to only allow rigid rotation of the particle, it is known as a micropolar or Cossarat continuum.

The idea of adding additional degrees of freedom was first presented in the seminal work of the Cosserat brothers [18]. Their approach was extended by Eringen [27, 29] and Mindlin [80] to the micromorphic theory.

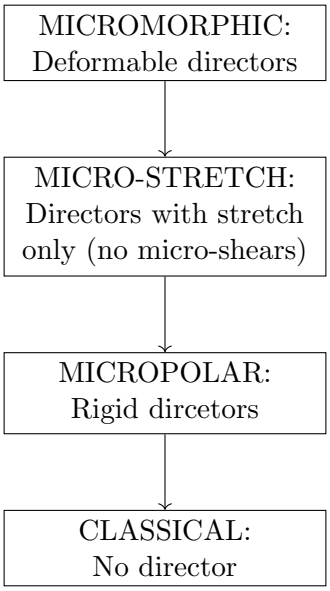

Figure 5.1: Diagram illustrating the different subclasses of the microcontinuum, from [27] . The directors of a micropolar (or Cosserat) continuum are rigid. A particle is only allowed to rotate. A microstretch continuum has directors that can experience micro-stretch and micro-rotation. A particle in a micromorphic continuum is allowed to rotate, stretch and experience micro-shear.

5.2 Non-Affine Deformation of Biological Tissue

Classical continuum models assume that a continuum body experiences affine deformation [66]. Therefore, the material models discussed in Chapter 4 predict that cardiac muscle fibres orientate and deform along with the matrix material. This implies that there is no relative deformation

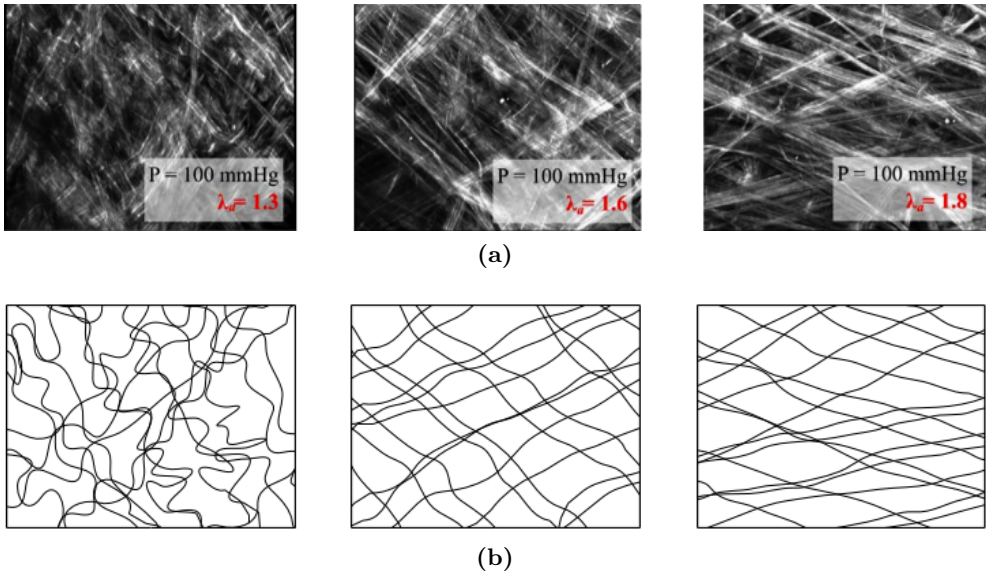

Figure 5.2: (a) Multiphoton microscopy imaging of collagen fibres experiencing reorientation under axial load, adapted from [66] and (b) a schematic illustration of the fibre kinematics.

between these two constituents. However, several authors have investigated non-affine fibre deformation in soft tissue [5, 14, 49, 66, 68]. Billiar and Sacks [5] measured the reorientation of fibres in collagenous tissues. To quantify fibre kinematics, tissue samples from porcine aortic valve leaflets and bovine pericardium specimens were subjected to biaxial loading. In addition to the experimental testing, Billiar and Sacks analytically computed the fibre orientation with the assumption of affine deformation. For both tissues they found that affine predications did not agree with the measured reorientation. The tissues, therefore, exhibited non-affine fibre deformation. Lake et al. [68] examined the assumption that fibres in human tendon tissue experience affine deformation. They performed uniaxial tension tests and observed that the extent of non-affine deformation depended on the orientation of the load. When loaded parallel to the long axis of the tendon, the measured fibre deformation was overall more affine. However, when loaded perpendicular to the long axis, the fibre deformation was more consistent with non-affine deformation. Krasny et al. [66] used multiphoton microscopy to investigate the realignment of collagen fibres in carotid arteries. Two loading cases were considered, namely axial tension and inflation. Realigned was observed when the tissue was tensioned axially, as shown in see Figure 5.2, while little reorientation was observed during inflation of the arteries. However, in both loading scenarios the fibres experienced non-affine deformation.

Microcontinuum modelling has only recently been extended to soft tissues. The lack of microcontinuum modelling in biomechanical problems may be attributed to the large number of material parameters one has to deal with [129]. Sack et al. [108] modelled the behaviour of the myocardium as a Cosserat continuum which allowed non-local material responses to be included in the model. Thurieau et al. [118] investigated the deformation of a healthy and a diseased left ventricle using a microstretch formulation. Heart tissue was modelled as a microstretch medium and the infarcted areas were modelled as a microdilation[1] medium. The left ventricle was represented with a hollow

[1]Microdilatation: constrained version of the microstretch medium that only allows breathing-type motion.

cylinder and the investigation focussed on small strains only. When compared to a healthy heart, Thurieau et al. observed reduced axial deformation for the infarcted regions, which is in line with clinical studies. For academic examples illustrating the use of micromorphic modelling, the reader is referred to [129].

5.3 Kinematics

Figure 5.3 depicts the deformation of a micromorphic continuum which is also viewed as a two-level continuum [71]. In the reference configuration the micromorphic continuum occupies the space $\mathcal{G}_0$ which consists of a macro-space $\mathcal{B}_0$ and a micro-space $\mathcal{S}_0$. Similarly, in the current configuration, the macro-space $\mathcal{B}$ and the micro-space $\mathcal{S}$ compose the micromorphic body $\mathcal{G}$. The macro-space is described by the curvilinear coordinates ϑ^i and the micro-space by the curvilinear coordinates ζ^α. The number of $\alpha = 1, 2, 3...M$ is chosen based on the internal structure of the material [109].

The position of a material point in $\mathcal{G}_0$ is expressed as the sum of the macro-placement $\mathbf{X} \in \mathcal{B}_0$ and the micro-placement $\boldsymbol{\Xi} \in \mathcal{S}_0$. Accordingly, we define the position $\tilde{\mathbf{X}} \in \mathcal{G}_0$ as

$$\tilde{\mathbf{X}} = \mathbf{X}(\vartheta^i) + \boldsymbol{\Xi}(\vartheta^i, \zeta^\alpha) \,. \tag{5.1}$$

Since the micro-placement is relative to the macro-placement it also depends on the macro-coordinates ϑ^i. Similarly, the position in the deformed configuration $\mathcal{G}$ is given by

$$\tilde{\mathbf{x}}(\vartheta^i, \zeta^\alpha, t) = \mathbf{x}(\vartheta^i, t) + \boldsymbol{\xi}(\vartheta^i, \zeta^\alpha, t) \,, \tag{5.2}$$

where $\mathbf{x} \in \mathcal{B}$ and $\boldsymbol{\xi} \in \mathcal{S}$ are the positions in the macro-space and micro-space respectively.

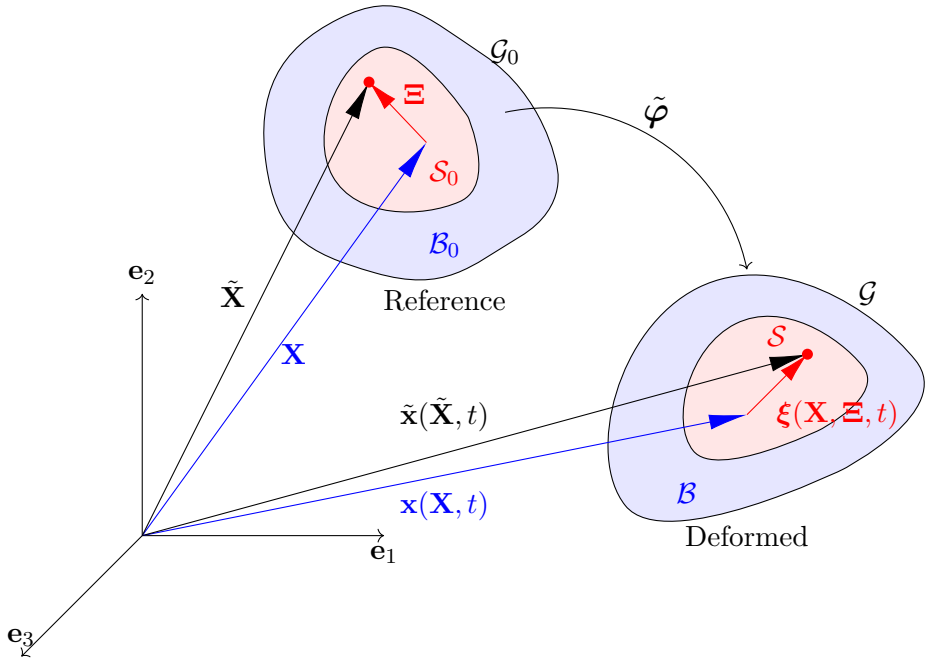

Figure 5.3: Motion of a micromorphic continuum. The continuum is composed of a macro-space and a micro-space. The micro-space represents the deformable particle.

The motion $\tilde{\boldsymbol{\varphi}}$ maps each point in the reference configuration to its current position,

$$\tilde{\boldsymbol{\varphi}} : \mathcal{G}_0 \to \mathcal{G} \,. \tag{5.3}$$

In Section 3.8 we introduced the covariant base vectors, which are tangent to the curvilinear coordinates. The covariant base vectors in the reference configuration are given as

$$\tilde{\mathbf{G}}_i = \frac{\partial \tilde{\mathbf{X}}}{\partial \vartheta^i} \,, \qquad \tilde{\mathbf{I}}_\alpha = \frac{\partial \tilde{\mathbf{X}}}{\partial \zeta^\alpha} \,, \tag{5.4}$$

where $\tilde{\mathbf{G}}_i$ and $\tilde{\mathbf{I}}_\alpha$ are the covariant base vectors of the macro-scale and the micro-scale respectively. Similarly we define the base vectors in the current configuration as

$$\tilde{\mathbf{g}}_i = \frac{\partial \tilde{\mathbf{x}}}{\partial \vartheta^i} \,, \qquad \tilde{\mathbf{i}}_\alpha = \frac{\partial \tilde{\mathbf{x}}}{\partial \zeta^\alpha} \,. \tag{5.5}$$

The form of the micro-space placement has to be chosen a priori. The choice defines the type of microcontinuum, as discussed in Section 5.1. In this work we follow Sansour et al. [109] and introduce scalar fields χ_β to obtain a micro-motion with the following ansatz,

$$\tilde{\mathbf{x}} = \mathbf{x} + \zeta^\alpha (1 + \zeta^\beta \chi_\beta) \mathbf{a}_\alpha \,. \tag{5.6}$$

where the directors $\mathbf{a}_\alpha$ are vector functions that orientate the micro-placement in the current configuration. The introduction of the directors $\mathbf{a}_\alpha$ and scalar fields χ_β add extra degrees of freedom to the problem (on top of the classical displacement degrees of freedom) that need be solved. The macroscopic displacement $\mathbf{u}$ and the micro-deformation $\mathbf{w}_\alpha$ are defined as

$$\mathbf{u} = \mathbf{X} - \mathbf{x} \,, \qquad \mathbf{w}_\alpha = \mathbf{a}_\alpha - \mathbf{A}_\alpha \,. \tag{5.7}$$

where $\mathbf{A}_\alpha$ are the directors in the reference configuration. In this work we define one director for every particle and therefore take α to be one. The director is chosen to align with the longitudinal direction of the cardiac fibre.

5.4 Strain Measures

The generalised deformation gradient is given by

$$\tilde{\mathbf{F}} = \frac{\partial \tilde{\mathbf{x}}}{\partial \tilde{\mathbf{X}}} \,. \tag{5.8}$$

Since $\tilde{\mathbf{x}}$ is a function of the curvilinear coordinates ϑ^i and ζ^α, we can expand the deformation gradient as follows,

$$\begin{aligned} \tilde{\mathbf{F}} &= \frac{\partial \tilde{\mathbf{x}}}{\partial \vartheta^i} \otimes \frac{\partial \vartheta^i}{\partial \tilde{\mathbf{X}}} + \frac{\partial \tilde{\mathbf{x}}}{\partial \zeta} \otimes \frac{\partial \zeta}{\partial \mathbf{X}} \\ &= \frac{\partial \tilde{\mathbf{x}}}{\partial \vartheta^i} \otimes \tilde{\mathbf{G}}^i + \frac{\partial \tilde{\mathbf{x}}}{\partial \zeta} \otimes \tilde{\mathbf{I}} \,, \end{aligned} \tag{5.9}$$

where $\tilde{\mathbf{G}}^i$ and $\tilde{\mathbf{I}}$ are the contravariant base vectors for the macro-space and micro-space respectively.

Furthermore, utilising Equation (5.6) and taking $\alpha = \beta = 1$, we obtain the deformation gradient as

$$\begin{aligned}
\tilde{\mathbf{F}} &= \left(\frac{\partial \mathbf{x}}{\partial \vartheta^i} + \zeta\zeta\frac{\partial \chi}{\partial \vartheta^i}\mathbf{a} + \zeta(1+\zeta\chi)\frac{\partial \mathbf{a}}{\partial \vartheta^i}\right) \otimes \tilde{\mathbf{G}}^i \\
&\quad + \left(\frac{\partial \zeta}{\partial \zeta}\mathbf{a} + \zeta\frac{\partial \mathbf{a}}{\partial \zeta} + \frac{\partial \zeta}{\partial \zeta}\zeta\chi\mathbf{a} + \zeta\frac{\partial \zeta}{\partial \zeta}\chi\mathbf{a} + \zeta\zeta\chi\frac{\partial \mathbf{a}}{\partial \zeta}\right) \otimes \tilde{\mathbf{I}} \\
&= \underbrace{\left(\frac{\partial \mathbf{x}}{\partial \vartheta^i} + \zeta^2\frac{\partial \chi}{\partial \vartheta^i}\mathbf{a} + \zeta(1+\zeta\chi)\frac{\partial \mathbf{a}}{\partial \vartheta^i}\right)}_{\tilde{\mathbf{g}}_i} \otimes \tilde{\mathbf{G}}^i + \underbrace{\left(\mathbf{a} + \zeta\frac{\partial \mathbf{a}}{\partial \zeta} + 2\zeta\chi\mathbf{a} + \zeta^2\chi\frac{\partial \mathbf{a}}{\partial \zeta}\right)}_{\tilde{\mathbf{i}}} \otimes \tilde{\mathbf{I}} \\
&= \tilde{\mathbf{g}}_i \otimes \tilde{\mathbf{G}}^i + \tilde{\mathbf{i}} \otimes \tilde{\mathbf{I}}\,, \qquad (5.10)
\end{aligned}$$

where $\tilde{\mathbf{g}}_i$ and $\tilde{\mathbf{i}}$ are the covariant base vectors for the macro-space and micro-space in the current configuration. The generalised right Cauchy-Green tensor is expressed as

$$\begin{aligned}
\tilde{\mathbf{C}} &= \tilde{\mathbf{F}}^T\tilde{\mathbf{F}} \\
&= (\tilde{\mathbf{G}}^k \otimes \tilde{\mathbf{g}}_k + \tilde{\mathbf{I}} \otimes \tilde{\mathbf{i}})(\tilde{\mathbf{g}}_i \otimes \tilde{\mathbf{G}}^i + \tilde{\mathbf{i}} \otimes \tilde{\mathbf{I}}) \\
&= (\tilde{\mathbf{G}}^k \otimes \tilde{\mathbf{g}}_k)(\tilde{\mathbf{g}}_i \otimes \tilde{\mathbf{G}}^i) + (\tilde{\mathbf{G}}^k \otimes \tilde{\mathbf{g}}_k)(\tilde{\mathbf{i}} \otimes \tilde{\mathbf{I}}) + (\tilde{\mathbf{I}} \otimes \tilde{\mathbf{i}})(\tilde{\mathbf{g}}_i \otimes \tilde{\mathbf{G}}^i) + (\tilde{\mathbf{I}} \otimes \tilde{\mathbf{i}})(\tilde{\mathbf{i}} \otimes \tilde{\mathbf{I}}) \\
&= \underbrace{\tilde{\mathbf{g}}_k \cdot \tilde{\mathbf{g}}_i(\tilde{\mathbf{G}}^k \otimes \tilde{\mathbf{G}}^i)}_{\tilde{\mathbf{C}}^{(0)}} + \underbrace{\tilde{\mathbf{g}}_k \cdot \tilde{\mathbf{i}}(\tilde{\mathbf{G}}^k \otimes \tilde{\mathbf{I}}) + \tilde{\mathbf{i}} \cdot \tilde{\mathbf{g}}_i(\tilde{\mathbf{I}} \otimes \tilde{\mathbf{G}}^i)}_{\tilde{\mathbf{C}}^{(1)}} + \underbrace{\tilde{\mathbf{i}} \cdot \tilde{\mathbf{i}}(\tilde{\mathbf{I}} \otimes \tilde{\mathbf{I}})}_{\tilde{\mathbf{C}}^{(2)}}\,. \qquad (5.11)
\end{aligned}$$

Through inspection of the basis vectors, we see that $\mathbf{C}^{(0)}$ is defined in the macro-space, $\mathbf{C}^{(1)}$ is defined in both the macro-and micro-space while $\mathbf{C}^{(2)}$ is defined in the micro-space only. We define the generalised Green-Lagrange strain tensor $\tilde{\mathbf{E}}$ as

$$\begin{aligned}
\tilde{\mathbf{E}} = \frac{1}{2}(\tilde{\mathbf{C}} - \tilde{\mathbf{C}}_0) &= \frac{1}{2}(\tilde{\mathbf{C}}^{(0)} - \tilde{\mathbf{C}}_0^{(0)}) + \frac{1}{2}(\tilde{\mathbf{C}}^{(1)} - \tilde{\mathbf{C}}_0^{(1)}) + \frac{1}{2}(\tilde{\mathbf{C}}^{(2)} - \tilde{\mathbf{C}}_0^{(2)}) \\
&= \tilde{\mathbf{E}}^{(0)} + \tilde{\mathbf{E}}^{(1)} + \tilde{\mathbf{E}}^{(2)}\,, \qquad (5.12)
\end{aligned}$$

where $\tilde{\mathbf{C}}_0$ is the right Cauchy-Green deformation tensor at time t_0. We can further simplify the above by neglecting χ. In this case we need to solve a total of 6 degrees of freedom: 3 classical displacement (u_1,u_2,u_3) and 3 micro-deformation (w_1,w_2,w_3).

5.5 Weak Formulation

We assume that the generalised second Piola-Kirchhoff stress tensor $\tilde{\mathbf{S}}$ takes the form

$$\tilde{\mathbf{S}} = \tilde{\mathbf{S}}^{(0)}(\tilde{\mathbf{C}}^{(0)}) + \tilde{\mathbf{S}}^{(1)}(\tilde{\mathbf{C}}^{(1)}) + \tilde{\mathbf{S}}^{(2)}(\tilde{\mathbf{C}}^{(2)})\,. \qquad (5.13)$$

Furthermore, we extend the principle of virtual work in Equation (3.79) to include the generalised stress and strain measures,

$$\frac{1}{2}\int_{\mathcal{B}_0}\int_{\mathcal{S}_0} \tilde{\mathbf{S}} : \delta\tilde{\mathbf{C}}\,\mathrm{d}S\mathrm{d}V - W_{ext} = 0\,. \qquad (5.14)$$

The external work W_{ext} is a function of the body and traction forces, as defined in [109],

$$W_{ext} = \int_{\mathcal{B}_0} \mathbf{b} \cdot \delta\mathbf{u} \, \mathrm{d}V + \int_{\mathcal{B}_0} \mathbf{l} \cdot \delta\mathbf{w} \, \mathrm{d}V + \int_{\partial\mathcal{B}_0} \mathbf{t}^{(\mathbf{n})} \cdot \delta\mathbf{u} \, \mathrm{d}A + \int_{\partial\mathcal{B}_0} \mathbf{q}^{(\mathbf{n})} \cdot \delta\mathbf{w} \, \mathrm{d}A \,, \tag{5.15}$$

where $\mathbf{b}$ and $\mathbf{t}$ are the traction and the body forces, and $\mathbf{l}$ and $\mathbf{q}$ are the higher-order body and traction forces. In the above $\delta\mathbf{u}$ is the virtual displacement and $\delta\mathbf{w}$ is the virtual micro-deformation.

By including Equation (5.13), the weak formulation becomes

$$\frac{1}{2}\int_{\mathcal{B}_0}\int_{\mathcal{S}_0} \left(\tilde{\mathbf{S}}^{(0)} : \delta\tilde{\mathbf{C}}^{(0)} + \tilde{\mathbf{S}}^{(1)} : \delta\tilde{\mathbf{C}}^{(1)} + \tilde{\mathbf{S}}^{(2)} : \delta\tilde{\mathbf{C}}^{(2)}\right) \mathrm{d}S\mathrm{d}V - W_{ext} = 0 \,. \tag{5.16}$$

The above expression is non-linear in $\mathbf{u}$ and $\mathbf{w}$ and therefore needs to be linearised. As explained in Chapter 3 the aim is to find the macroscopic displacement $\mathbf{u}$ as well as the micro-deformation $\mathbf{w}$ such that the residual G is minimised,

$$\mathrm{G}(\mathbf{u}, \mathbf{a}) = \frac{1}{2}\int_{\mathcal{B}_0}\int_{\mathcal{S}_0} \left(\tilde{\mathbf{S}}^{(0)} : \delta\tilde{\mathbf{C}}^{(0)} + \tilde{\mathbf{S}}^{(1)} : \delta\tilde{\mathbf{C}}^{(1)} + \tilde{\mathbf{S}}^{(2)} : \delta\tilde{\mathbf{C}}^{(2)}\right) \mathrm{d}S\mathrm{d}V - W_{ext} = 0 \,. \tag{5.17}$$

To linearise the residual we consider a first-order Taylor expansion,

$$\mathrm{G}(\mathbf{u}_{k+1}, \mathbf{a}_{k+1}) = \mathrm{G}(\mathbf{u}_k, \mathbf{a}_k) + \Delta\mathrm{G}_k \,. \tag{5.18}$$

where $\Delta\mathrm{G}_k$ is the variation in the residual. Using Equation (5.17), we obtain the linearised residual as

$$\begin{aligned}
\mathrm{G}(\mathbf{u}_{k+1}, \mathbf{a}_{k+1}) = {} & \frac{1}{2}\int_{\mathcal{B}_0}\int_{\mathcal{S}_0} (\tilde{\mathbf{S}}^{(0)} : \delta\tilde{\mathbf{C}}^{(0)} + \tilde{\mathbf{S}}^{(1)} : \delta\tilde{\mathbf{C}}^{(1)} + \tilde{\mathbf{S}}^{(2)} : \delta\tilde{\mathbf{C}}^{(2)}) \, \mathrm{d}S\mathrm{d}V - W_{ext} \\
& + \frac{1}{2}\int_{\mathcal{B}_0}\int_{\mathcal{S}_0} \left(\frac{\partial\tilde{\mathbf{S}}^{(0)}}{\partial\tilde{\mathbf{C}}^{(0)}}\Delta\tilde{\mathbf{C}}^{(0)} : \delta\tilde{\mathbf{C}}^{(0)} + \frac{\partial\tilde{\mathbf{S}}^{(1)}}{\partial\tilde{\mathbf{C}}^{(1)}}\Delta\tilde{\mathbf{C}}^{(1)} : \delta\tilde{\mathbf{C}}^{(1)} + \frac{\partial\tilde{\mathbf{S}}^{(2)}}{\partial\tilde{\mathbf{C}}^{(2)}}\Delta\tilde{\mathbf{C}}^{(2)} : \delta\tilde{\mathbf{C}}^{(2)}\right) \mathrm{d}S\mathrm{d}V \\
& + \frac{1}{2}\int_{\mathcal{B}_0}\int_{\mathcal{S}_0} \left(\tilde{\mathbf{S}}^{(0)} : \Delta\delta\tilde{\mathbf{C}}^{(0)} + \tilde{\mathbf{S}}^{(1)} : \Delta\delta\tilde{\mathbf{C}}^{(1)} + \tilde{\mathbf{S}}^{(2)} : \Delta\delta\tilde{\mathbf{C}}^{(2)}\right) \mathrm{d}S\mathrm{d}V \,,
\end{aligned} \tag{5.19}$$

where $\Delta\tilde{\mathbf{C}}^{(i)}$ are the variations in the right Cauchy-Green tensor and $\frac{\partial\tilde{\mathbf{S}}^{(i)}}{\partial\tilde{\mathbf{C}}^{(i)}}$ are the elasticity tensors. In the above we have assumed that the external forces are conservative. Instead of having just one elasticity tensor, as in the classical continuum case, we now have three elasticity tensors. The elasticity tensors $\mathbb{C}^{(i)}$ can also be defined in terms of the strain energy function,

$$\mathbb{C}^{(i)} = 2\frac{\partial^2\tilde{\psi}}{\partial\tilde{\mathbf{C}}^{(i)} \otimes \partial\tilde{\mathbf{C}}^{(i)}} \,. \tag{5.20}$$

5.6 Material Model for Passive Cardiac Tissue

In this section we present a micromorphic material model to describe the passive behaviour of cardiac tissue. The proposed strain energy is separated into three components,

$$\tilde{\psi} = \tilde{\psi}^{(0)}(\tilde{\mathbf{E}}^{(0)}) + \tilde{\psi}^{(1)}(I_{8ff}, I_{8fs}, I_{8fn}) + \tilde{\psi}^{(2)}(I_{4f}) \,. \tag{5.21}$$

The first describes the deformation of the bulk material while the second and third components are related to the deformation experienced by the cardiac fibres. The second component describes the relative deformation between the bulk material and the cardiac fibres and the third describes the pure micro-motion of the cardiac fibres. To model the behaviour of the bulk material we utilise the strain energy function by Usyk et al. [122]. Therefore, the surrounding tissue is modelled as an orthotropic material and the contribution to the strain energy is formulated in terms of the macroscopic deformation tensor $\tilde{\mathbf{E}}^{(0)}$. The second and third components of the strain energy function make use of the following invariants,

$$I_{8ff} = \tilde{\mathbf{C}}^{(1)} : \mathbf{V}^f \otimes \mathbf{V}^f \,, \tag{5.22}$$

$$I_{8fs} = \tilde{\mathbf{C}}^{(1)} : \mathbf{V}^f \otimes \mathbf{V}^s \,, \tag{5.23}$$

$$I_{8fn} = \tilde{\mathbf{C}}^{(1)} : \mathbf{V}^f \otimes \mathbf{V}^n \,, \tag{5.24}$$

$$I_{4f} = \tilde{\mathbf{C}}^{(2)} : \mathbf{V}^f \otimes \mathbf{V}^f \,, \tag{5.25}$$

where $\mathbf{V}^f$, $\mathbf{V}^s$ and $\mathbf{V}^n$ are the initial fibre, sheet and normal directions respectively. The invariants I_{8ff}, I_{8fs} and I_{8fn} give information about the relative deformation between the bulk material and the cardiac fibres, while I_{4f} is a measure of the micro-deformation experienced by the cardiac fibres. We utilise Fung-type functions to define the contributions for the relative deformation between the cardiac fibres and the bulk material as well as the micro-deformation of the fibres,

$$\begin{aligned}
\tilde{\psi} = \quad & \underbrace{\frac{A_0}{2B_0}(e^{B_0 Q_m} - 1)}_{\text{bulk deformation}} + \underbrace{A_{comp}\left(\ln\sqrt{\det\tilde{\mathbf{C}}^{(0)}}\right)^2}_{\text{compressibility}} \\
& + \underbrace{\frac{A_{8ff}}{2B_{8ff}}(e^{B_{8ff}Q_{8ff}} - 1) + \frac{A_{8fs}}{2B_{8fs}}(e^{B_{8fs}Q_{8fs}} - 1) + \frac{A_{8fn}}{2B_{8fn}}(e^{B_{8fn}Q_{8fn}} - 1)}_{\text{relative deformation}} \\
& + \underbrace{\frac{A_{4f}}{2B_{4f}}(e^{B_{4f}Q_{4f}} - 1)}_{\text{micro-deformation}} \\
= \quad & \tilde{\psi}^{(0)}_{bulk} + \tilde{\psi}^{(0)}_{comp} + \tilde{\psi}^{(1)} + \tilde{\psi}^{(2)}
\end{aligned} \tag{5.26}$$

with

$$\begin{aligned}
Q_m &= b_{ff}(\tilde{E}^{(0)}_{ff})^2 + b_{ss}(\tilde{E}^{(0)}_{ss})^2 + b_{nn}(\tilde{E}^{(0)}_{nn})^2 + b_{fs}\big((\tilde{E}^{(0)}_{fs})^2 + (\tilde{E}^{(0)}_{sf})^2\big) \\
&\quad + b_{fn}\big((\tilde{E}^{(0)}_{fn})^2 + (\tilde{E}^{(0)}_{nf})^2\big) + b_{sn}\big((\tilde{E}^{(0)}_{sn})^2 + (\tilde{E}^{(0)}_{ns})^2\big) && (5.27)\\
Q_{8ff} &= (I_{8ff} - 2)^2 && (5.28)\\
Q_{8fs} &= I^2_{8fs} && (5.29)\\
Q_{fn} &= I^2_{8fn} && (5.30)\\
Q_{4f} &= (I_{4f} - 1)^2 && (5.31)
\end{aligned}$$

where A_0, B_0 and b_{ij} are material parameters related to the bulk material and A_{8ff}, B_{8ff}, A_{8fn}, B_{8fn}, A_{8fs}, B_{8fs}, A_{4f} and B_{4f} are material parameters related to the cardiac fibres. The scaling parameter A_{comp} is used to ensure the incompressibility condition is satisfied.

With Equation (3.58), we find the generalised Second Piola-Kirchhoff stress tensor to be

$$\begin{aligned}\tilde{\mathbf{S}} = \frac{\partial \tilde{\psi}}{\partial \tilde{\mathbf{E}}} &= 2\frac{\partial \tilde{\psi}}{\partial \tilde{\mathbf{C}}} \\ &= 2\frac{\partial \tilde{\psi}^{(0)}}{\partial \tilde{\mathbf{C}}^{(0)}} + 2\frac{\partial \tilde{\psi}^{(1)}}{\partial \tilde{\mathbf{C}}^{(1)}} + 2\frac{\partial \tilde{\psi}^{(2)}}{\partial \tilde{\mathbf{C}}^{(2)}} \\ &= \tilde{\mathbf{S}}^{(0)} + \tilde{\mathbf{S}}^{(1)} + \tilde{\mathbf{S}}^{(2)} \,. \end{aligned} \tag{5.32}$$

Furthermore, we substitute in the proposed strain energy function to obtain the generalised stress tensors $\tilde{\mathbf{S}}^{(0)}$, $\tilde{\mathbf{S}}^{(1)}$ and $\tilde{\mathbf{S}}^{(2)}$:

$$\begin{aligned}\tilde{\mathbf{S}}^{(0)} = 2\frac{\partial \tilde{\psi}^{(0)}}{\partial \tilde{\mathbf{C}}^{(0)}} &= 2\frac{\partial \tilde{\psi}^{(0)}_{bulk}}{\partial \tilde{\mathbf{C}}^{(0)}} + 2\frac{\partial \tilde{\psi}^{(0)}_{comp}}{\partial \tilde{\mathbf{C}}^{(0)}} \\ &= \frac{\partial \tilde{\psi}^{(0)}_{bulk}}{\partial \tilde{\mathbf{E}}^{(0)}} + 2\frac{\partial \tilde{\psi}^{(0)}_{comp}}{\partial \tilde{\mathbf{C}}^{(0)}} \\ &= \tilde{\mathbf{S}}^{(0)}_{bulk} + \tilde{\mathbf{S}}^{(0)}_{comp} \,. \end{aligned} \tag{5.33}$$

The two stress components in the previous expression are given by

$$\tilde{\mathbf{S}}^{(0)}_{bulk} = \frac{\partial \tilde{\psi}^{(0)}_{bulk}}{\partial \tilde{\mathbf{E}}^{(0)}} = \frac{1}{2} A_0 e^{B_0 Q_m} \frac{\partial Q_m}{\partial \tilde{\mathbf{E}}^{(0)}} \,, \tag{5.34}$$

$$\begin{aligned}\tilde{\mathbf{S}}^{(0)}_{comp} = 2\frac{\partial \tilde{\psi}^{(0)}_{comp}}{\partial \tilde{\mathbf{C}}^{(0)}} &= 2\frac{\partial\, A_{comp}\left(\ln\sqrt{\det\tilde{\mathbf{C}}^{(0)}}\right)^2}{\partial \tilde{\mathbf{C}}^{(0)}} \\ &= 4A_{comp}\ln\sqrt{\det\tilde{\mathbf{C}}^{(0)}}\,\frac{\partial \ln\sqrt{\det\tilde{\mathbf{C}}^{(0)}}}{\partial \tilde{\mathbf{C}}^{(0)}} \\ &= 4A_{comp}\ln\sqrt{\det\tilde{\mathbf{C}}^{(0)}}\,\frac{1}{2}\frac{1}{\sqrt{\det\tilde{\mathbf{C}}^{(0)}}}\frac{1}{\sqrt{\det\tilde{\mathbf{C}}^{(0)}}}\det\tilde{\mathbf{C}}^{(0)}(\tilde{\mathbf{C}}^{(0)})^{-T} \\ &= 2A_{comp}\ln\sqrt{\det\tilde{\mathbf{C}}^{(0)}}(\tilde{\mathbf{C}}^{(0)})^{-T} \,, \end{aligned} \tag{5.35}$$

where we have used the rule $\frac{\partial \det\mathbf{A}}{\partial \mathbf{A}} = (\det\mathbf{A})\mathbf{A}^{-T}$. Similarly we find that

$$\begin{aligned}\tilde{\mathbf{S}}^{(1)} &= 2\frac{\partial \tilde{\psi}^{(1)}}{\partial \tilde{\mathbf{C}}^{(1)}} \\ &= A_{8ff}e^{B_{8ff}Q_{8ff}}\frac{\partial Q_{8ff}}{\partial \tilde{\mathbf{C}}^{(1)}} + A_{8fs}e^{B_{8fs}Q_{8fs}}\frac{\partial Q_{8fs}}{\partial \tilde{\mathbf{C}}^{(1)}} + A_{8fn}e^{B_{8fn}Q_{8fn}}\frac{\partial Q_{8fn}}{\partial \tilde{\mathbf{C}}^{(1)}} \,, \end{aligned} \tag{5.36}$$

and

$$\begin{aligned}\tilde{\mathbf{S}}^{(2)} &= 2\frac{\partial\tilde{\psi}^{(2)}}{\partial\tilde{\mathbf{C}}^{(2)}} \\ &= A_{4f}e^{B_{4f}Q_{4f}}\frac{\partial Q_{4f}}{\partial\tilde{\mathbf{C}}^{(2)}}\,.\end{aligned} \tag{5.37}$$

The complete expression for the generalised stress tensor therefore reads

$$\begin{aligned}\tilde{\mathbf{S}} &= \frac{1}{2}A_0e^{B_0Q_m}\frac{\partial Q_m}{\partial\tilde{\mathbf{E}}^{(0)}} + 2A_{comp}\ln\sqrt{\det\tilde{\mathbf{C}}^{(0)}}(\tilde{\mathbf{C}}^{(0)})^{-1} + \\ &\quad A_{8ff}e^{B_{8ff}Q_{8ff}}\frac{\partial Q_{8ff}}{\partial\tilde{\mathbf{C}}^{(1)}} + A_{8fs}e^{B_{8fs}Q_{8fs}}\frac{\partial Q_{8fs}}{\partial\tilde{\mathbf{C}}^{(1)}} + A_{8fn}e^{B_{8fn}Q_{8fn}}\frac{\partial Q_{8fn}}{\partial\tilde{\mathbf{C}}^{(1)}} + A_{4f}e^{B_{4f}Q_{4f}}\frac{\partial Q_{4f}}{\partial\tilde{\mathbf{C}}^{(2)}}\,.\end{aligned} \tag{5.38}$$

With the introduction of the director $\mathbf{a}$, we have automatically achieved a transversely isotropic material for the fibre component of the strain energy function. To model a fully orthotropic material one would need to include two more directors that align with the sheet and sheet-normal directions.

It is important to identify the elasticity tensors since they provide a relationship between the strain and stress in a material. Using the expression for the stress, the three passive elasticity tensors are found to be

$$\begin{aligned}\mathbb{C}^{(i)} &= \frac{\partial\tilde{\mathbf{S}}^{(i)}}{\partial\tilde{\mathbf{C}}^{(i)}} = 2\frac{\partial^2\tilde{\psi}}{\partial\tilde{\mathbf{C}}^{(i)}\otimes\partial\tilde{\mathbf{C}}^{(i)}} \\ &= \frac{1}{2}\frac{\partial\tilde{\mathbf{S}}^{(i)}}{\partial\tilde{\mathbf{E}}^{(i)}} = \frac{1}{2}\frac{\partial^2\tilde{\psi}}{\partial\tilde{\mathbf{E}}^{(i)}\otimes\partial\tilde{\mathbf{E}}^{(i)}}\end{aligned} \tag{5.39}$$

Therefore,

$$\begin{aligned}\mathbb{C}^{(0)} &= \frac{1}{2}\frac{\partial\tilde{\mathbf{S}}^{(0)}_{bulk}}{\partial\tilde{\mathbf{E}}^{(0)}} + \frac{\partial\tilde{\mathbf{S}}^{(0)}_{comp}}{\partial\tilde{\mathbf{C}}^{(0)}} \\ &= \frac{1}{4}A_0B_0e^{B_0Q_m}\frac{\partial Q_m}{\partial\tilde{\mathbf{E}}^{(0)}}\otimes\frac{\partial Q_m}{\partial\tilde{\mathbf{E}}^{(0)}} + \frac{1}{4}A_0e^{B_0Q_m}\frac{\partial^2Q_m}{\partial\tilde{\mathbf{E}}^{(0)}\otimes\partial\tilde{\mathbf{E}}^{(0)}} + \frac{\partial\tilde{\mathbf{S}}^{(0)}_{comp}}{\partial\tilde{\mathbf{C}}^{(0)}}\,,\end{aligned} \tag{5.40}$$

$$\begin{aligned}\mathbb{C}^{(1)} = \frac{\partial\tilde{\mathbf{S}}^{(1)}}{\partial\tilde{\mathbf{C}}^{(1)}} &= A_{8ff}B_{8ff}e^{B_{8ff}Q_{8ff}}\frac{\partial Q_{8ff}}{\partial\tilde{\mathbf{C}}^{(1)}}\otimes\frac{\partial Q_{8ff}}{\partial\tilde{\mathbf{C}}^{(1)}} + A_{8ff}e^{B_{8ff}Q_{8ff}}\frac{\partial^2Q_{8ff}}{\partial\tilde{\mathbf{C}}^{(1)}\otimes\partial\tilde{\mathbf{C}}^{(1)}} \\ &\quad + A_{8fs}B_{8fs}e^{B_{8fs}Q_{8fs}}\frac{\partial Q_{8fs}}{\partial\tilde{\mathbf{C}}^{(1)}}\otimes\frac{\partial Q_{8fs}}{\partial\tilde{\mathbf{C}}^{(1)}} + A_{8fs}e^{B_{8fs}Q_{8fs}}\frac{\partial^2Q_{8fs}}{\partial\tilde{\mathbf{C}}^{(1)}\otimes\partial\tilde{\mathbf{C}}^{(1)}} \\ &\quad + A_{8fn}B_{8fn}e^{B_{8fn}Q_{8fn}}\frac{\partial Q_{8fn}}{\partial\tilde{\mathbf{C}}^{(1)}}\otimes\frac{\partial Q_{8fn}}{\partial\tilde{\mathbf{C}}^{(1)}} + A_{8fn}e^{B_{8fn}Q_{8fn}}\frac{\partial^2Q_{8fn}}{\partial\tilde{\mathbf{C}}^{(1)}\otimes\partial\tilde{\mathbf{C}}^{(1)}}\,,\end{aligned} \tag{5.41}$$

and

$$\begin{aligned}\mathbb{C}^{(2)} &= \frac{\partial \tilde{\mathbf{S}}^{(1)}}{\partial \tilde{\mathbf{C}}^{(2)}} \\ &= A_{4f} B_{4f} e^{B_{4f} Q_{4f}} \frac{\partial Q_{4f}}{\partial \tilde{\mathbf{C}}^{(2)}} \otimes \frac{\partial Q_{4f}}{\partial \tilde{\mathbf{C}}^{(2)}} + A_{4f} e^{B_{4f} Q_{4f}} \frac{\partial^2 Q_{4f}}{\partial \tilde{\mathbf{C}}^{(2)} \otimes \partial \tilde{\mathbf{C}}^{(2)}} \,. \end{aligned} \tag{5.42}$$

5.7 Summary of Micromorphic Modelling

Most continuum models of the heart are based on classical continuum mechanics. A classical continuum formulation, however, lacks the ability to describe non-affine deformation, i.e. it cannot describe relative deformation of the micro-constituents to the bulk material. In this chapter we proposed the use of a micromorphic formulation to obtain a more complete description of the mechanical behaviour of cardiac tissue.

This chapter introduced the kinematics of a micromorphic continuum as well as the generalised strain measures used to formulate constitutive models. Finally, a material model for passive cardiac tissue was presented. An orthotropic material model is used to describe the behaviour of the surrounding tissue and Fung-type strain energy functions are used to model the relative and micro-deformation of the cardiac muscle fibres.

Chapter 6

Modelling the Active Stresses in the Myocardium

For a complete description of the mechanical behaviour of the heart, we not only need to model the passive response but also the active response of cardiac tissue, i.e. the tension generated when the tissue is electrically stimulated. In this chapter we present a model for the active behaviour of cardiac tissue and discuss how the model is incorporated into the weak formulation presented in Chapter 5.

6.1 Mathematical Model for Active Cardiac Tissue

To include the active behaviour we follow an active-stress approach. That is, the total wall stress $\tilde{\mathbf{S}}_{total}$ is additively decomposed into a passive and an active contribution,

$$\tilde{\mathbf{S}}_{total} = \tilde{\mathbf{S}}_P + \mathbf{S}_A \,, \tag{6.1}$$

where $\mathbf{S}_A$ is the active stress tensor. We assume that the active stress acts on the macro-scale only and therefore exclude scale-dependent effects. The passive stress $\tilde{\mathbf{S}}_P$ is discussed in Chapter 5, see Equation (5.38). To obtain the active stress we utilise the elastance model that was presented in Chapter 4. We repeat the model here for convenience. Furthermore, all the cardiac fibres are assumed to contract simultaneously and the active tension is taken to act only in the fibre direction. As proposed by Guccione et al. [47], the active tension T_A has the following form,

$$T_A = T_{max} \frac{Ca_0^2}{Ca_0^2 + ECa_{50}^2} C_t \,, \tag{6.2}$$

where T_{max} is the tension at the longest sarcomere length and Ca_0 is the peak intracellular calcium concentration. The calcium sensitivity ECa_{50} is defined as

$$ECa_{50} = \frac{(Ca_0)_{max}}{\sqrt{e^{B(l-l_0)} - 1}} \,, \tag{6.3}$$

where B, l_0 and $(Ca_0)_{max}$ are model parameters: B determines the shape of the peak tension-

sarcomere length curve, $(Ca_0)_{max}$ is the maximum peak intracellular calcium concentration and l_0 is the sarcomere length at which no active tension is generated. The internal variable C_t represents the extend of activation [119] and varies between 0 and 1,

$$C_t = \frac{1}{2}(1 - cos\omega)\,. \tag{6.4}$$

The parameter ω has different values during activation and relaxation,

$$\omega = \begin{cases} \pi\frac{t}{t_0} & \text{if } 0 \leq t < t_0 \qquad \text{(activation)} \\ \pi\frac{t-t_0+t_r}{t_r} & \text{if } t_0 \leq t < t_0 + t_r \qquad \text{(relaxation)} \\ 0 & \text{if } t_0 + t_r \leq t \end{cases} \tag{6.5}$$

where t is the time after contraction has started and t_0 is the time needed to reach the peak tension. The duration of relaxation t_r is a function of the sarcomere length l,

$$t_r = ml + b\,, \tag{6.6}$$

where the slope m and time-intercept b are model parameters. Guccione et al. [47] defined the sarcomere length as a function of the stretch along the initial fibre direction, see Equation (4.17). In the present analysis the sarcomere orientation is defined in terms of the director $\mathbf{a}$. As mentioned in Chapter 5, the director lies along the cardiac fibre. As the body is loaded, the orientation of the director changes and therefore also the direction in which contraction takes place. Consider the following,

$$\begin{aligned} (d\mathbf{X})^2 &= d\mathbf{X} \cdot d\mathbf{X} \\ &= \mathbf{F}^{-1}d\mathbf{x} \cdot \mathbf{F}^{-1}d\mathbf{x} \\ &= d\mathbf{x} \cdot (\mathbf{F}\mathbf{F}^T)^{-1}d\mathbf{x}\,, \end{aligned} \tag{6.7}$$

where $d\mathbf{X}$ and $d\mathbf{x}$ are line elements in the reference configuration and current configuration respectively. The deformation gradient $\mathbf{F}$ represents the deformation on the macro-scale. If we let the line elements represent a sarcomere in the reference and the current state, then we can rewrite the above as

$$l_R^2 = l^2\hat{\mathbf{a}} \cdot (\mathbf{F}\mathbf{F}^T)^{-1}\hat{\mathbf{a}} \qquad \text{with} \qquad \hat{\mathbf{a}} = \frac{\mathbf{a}}{\parallel \mathbf{a} \parallel}\,, \tag{6.8}$$

where l_R is the sarcomere length at rest and l is the current sarcomere length. The unit vector $\hat{\mathbf{a}}$ represents the direction or orientation of the director and therefore also the orientation of a sarcomere in the current configuration. Using Equation (6.8) the sarcomere length is given as

$$l = \frac{l_R}{\sqrt{\hat{\mathbf{a}} \cdot (\mathbf{F}\mathbf{F}^T)^{-1}\hat{\mathbf{a}}}} = \frac{l_R}{\sqrt{\mathbf{F}^{-T}\mathbf{F}^{-1} : \hat{\mathbf{a}} \otimes \hat{\mathbf{a}}}}\,. \tag{6.9}$$

Since we assume that the active stress develops in the fibre direction only, the active Cauchy stress tensor is given by

$$\boldsymbol{\sigma}_A = T_A(\hat{\mathbf{a}} \otimes \hat{\mathbf{a}})\,. \tag{6.10}$$

Using Equation (3.39), the active contribution to the second Piola-Kirchhoff stress is given by

$$\mathbf{S}_A = J\mathbf{F}^{-1}T_A(\hat{\mathbf{a}}\otimes\hat{\mathbf{a}})\mathbf{F}^{-T}\,, \tag{6.11}$$

where $\mathbf{F}$ is the deformation gradient associated with the deformation on the macro-scale.

6.2 Weak Formulation

The active-stress approach allows us to simply add the active stress component to the governing equation. With the active stress component, the weak formulation stated in Equation (5.16) now reads

$$\frac{1}{2}\int_{\mathcal{B}_0}\int_{\mathcal{S}_0}\left(\tilde{\mathbf{S}}^{(0)}:\delta\tilde{\mathbf{C}}^{(0)}+\tilde{\mathbf{S}}^{(1)}:\delta\tilde{\mathbf{C}}^{(1)}+\tilde{\mathbf{S}}^{(2)}:\delta\tilde{\mathbf{C}}^{(2)}\right)\mathrm{d}S\mathrm{d}V+\frac{1}{2}\int_{\mathcal{B}_0}\mathbf{S}_A:\delta\mathbf{C}\,\mathrm{d}V-W_{ext}=0\,. \tag{6.12}$$

Since we assume that the active stress acts on the macro-scale only, it is the work conjugate of the classical right Cauchy-Green strain tensor $\mathbf{C}$. As a result, the active stress is constant in the micro-space and there is no need to integrate over the micro-domain.

6.2.1 Linearisation of the Weak Form

As before we consider the residual G and its linearisation, but now we also include the active stress. We extend the linearised residual in Equation (5.19) to include the active stress component,

$$\begin{aligned}
&\mathrm{G}(\mathbf{u}_{k+1},\mathbf{a}_{k+1})=\\
&\frac{1}{2}\int_{\mathcal{B}_0}\int_{\mathcal{S}_0}\left(\tilde{\mathbf{S}}^{(0)}:\delta\tilde{\mathbf{C}}^{(0)}+\tilde{\mathbf{S}}^{(1)}:\delta\tilde{\mathbf{C}}^{(1)}+\tilde{\mathbf{S}}^{(2)}:\delta\tilde{\mathbf{C}}^{(2)}\right)\mathrm{d}S\mathrm{d}V-W_{ext}\\
&+\frac{1}{2}\int_{\mathcal{B}_0}\int_{\mathcal{S}_0}\left(\frac{\partial\tilde{\mathbf{S}}^{(0)}}{\partial\tilde{\mathbf{C}}^{(0)}}\Delta\tilde{\mathbf{C}}^{(0)}:\delta\tilde{\mathbf{C}}^{(0)}++\frac{\partial\tilde{\mathbf{S}}^{(1)}}{\partial\tilde{\mathbf{C}}^{(1)}}\Delta\tilde{\mathbf{C}}^{(1)}:\delta\tilde{\mathbf{C}}^{(1)}+\frac{\partial\tilde{\mathbf{S}}^{(2)}}{\partial\tilde{\mathbf{C}}^{(2)}}\Delta\tilde{\mathbf{C}}^{(2)}:\delta\tilde{\mathbf{C}}^{(2)}\right)\mathrm{d}S\mathrm{d}V\\
&+\frac{1}{2}\int_{\mathcal{B}_0}\int_{\mathcal{S}_0}\left(\tilde{\mathbf{S}}^{(0)}:\Delta\delta\tilde{\mathbf{C}}^{(0)}+\tilde{\mathbf{S}}^{(1)}:\Delta\delta\tilde{\mathbf{C}}^{(1)}+\tilde{\mathbf{S}}^{(2)}:\Delta\delta\tilde{\mathbf{C}}^{(2)}\right)\mathrm{d}S\mathrm{d}V\\
&+\frac{1}{2}\int_{\mathcal{B}_0}\mathbf{S}_A:\delta\mathbf{C}\,\mathrm{d}V+\frac{1}{2}\int_{\mathcal{B}_0}\left(\frac{\partial\mathbf{S}_A}{\partial\mathbf{F}}\Delta\mathbf{F}:\delta\mathbf{C}+\frac{\partial\mathbf{S}_A}{\partial\mathbf{a}}\Delta\mathbf{a}:\delta\mathbf{C}\right)\mathrm{d}V+\frac{1}{2}\int_{\mathcal{B}_0}\mathbf{S}_A:\Delta\delta\mathbf{C}\,\mathrm{d}V=0\,,
\end{aligned} \tag{6.13}$$

where the last three terms are the additions made to the original weak formulation. Because the active stress is given in terms of the deformation gradient and the director, the derivative of the stress is with respect to $\mathbf{F}$ and $\mathbf{a}$. Apart from the three passive elasticity tensors, defined in Equations (5.40) through (5.42), we now have two additional constitutive tensors, $\frac{\partial\mathbf{S}_A}{\partial\mathbf{F}}$ and $\frac{\partial\mathbf{S}_A}{\partial\mathbf{a}}$.

6.2.2 Evaluation of the Active Constitutive Tensors

In this section we derive the fourth and fifth constitutive tensor. Using Equation (6.11) and applying the product rule, we find the fourth constitutive tensor to be,

$$\begin{aligned}
\mathbb{C}^{(3)}=\frac{\partial\mathbf{S}_A}{\partial\mathbf{F}}=\frac{\partial J}{\partial\mathbf{F}}\mathbf{F}^{-1}T_A(\hat{\mathbf{a}}\otimes\hat{\mathbf{a}})\mathbf{F}^{-T}+J\frac{\partial\mathbf{F}^{-1}}{\partial\mathbf{F}}T_A(\hat{\mathbf{a}}\otimes\hat{\mathbf{a}})\mathbf{F}^{-T}+\\
J\mathbf{F}^{-1}\frac{\partial T_A}{\partial\mathbf{F}}(\hat{\mathbf{a}}\otimes\hat{\mathbf{a}})\mathbf{F}^{-T}+J\mathbf{F}^{-1}T_A(\hat{\mathbf{a}}\otimes\hat{\mathbf{a}})\frac{\partial\mathbf{F}^{-T}}{\partial\mathbf{F}}\,.
\end{aligned} \tag{6.14}$$

Similarly the fifth constitutive tensor is given as

$$\mathbb{C}^{(4)} = \frac{\partial \mathbf{S}_A}{\partial \mathbf{a}} = J\mathbf{F}^{-1}T_A\left(\frac{\partial \hat{\mathbf{a}}}{\partial \mathbf{a}} \otimes \hat{\mathbf{a}}\right)\mathbf{F}^{-T} + J\mathbf{F}^{-1}T_A\left(\hat{\mathbf{a}} \otimes \frac{\partial \hat{\mathbf{a}}}{\partial \mathbf{a}}\right)\mathbf{F}^{-T} + J\mathbf{F}^{-1}\frac{\partial T_A}{\partial \mathbf{a}}(\hat{\mathbf{a}} \otimes \hat{\mathbf{a}})\mathbf{F}^{-T} \,. \quad (6.15)$$

Since the active tension T_A is a function of the sarcomere length, its derivative with respect to the deformation gradient is given as follows,

$$\frac{\partial T_A}{\partial \mathbf{F}} = \frac{\partial T_A}{\partial l}\frac{\partial l}{\partial \mathbf{F}} \,. \quad (6.16)$$

Using the definition of the active tension in Equations (6.2) through (6.5), we find that

$$\frac{\partial T_A}{\partial l} = T_{max}\frac{ECa_{50}^2 e^{B(l-l_0)}B}{(e^{B(l-l_0)}-1)(Ca_0^2+ECa_{50}^2)^2}C_t - T_{max}\frac{Ca_0^2}{Ca_0^2+ECa_{50}^2}\frac{1}{2}\sin\omega\frac{\partial \omega}{\partial l} \,. \quad (6.17)$$

The derivative of the sarcomere length with respect to the deformation gradient is easiest to evaluate in index notation. From Equation (6.9), the sarcomere length in index notation is

$$l = \frac{l_R}{\sqrt{F_{sp}^{-1}F_{st}^{-1}\hat{a}_p\hat{a}_t}} \,. \quad (6.18)$$

Therefore,

$$\begin{aligned}
\frac{\partial l}{\partial F_{mn}} &= \frac{\partial}{\partial F_{mn}}\left(\frac{l_R}{\sqrt{F_{sp}^{-1}F_{st}^{-1}\hat{a}_p\hat{a}_t}}\right) \\
&= -\frac{1}{2}\frac{l_R}{(F_{sp}^{-1}F_{st}^{-1}\hat{a}_p\hat{a}_t)^{\frac{3}{2}}}\left(\frac{\partial F_{sp}^{-1}}{\partial F_{mn}}F_{st}^{-1}\hat{a}_p\hat{a}_t + F_{sp}^{-1}\frac{\partial F_{st}^{-1}}{\partial F_{mn}}\hat{a}_p\hat{a}_t\right) \\
&= -\frac{1}{2}\frac{l_R}{(F_{sp}^{-1}F_{st}^{-1}\hat{a}_p\hat{a}_t)^{\frac{3}{2}}}\left(-F_{sm}^{-1}F_{np}^{-1}F_{st}^{-1}\hat{a}_p\hat{a}_t - F_{sp}^{-1}F_{sm}^{-1}F_{nt}^{-1}\hat{a}_p\hat{a}_t\right) \,, \quad (6.19)
\end{aligned}$$

where we have used the rule $\frac{\partial \mathbf{F}^{-1}}{\partial \mathbf{F}} = -\mathbf{F}^{-T}\otimes\mathbf{F}^{-1}$. The derivative of the active tension with respect to the director is given by

$$\frac{\partial T_A}{\partial \mathbf{a}} = \frac{\partial T_A}{\partial l}\frac{\partial l}{\partial \hat{\mathbf{a}}}\frac{\partial \hat{\mathbf{a}}}{\partial \mathbf{a}} \,. \quad (6.20)$$

Again we evaluate the derivative of the sarcomere length with respect to the unit vector $\hat{\mathbf{a}}$ in index notation,

$$\begin{aligned}
\frac{\partial l}{\partial \hat{a}_r} &= \frac{\partial}{\partial \hat{a}_r}\left(\frac{l_R}{\sqrt{F_{sp}^{-1}F_{st}^{-1}\hat{a}_p\hat{a}_t}}\right) \\
&= -\frac{1}{2}\frac{l_R}{(F_{sp}^{-1}F_{st}^{-1}\hat{a}_p\hat{a}_t)^{\frac{3}{2}}}\frac{\partial}{\partial \hat{a}_r}(F_{sp}^{-1}F_{st}^{-1}\hat{a}_p\hat{a}_t) \\
&= -\frac{1}{2}\frac{l_R}{(F_{sp}^{-1}F_{st}^{-1}\hat{a}_p\hat{a}_t)^{\frac{3}{2}}}(F_{sr}^{-1}F_{st}^{-1}\hat{a}_t + F_{sp}^{-1}F_{sr}^{-1}\hat{a}_p) \,. \quad (6.21)
\end{aligned}$$

Lastly, the derivative of the unit vector with respect to the director is given by

$$\begin{aligned}\frac{\partial \hat{\mathbf{a}}}{\partial \mathbf{a}} &= \frac{\partial}{\partial \mathbf{a}}\left(\frac{\mathbf{a}}{\parallel \mathbf{a} \parallel}\right) \\ &= \frac{\partial}{\partial \mathbf{a}}\left(\frac{\mathbf{a}}{\sqrt{\mathbf{a}\cdot\mathbf{a}}}\right). \end{aligned} \tag{6.22}$$

In index form we have

$$\begin{aligned}\frac{\partial \hat{a}_k}{\partial a_s} &= \frac{\partial}{\partial a_s}\left(\frac{a_k}{\sqrt{a_m a_m}}\right) \\ &= \frac{\delta_{ks}\sqrt{a_m a_m} - a_k \frac{1}{2}\frac{1}{\sqrt{a_m a_m}}(\delta_{sm}a_m + a_m\delta_{sm})}{a_m a_m} \\ &= \frac{\delta_{ks}\sqrt{a_m a_m} - a_k \frac{1}{2}\frac{1}{\sqrt{a_m a_m}}(2a_s)}{a_m a_m} \\ &= \frac{\delta_{ks}\sqrt{a_m a_m} - \frac{1}{\sqrt{a_m a_m}}a_k a_s}{a_m a_m}. \end{aligned} \tag{6.23}$$

The expressions in Equations (6.16) through (6.23) are substituted back into Equations (6.14) and (6.15) to obtain the complete expressions for the active constitutive tensors. As discussed in Chapter 3, to obtain the macro-displacement and the micro-deformation we discretise the weak formulation and solve it with an iterative scheme such as the Newton Raphson method.

6.3 Summary

In this chapter we described an active-stress model for the tension generated when cardiac tissue contracts. The proposed model is based on the elastance model presented in [47]. The main difference between the elastance model in [47] and the model presented here is the formulation of the sarcomere length. Here the sarcomere length is expressed in terms of the micro-director and not in terms of the initial fibre direction. We also extended the weak formulation to include the active stress and we derived the active constitutive tensors.

Chapter 7

Simulation Procedure for a Full Heartbeat

In this chapter we first discuss the reconstruction of a patient-specific left ventricle from magnetic resonance images. The remainder of the chapter aims to present a methodology of how each of the four phases in a heartbeat can be simulated with the use of appropriate boundary and loading conditions.

7.1 Three-Dimensional Heart Anatomy and Tissue Structure

This study utilises a patient-specific geometry that was generated by the Computational Continuum Mechanics Group at the University of Cape Town, see [54]. The geometry was reconstructed from magnetic resonance imaging (MRI) scans of the heart that were provided by the Cape University Body Imaging Centre (CUBIC). The use of the scans was approved by the Ethics Committee of the Faculty of Health Sciences, see Appendix B. Below we summarise the general approach that is used to generate a realistic three-dimensional shape of the left ventricle.

MRI scans provide both short- and long-axis views of the heart. The stack of scans used in this study contains short-axis slices spaced 10 mm apart and long-axis slices that are spaced at 8.3 mm intervals. The first short-axis slice is located just below the mitral valve and the last slice is positioned near the apex.

To extract geometric data from the scans, a process known as image segmentation is performed. In this research manual image segmentation of the left ventricle is carried out using Synopsys' Simpleware software together with the image processing tool ScanIP. Because continuum balance laws are often formulated with respect to the reference configuration, it is important to identify a reference (undeformed) state. In our model the reference configuration is taken to be at the start of diastolic filling since early diastole is regarded as being relatively stress-free [86]. The images corresponding to the start of diastolic filling are imported into Simpleware, cropped and segmented as illustrated in Figures 7.1 and 7.2. After completing the segmentation process, a three-dimensional geometry is created based on the segmented regions and smoothing algorithms are applied to the surface. The +NURBS module in Simpleware is utilised to generate a NURBS (non-uniform rational B-spline) surface, which is suitable for finite element analysis.

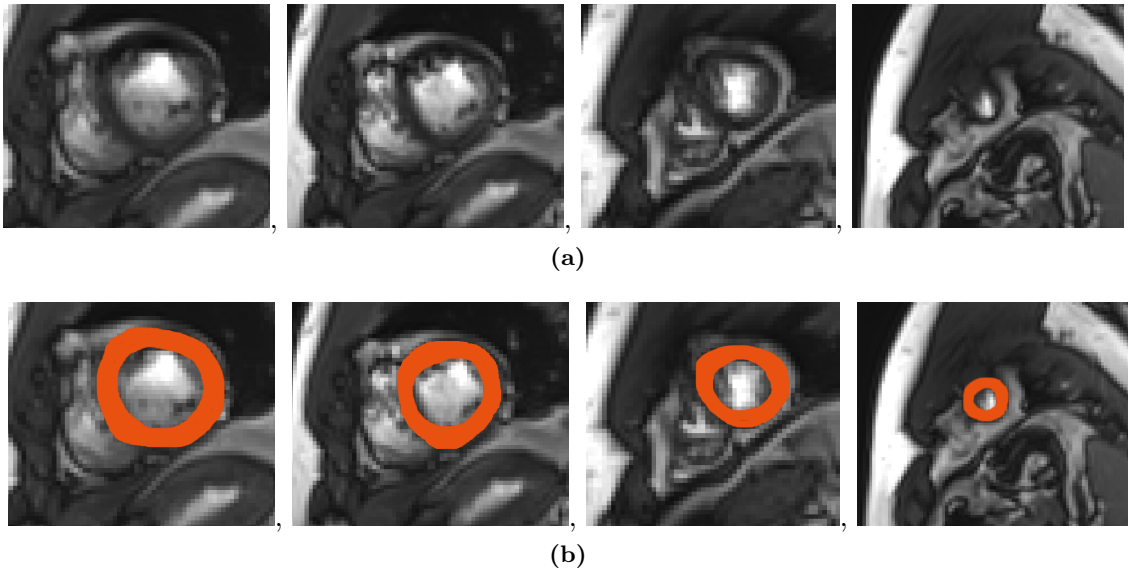

Figure 7.1: Examples of (a) magnetic resonance images from the CUBIC database and (b) segmentation of the left ventricle.

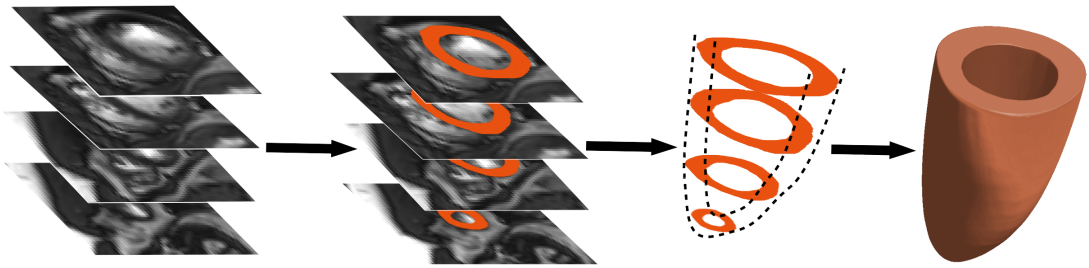

Figure 7.2: Diagram illustrating the process of creating a three-dimensional geometry of the left ventricle. The stack of magnetic resonance images is imported into the image processing software and the anatomical structure of the left ventricle is segmented. A surface is created that fits the segmented regions.

The NURBS surface is imported into the pre- and post-processing software GiD and the geometry is discretised into four-node tetrahedral elements. The material properties, boundary conditions, fibre directions and sarcomere lengths are also assigned in GiD.

Boundary conditions should reflect the physiological conditions in which the heart operates [37]. Because the fibrous structure surrounding the valves is much stiffer than the ventricles, the vertical displacement of the base is taken to be zero. The outer edge of the base is constrained in the x- and y-directions using an elastic line force with a stiffness of 50 kN/mm. This constraint prevents excessive movement of the ventricle in the x-y plane. A pressure load is applied to the endocardial surface of the ventricle to simulate the pressure exerted by the blood. The pressure load is determined for each phase of the cardiac cycle, as discussed in the following sections. The load exerted by the pericardium and surrounding tissue is assumed negligible and therefore the pressure on the epicardial surface is taken to be zero.

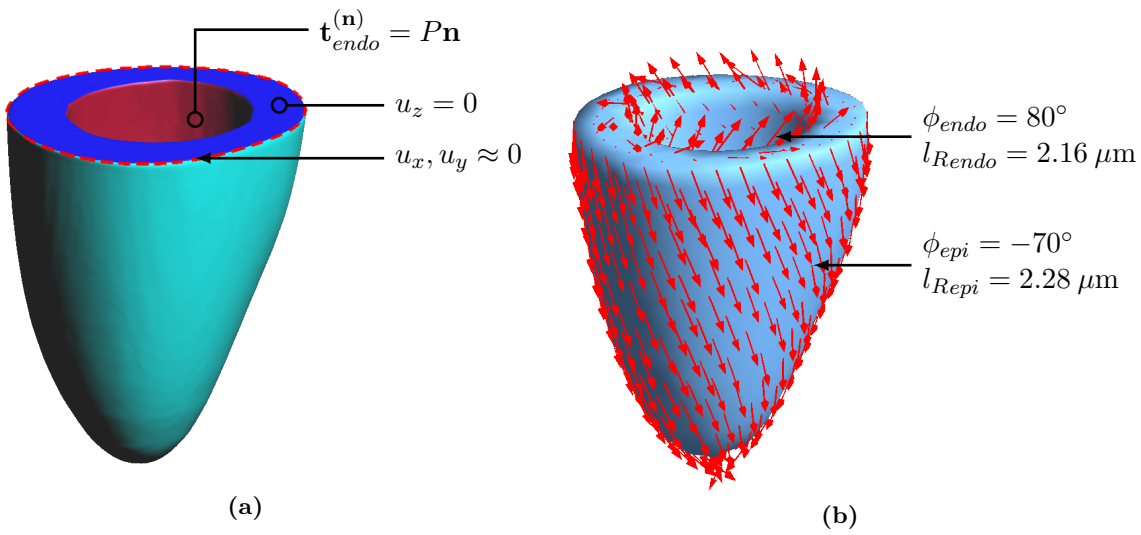

Figure 7.3: Ventricular geometry with (a) the Dirichlet and Neumann boundary conditions and (b) the fibre direction and sarcomere lengths. The vectors indicate the fibre direction in the reference configuration.

The direction of the cardiac fibres in the ventricle is chosen in accordance with [135]. The fibre angles at the epicardial and endocardial surfaces are taken to be -70° and 80° respectively, as depicted in Figure 7.3(b). The transmural variation of the fibre direction is obtained by interpolating the fibre angle through the ventricular wall using the algorithm developed by Wong and Kuhl [135]. Similarly, the resting sarcomere lengths are assigned such that is varies from 2.16 μm at the endocardium to 2.28 μm at the epicardium. Literature reports that the sarcomere length in the unloaded state ranges between 1.9 μm and 2.3 μm [44, 69, 103] and is usually longer near the epicardium [44].

7.2 Modelling the Cardiac Cycle

As discussed in Chapter 2, the cardiac cycle consists of four phases. Accordingly, the simulation is also divided into four different phases. We follow a similar approach to that used by Skatulla and Sansour [111] of which an outlined is given below.

7.2.1 Diastolic Filling

During diastolic filling, blood flows into the left ventricle from its adjoining atrium. As the ventricle fills with blood, there is an increase in its volume as well as the pressure acting on the endocardial surface. The ventricle is in a relaxed state since the cardiac fibres are not electrically activated. As a result, the only stresses present in the ventricular wall are the passive stresses,

$$\tilde{\mathbf{S}}_{total} = \tilde{\mathbf{S}}_P \,. \tag{7.1}$$

The passive stress component $\tilde{\mathbf{S}}_P$ is obtained from the micromorphic model discussed in Chapter 5. A Neumann boundary condition in the form of a pressure load P^{ED} is applied to the endocardial surface of the left ventricle. This pressure load simulates the inflow of blood and is taken to

be 1.5 kPa [65]. Because of the high degree of non-linearity, the external load, in this case the end-diastolic pressure P^{ED}, is applied incrementally,

$$P_n = \zeta_n P^{ED} \qquad \text{with} \qquad 0 \leq \zeta_n \leq 1, \tag{7.2}$$

where ζ_n is the loading factor and n is the current loading step. The current loading factor is determined with a predetermined loading factor increment,

$$\zeta_n = \zeta_{n-1} + \Delta\zeta_n \,, \tag{7.3}$$

where $\Delta\zeta_n$ is the loading factor increment. The displacement field and the micro-deformation are determined for each loading step. Using the displacement field, we also determine the cavity volume for each step. In this way we obtain a set of pressure-volume data points that represents the end-diastolic pressure-volume relationship of the ventricle.

7.2.2 Isovolumetric Contraction

Once the cavity pressure in the ventricle reaches the end-diastolic pressure, the mitral valve closes and no inflow or outflow of blood is permitted. An electrical impulse causes ventricular contraction which in turn results in a significant rise in the cavity pressure. Since blood is a nearly-incompressible fluid, the cavity volume of the ventricle remains relatively constant during this phase. In addition to the passive stress, cardiac fibres now also generate their own tension. Therefore, the total ventricular wall stress is given by

$$\tilde{\mathbf{S}}_{total} = \tilde{\mathbf{S}}_P + \mathbf{S}_A \,, \tag{7.4}$$

where $\mathbf{S}_A$ is the active stress based on the active model discussed in Chapter 6. During isovolumetric contraction the displacement field should be such that the cavity volume of the left ventricle remains constant ($\Delta V \approx 0$). The applied pressure load in each loading step is computed such that the volume constraint is satisfied. Instead of having a predetermined loading factor increment, the increment is unknown and needs to be solved. A displacement control approach is used to determine the loading factor increment and consequently also the pressure load. The displacement control approach and its extension to structures with cavities are discussed in more detail by Skatulla and Sansour [111].

The end of isovolumetric contraction is reached when the left ventricular pressure is equal to the pressure in the aorta which is taken to be 10 kPa [64, 65].

7.2.3 Ejection

Because of the high ventricular pressure at the end of isovolumetric contraction, the aortic valve opens and blood is allowed to flow into the aorta. As blood is ejected, the cavity volume of the ventricle decreases. We use a three-element Windkessel model to obtain the change in volume,

$$\big(1 + \frac{R_a}{R_p}\big)\mathrm{I(t)} + C_a R_a \frac{\mathrm{dI(t)}}{\mathrm{dt}} = \frac{\mathrm{P(t)}}{R_p} + C_a \frac{\mathrm{dP(t)}}{\mathrm{dt}} \,, \tag{7.5}$$

where R_p and R_a are the peripheral resistance of the blood vessels and the resistance of the aorta respectively. The parameter C_a represents the compliance of the elastic arteries.

The initial flow rate is taken to be zero, while the initial pressure is the same as the pressure at the end of isovolumetric contraction. If we assume a small time increment, the three-element Windkessel equation can be written as

$$\big(1+\frac{R_a}{R_p}\big)\mathrm{I_n}+C_aR_a\frac{\mathrm{I_n}-\mathrm{I_{n-1}}}{\Delta\mathrm{t}}=\frac{\mathrm{P_n}}{R_p}+C_a\frac{\mathrm{P_n}-\mathrm{P_{n-1}}}{\Delta\mathrm{t}}\,, \tag{7.6}$$

where n is the current time step. The volume increment in terms of the flow rate is given by

$$\Delta V_n=-\mathrm{I_n}\Delta\mathrm{t}\,. \tag{7.7}$$

The negative sign is to ensure a negative volume change during the ejection phase [97]. Using the above equation and Equation (7.6), the volume increment in terms of the Windkessel parameters is found to be

$$\Delta V_n=-\left(\frac{C_aR_a}{\Delta\mathrm{t}}+\left(1+\frac{R_a}{R_p}\right)\right)^{-1}\left(C_a\frac{\mathrm{P_n}-\mathrm{P_{n-1}}}{\Delta\mathrm{t}}+\frac{\mathrm{P_n}}{R_p}+C_aR_a\frac{\mathrm{I_{n-1}}}{\Delta\mathrm{t}}\right)\Delta\mathrm{t}\,. \tag{7.8}$$

Again the cavity control approach outlined in [111] is used to determine the pressure load on the endocardial surface. The ejection phase ends when the flow rate nears zero.

7.2.4 Isovolumetric Relaxation

After blood ejection, the aortic valve closes and the cavity pressure starts reducing while the cavity volume remains constant. Both passive and active stresses are still present, but the latter gradually decreases to zero. As with isovolumetric contraction, the cavity-volume change ΔV is set to zero. As soon as the ventricular pressure falls below the atrium pressure, the mitral valve opens which signals the end of relaxation. Therefore, the fourth and final phase ends when the ventricular pressure reaches that of the atrium which is taken to be 0.2 kPa.

Chapter 8

Results and Discussions

Previous chapters provided the theoretical background needed to create a computational model of the left ventricle and outlined how the mechanical behaviour of the ventricle may be simulated. Here we discuss the results obtained from the modelling procedure detailed in Chapter 7. We first present the results of a mesh convergence study performed to determine an appropriate mesh density for the finite element model. Next, we summarise the passive, active and Windkessel material parameters determined from shear experiments and pressure-volume data. Finally, we present the simulated ventricular mechanics and we compare the micromorphic formulation with a classical formulation.

8.1 Mesh Convergence Study

A mesh convergence study was conducted to determine an appropriate element size for the finite element model of the left ventricle. The ventricular geometry was first discretised into 486 four-node tetrahedral elements. With each subsequent analysis the mesh was refined to determine the effect of the element size. The most refined mesh consisted of 13 552 tetrahedral elements. Figure 8.1 shows examples of the different mesh densities used in the mesh convergence study.

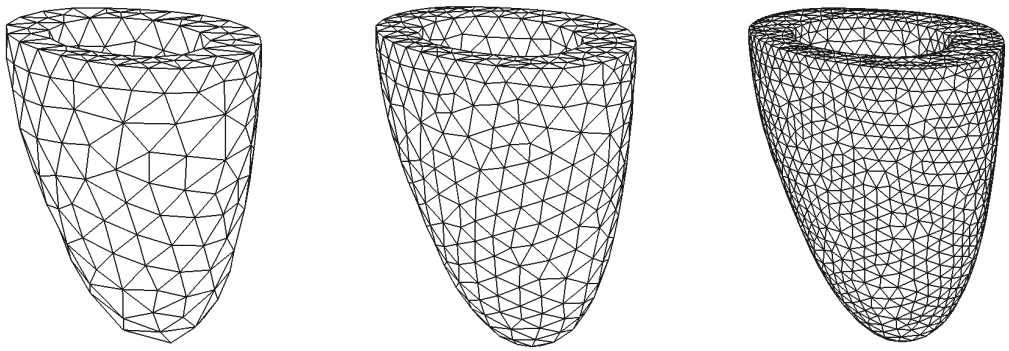

(a) **(b)** **(c)**

Figure 8.1: Examples of finite element geometries consisting of (a) 836 elements, (b) 2017 elements and (c) 7246 elements.

Table 8.1: Values used in the mesh convergence analysis to describe the bulk material behaviour of passive cardiac tissue, obtained from [122].

Parameter	Units	Value
A_0	kPa	0.88
B_0	–	1.0
A_{comp}	kPa	3.0
b_{ff}	–	6.0
b_{ss}	–	7.0
b_{nn}	–	3.0
b_{fs}	–	12.0
b_{fn}	–	3.0
b_{sn}	–	3.0

Table 8.2: Values for the passive material parameters to describe the fibre material in the mesh convergence analysis.

Parameter	Units	Value
A_{8ff}	kPa	0.5
B_{8ff}	–	1.0
A_{8fs}	kPa	0.5
B_{8fs}	–	1.0
A_{8fn}	kPa	0.5
B_{8fn}	–	1.0
A_{4f}	kPa	0.5
B_{4f}	–	1.0

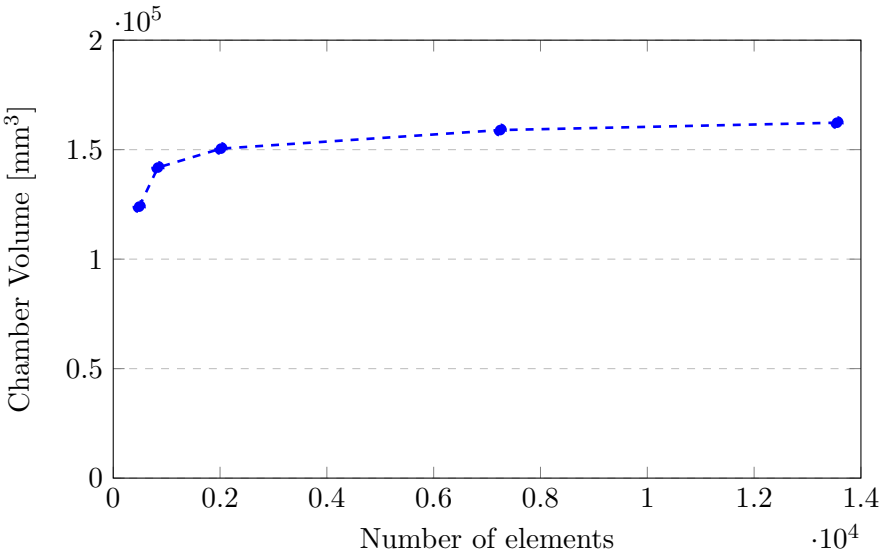

Figure 8.2: Relationship between the element density and the final volume illustrating the convergence of the finite element solution.

In this initial analysis the base of the left ventricle was constrained as discussed in Section 7.1 and a pressure load of 3.0 kPa was applied to the endocardial surface of the ventricle. The passive material parameters that describe the bulk material in Equation (5.38) were chosen based on a study performed by Usyk et al. [122] and are summarised in Table 8.1. Without additional material testing that reports on the non-affine deformation of cardiac tissue, it will not be possible to uniquely identify the material parameters related to the fibre material. For simplicity, the exponential scaling parameters (B_{8ff}, B_{8fs}, B_{8fn} and B_{4f}) were taken to be equal to 1.00, while values for the scaling parameters (A_{8ff}, A_{8fs}, A_{8fn} and A_{4f}) were assumed to be small to limit the reorientation of the fibres.

The results from the mesh convergence study are depicted in Figure 8.2. The figure presents the relationship between the number of tetrahedral elements in the finite element mesh and the final

chamber volume at 3.0 kPa. We see that the difference between successive simulations reduces with each refinement. The curve clearly shows that the simulated volume convergences to a solution as the mesh is refined.

Even though a denser mesh usually provides results that are closer to the actual solution, one also has to take into account the simulation run time when choosing an appropriate mesh. To ensure a balance between computation time and accuracy, a final mesh of 2017 finite elements was chosen for subsequent analyses.

8.2 Material Parameters

Material parameters found in the passive, active and Windkessel models have to be chosen such that the models replicate the observed behaviour of cardiac tissue. To determine suitable values for the parameters, the mathematical models are fit to experimental data. The objective during the calibration process is the minimise the difference between the experimental results and the corresponding simulation results.

8.2.1 Parameter Estimation

To identify material parameters, the Computational Continuum Mechanics (CCM) Research Group implemented a parameter estimation scheme. The scheme is based on the least squares curve fitting problem,

$$\min_{\alpha} J(\boldsymbol{\alpha}) = \sum_{i=1}^{m} (f_i(\boldsymbol{\alpha}, x_i) - y_i(x_i))^2 \,, \tag{8.1}$$

where J is the sum of the squared differences. In Equation (8.1), x_i is the independent variable, y_i is the experimental data point and m is the number of data points. The simulation result f_i depends on the material parameter(s) $\boldsymbol{\alpha}$ and the independent variable x_i. The objective is to minimise the sum of the square of the differences between the experimental data and the computational model. The parameter estimation scheme developed by the research group solves the curve fitting problem using the Levenberg-Marquardt algorithm, which is a combination of the steepest descent method and the Gauss-Newton method. More detail regarding the implementation of this algorithm is found in [30, 97].

8.2.2 Passive Material Parameters

The micromorphic model in Equation (5.38) has 17 material parameters, 9 related to the bulk material and 8 related to the fibre material. All the bulk material parameters, except for the scaling parameter A_0 and the incompressibility parameter A_{comp}, were calibrated with the use of shear test data. The set of passive material parameters was previously determined by the CCM group using the Levenberg-Marquardt algorithm and it is therefore not necessary to recalibrate the passive model. Below we provide a brief outline of how the parameters were obtained, but for a more detailed discussion see [24].

The passive model was calibrated to fit the experimental data obtained by Sommer et al. [113]. Sommer et al. performed tri-axial experiments on cubes of human cardiac tissue. Cubes with dimensions $4 \times 4 \times 4$ mm and sides aligned with the material directions of cardiac tissue were taken from the ventricular wall. The cubes were deformed by constraining one side of the sample and

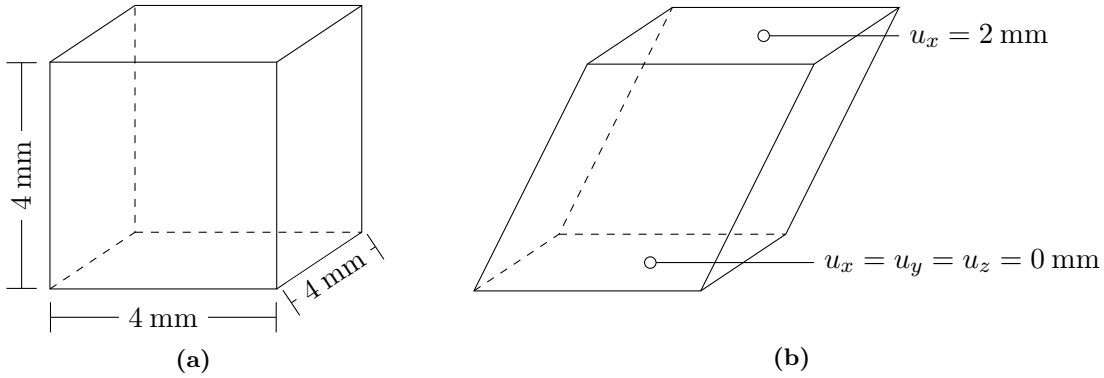

Figure 8.3: Replication of the shear experiments showing (a) the dimensions of the undeformed cube and (b) the boundary conditions used to produce shear deformation.

Table 8.3: Material parameters for the bulk material in the passive model. The parameters were determined by fitting the model to data from shear experiments and the calibration was performed using the Levenberg-Marquardt method, from [24].

Model Parameter		Value after calibration
Bulk	B_0	1.0
	b_{ff}	21.03
	b_{ss}	8.02
	b_{nn}	0.22
	b_{fs}	10.68
	b_{fn}	8.12
	b_{sn}	9.71

translating the opposite surface with a specially designed shear testing device. A shear of 50% was obtained in this way. The shear tests were performed in different orientations to obtain the different shear deformation modes, see Figure 4.2 in Chapter 4.

To determine the material parameters, the shear experiments were reproduced computationally. The simulation consisted of a $4 \times 4 \times 4$ mm cube whose material behaviour was simulated with the micromorphic model discussed in Chapter 5. The degrees of freedom in all three directions on the bottom face were fixed. To ensure pure shear, the opposite face was prevented from moving in the vertical direction while an in-plane displacement of 2 mm was prescribed to achieve a strain of 50%, as shown in Figure 8.3. As noted in Chapter 2, the direction of the cardiac fibres changes gradually across the heart wall. To include this variation in the simulation, the fibre direction was specified such that it varied across the cube. The one side was chosen to have a fibre angle of +30° which varied to -30° at the opposite face [97]. All together 6 computational experiments were required to represent the 6 deformation modes. This was achieved by changing the planes on which the displacement boundary conditions were applied.

The final values for the bulk material parameters are reported in Table 8.3. Only after more detailed experimental testing is performed on cardiac tissue will it be possible to determine the parameters related to the relative motion and micro-motion of the cardiac fibres. In the following sections the fibre material parameters reported in Table 8.2 are used.

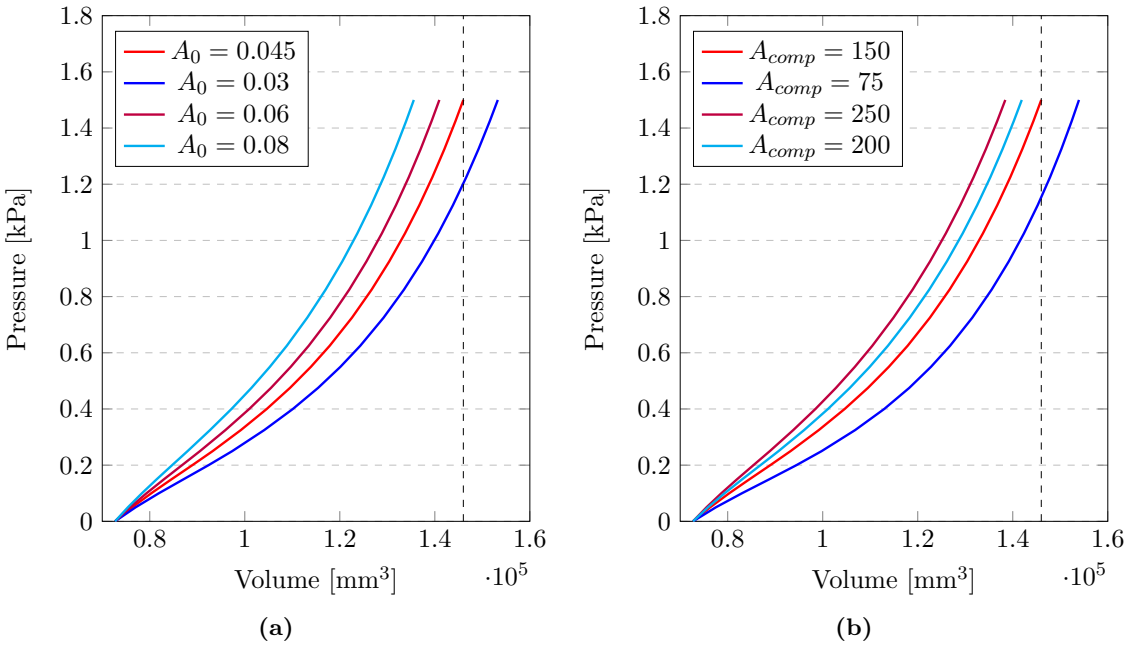

Figure 8.4: The effect on the material response when using different values for (a) the scaling parameter A_0 and (b) the incompressibility parameter A_{comp}. The pressure-volume curves show that increasing these parameters causes the material to behave stiffer. The dashed line indicates the target volume.

We used the end-diastolic pressure-volume relation to obtain suitable values for the incompressibility parameter A_{comp} and the scaling parameter A_0. To determine these values the diastolic filling phase of the cardiac cycle was reproduced as discussed in Section 7.2.1. From magnetic resonance images we know that the end-diastolic volume is equal to 146 ml. The parameters A_{comp} and A_0 were chosen in order to obtain the target volume of 146 ml at an end-diastolic pressure of 1.5 kPa. Figure 8.4 shows the effect of these two parameters on the end-diastolic pressure-volume relationship. The values $A_{comp} = 0.045$ kPa and $A_0 = 150$ kPa were found to be most appropriate.

8.2.3 Active and Windkessel Material Parameters

Calibration of the passive model was followed by the calibration of the systolic parameters. The active and Windkessel model parameters, see Equations (6.2) and (7.5), are presented in Table 8.4. The initial parameters for the active model were chosen in accordance with [47], while the initial Windkessel parameters were based on the study of [64].

The pressure-volume data point at the end of ejection was used to obtain suitable values for the active and Windkessel parameters. The model parameters were chosen such that the simulated volume at the end of ejection matched the clinically measured end-ejection volume. Since the ventricle relaxes at a constant volume, the volume at the start of diastolic filling is the same as the volume at the end of ejection. From magnetic resonance imaging data we know the initial volume and therefore also the end-ejection volume is 73 ml. With the Levenberg-Marquardt algorithm, a set of suitable parameters was determined such that an end-ejection volume of 73 ml was obtained. The final values are summarised in Table 8.4.

Table 8.4: Active and Windkessel material constants determined such that the end-systolic volume was equal to 73 ml.

Model Parameter		Units	Initial value and source	Value after calibration
active	T_{max}	kPa	135.7 [47]	169.98
	C_{a0}	μM	4.35 [47]	4.35
	C_{max}	μM	4.35 [47]	4.35
	b	s	-1.429 [47]	-1.429
	B	μm^{-1}	4.75 [47]	3.8
	l_0	μm	1.58 [47]	1.45
	t_0	s	0.1 [47]	0.22
Windkessel	R_a	kPa·s/mm^3	1.50×10^{-5} [64]	8.75×10^{-5}
	R_p	kPa·s/mm^3	1.20×10^{-6} [64]	9.00×10^{-6}
	C_a	mm^3/kPa	1000 [64]	4500

8.3 Left Ventricular Mechanics

In this section we present the main findings of the computational study of the left ventricle. To verify the micromorphic results, the model is compared to a classical continuum formulation. Cardiac modelling performed in the CCM group led to the development of a fully-calibrated classical continuum model of the heart, see [97]. The classical material model uses the model of Usyk et al. [122], see Equation (4.5), to describe the passive behaviour of cardiac tissue.

8.3.1 Simulated Pressure-Volume Relationship

The pressure-volume curves of the two continuum descriptions are presented in Figure 8.5. The material parameters of the classical model are given in Table 8.5. The orthotropic material parameters b_{ij} were obtained during a previous study, see [97]. As in the micromorphic case, the scaling parameter C and the incompressibility parameter C_{comp} were chosen to obtain an end-diastolic volume of 146 ml. Table 8.6 compares the Windkessel and active model parameters for the classical and micromorphic formulations. These parameters were chosen to ensure the end-ejection volume was equal to 73 ml.

From Figure 8.5 we see that the two formulations produced pressure-volume curves that are similar in shape. Some discrepancy between the curves is expected since the micromorphic formulation includes additional features of the material microstructure. The overall passive behaviour during diastolic filling is very similar for the two formulations. However, comparison of the scaling parameters, C and A_0, reveals that the micromorphic material behaves stiffer than the classical material. A smaller scaling parameter had to be used in the micromorphic case to achieve the same end-diastolic volume of 146 ml. A similar observation was made in a previous study where the Cosserat continuum was used to model cardiac tissue, see [107].

During ejection the cavity pressure increases, reaches a peak value and subsequently decreases. The maximum pressure in the micromorphic case is 19.8 kPa, which is slightly lower than the peak pressure of 20.2 kPa observed in the classical case. The pressure values at the end of ejection are 13.6 kPa and 12.6 kPa for the micromophic model and classical model respectively. Although the

Table 8.5: Material parameters for the classical formulation, from [97].

Parameter	Units	Initial value
C	kPa	0.0733
C_{comp}	kPa	150
b_{ff}	–	23.92
b_{ss}	–	5.89
b_{nn}	–	0.59
b_{fs}	–	12.74
b_{fn}	–	10.19
b_{sn}	–	11.7

Table 8.6: Active and Windkessel model parameters used in the micromorphic and classical model.

Model Parameter		Units	Micromorphic	Classic
active	T_{max}	kPa	169.98	109.5
	C_{a0}	μM	4.35	4.35
	C_{max}	μM	4.35	4.35
	b	s	-1.429	-1.429
	B	μm^{-1}	3.8	1.50
	l_0	μm	1.45	1.58
	t_0	s	0.22	0.22
Windk	R_a	kPa·s/mm^3	8.75×10^{-5}	1.016×10^{-4}
	R_p	kPa·s/mm^3	9.00×10^{-6}	1.00×10^{-5}
	C_a	mm^3/kPa	4500	4500

curves are similar, the classical approach required a much lower T_{max} value to obtain the desired end-systolic volume, see Table 8.6. The discrepancy between these values may be attributed to the inclusion of the micro-space in the micromorphic model and the different methods used to calculate the sarcomere lengths, compare Equations (4.17) and (6.9).

Another issue related to the systolic model parameters worth mentioning is the fact that both the active model and Windkessel model were calibrated with the end-systolic volume. The difficulty is that, because there are so many systolic parameters, there are a large number of potential parameter sets that can be used to obtain the measured end-systolic volume.

It is also worth noting that neither the micromophic nor the classical model was calibrated to patient-specific pressure data, but rather to average values reported in the literature. Because of the invasive nature of the procedure that is required to obtain patient-specific pressure data, it was not performed in this study. Even though the model is not truly patient-specific, it still provides qualitative information that allows us to investigate the mechanics of the ventricle.

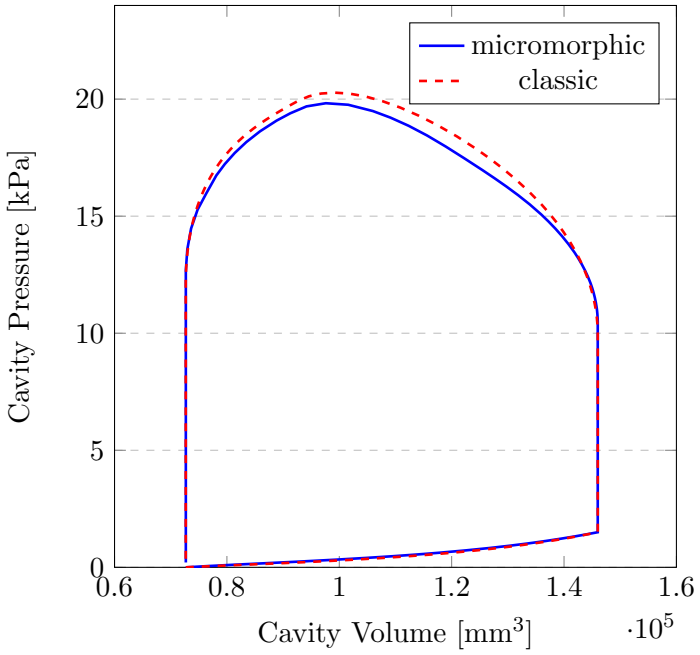

Figure 8.5: Simulated pressure-volume curves using a micromorphic formulation and a classical continuum formulation.

8.3.2 Diastolic Expansion

Figures 8.6 and 8.7 present the development of the effective strain during the cardiac cycle. In both figures the effective strain, defined as

$$\tilde{E}_{eff} = \sqrt{\frac{3}{2}\,\tilde{\mathbf{E}}^{(0)} : \tilde{\mathbf{E}}^{(0)}}\,, \tag{8.2}$$

is superimposed on the deformed geometry of the left ventricle. In Figure 8.6 the strain is plotted on the solid volume, while Figure 8.7 shows the spatial variation of the strain on cross-sectional views of the ventricle. Because the start of diastolic filling is assumed to be the reference configuration, the ventricle has yet to experience any deformation and the spatial distribution of the strain is zero across the ventricle in Figure 8.6(a). Comparison of the deformed geometries in the first two panels of Figure 8.6 shows that the left ventricle expands during diastolic filling. Additionally, the apex moves down causing the ventricle to experience lengthening along its long axis. The cross-sectional views in Figure 8.7 show that the thickness of the ventricular wall changes during a heartbeat. The relative sliding of myocardial sheets allows the changes in the ventricular geometry as well as changes in the wall thickness to take place [72].

8.3.3 Ventricular Twist

During contraction we observe a shortening of the ventricle along its centroidal axis. This results in a more spherical shape at the end of isovolumetric contraction, as seen in Figure 8.6(c). We note that the strain distributions in Figures 8.6(c) and (d) are similar in spite of the significant pressure difference between the two states. The behaviour is expected since biological tissue behaves stiffer at large strains.

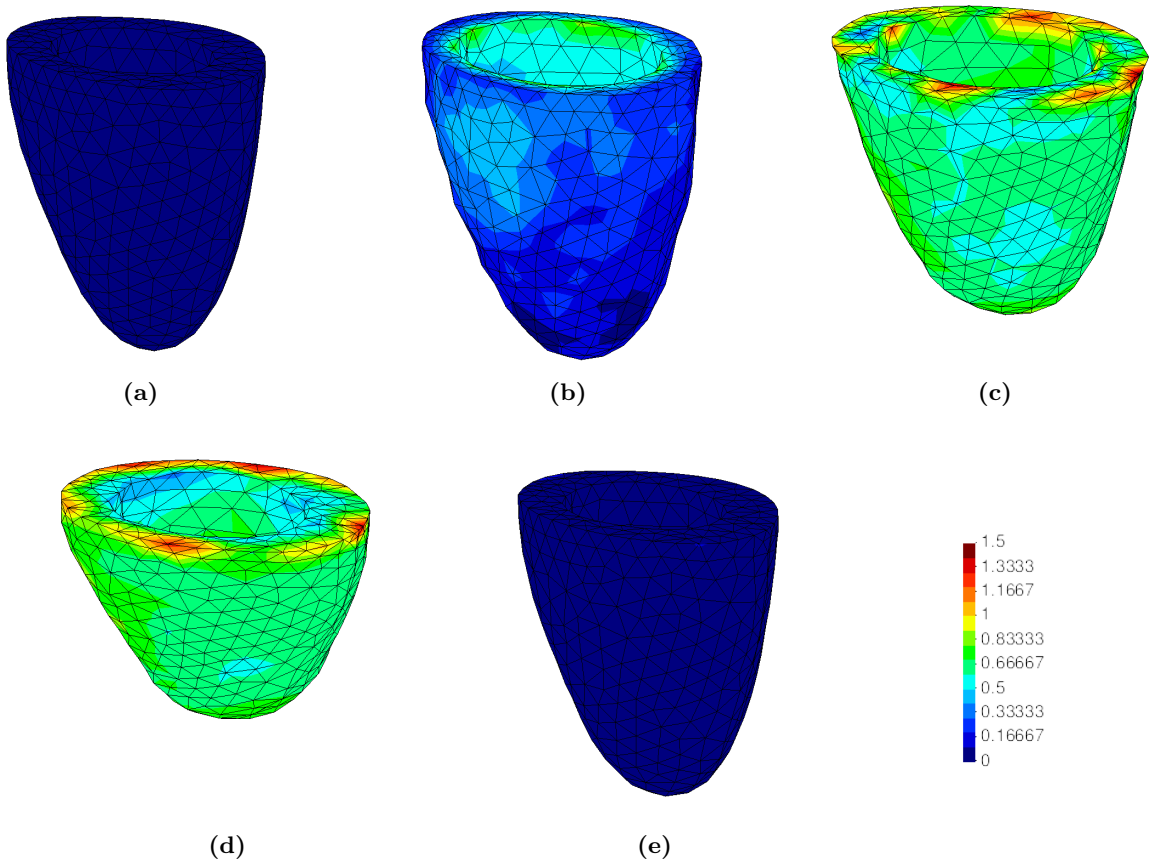

Figure 8.6: The computed effective strain using a micromorphic model, superimposed on the deformed ventricle at the (a) start of diastolic filling, (b) end of diastole, (c) end of isovolumetric contraction, (d) peak pressure and (e) end of isovolumetric relaxation.

As the ventricle contracts, it undergoes a twisting motion in order to increase the blood pressure. Figure 8.8 provides a short-axis view of the ventricle during isovolumetric contraction. The figure depicts the displacement of the ventricle as viewed from the apex and clearly illustrates the overall twisting motion during contraction. The observed twisting is in accordance with clinical findings and occurs as a result of the tissue layout in the myocardium [53, 82]. Without this rotational motion, the ejection fraction would be much less, around 15-20% instead of the actual 50-70% [82].

At the end of isovolumetric relaxation, the ventricle is in a state similar to the initial configuration but with some residual strains[1]. Residual strains are in line with clinical observations since the heart is always in a state of stress. The reason is that pressure exerted by blood during the heart cycle is always larger than zero. In this study we treated the start of diastolic filling as the unloaded state. However, this is somewhat inconsistent with clinical observations. The model may be improved by using the final state in Figure 8.6(e) as the starting point of a new simulation. This will allow for a more accurate simulation, since residual stresses will then automatically be included.

[1]The residual strains are not visible in Figure 8.6(e) because of the chosen colour scale.

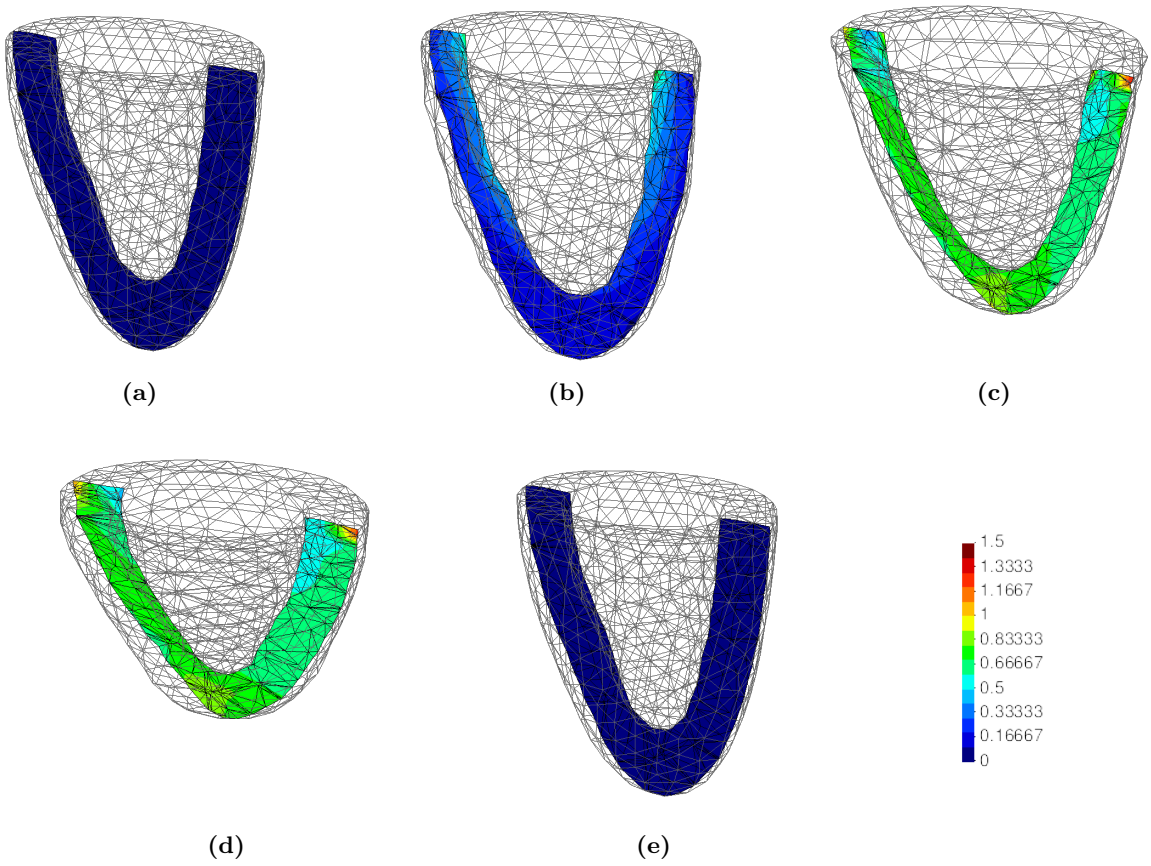

Figure 8.7: The computed strain contours on cross-sectional views of the deformed ventricle at the (a) start of diastolic filling, (b) end of diastole, (c) end of isovolumetric contraction, (d) peak pressure and (e) end of isovolumetric relaxation.

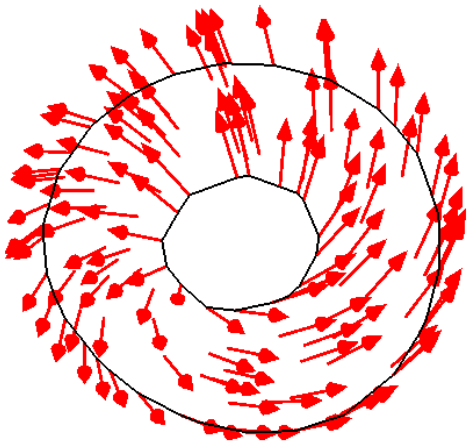

Figure 8.8: The computed displacement during the contraction of the ventricle as viewed from the apex. The displacement is illustrated as vectors to visualise the rotational motion of the ventricle.

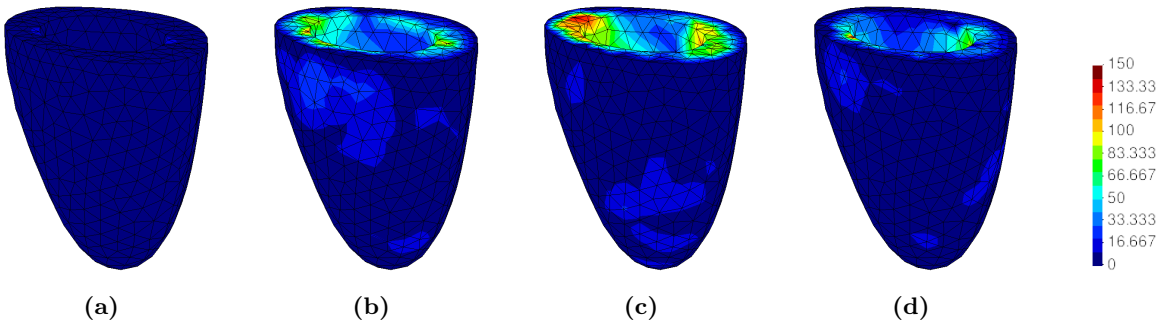

Figure 8.9: The computed effective stress using a micromorphic approach at (a) the end of diastolic filling, (b) end of isovolumetric contraction, (c) mid-ejection and (e) end of ejection.

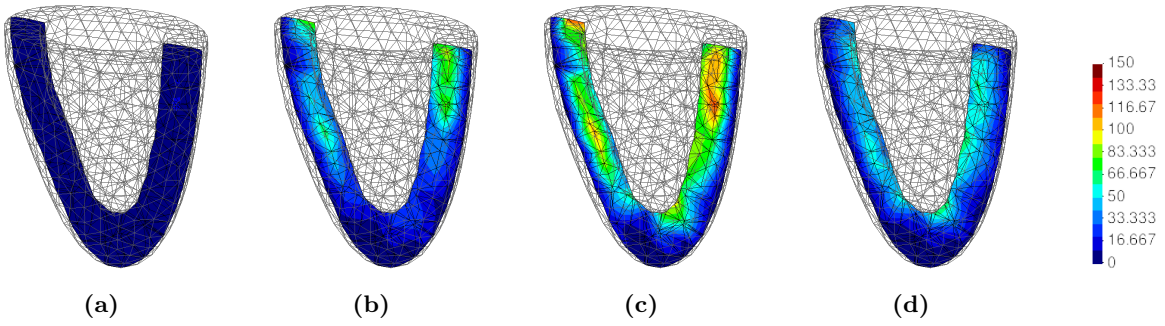

Figure 8.10: The computed effective stress on cross-sectional views of the ventricle at (a) the end of diastolic filling, (b) end of isovolumetric contraction, (c) mid-ejection and (e) end of ejection.

8.3.4 Stresses in the Left Ventricle

Figure 8.9 provides the spatial variation of the effective stress computed at different points in time in the cardiac cycle. The effective stress is given by

$$\tilde{\sigma}_{eff} = \sqrt{\frac{3}{2}\,\tilde{\boldsymbol{\sigma}}^{(0)} : \tilde{\boldsymbol{\sigma}}^{(0)}}\,, \tag{8.3}$$

where $\tilde{\boldsymbol{\sigma}}^{(0)}$ is the Cauchy stress associated with the macro-scale. Presented in Figure 8.10 are the contour plots of the effective stress on cross-sectional views of the left ventricle. As seen in Figure 8.9(a), stress values at the end of diastolic filling are quite low and the distribution is fairly uniform. The reason is that the pressure at the end of filling is still low compared to the pressures throughout the rest of the cardiac cycle. The wall stresses are highest during contraction and ejection, see Figures 8.10(b) and (c) , and the stresses tend to be higher near the endocardium. This corresponds with the study performed by Humphrey and Yin [57], who found that the peak stresses occur in the inner third of the ventricular wall.

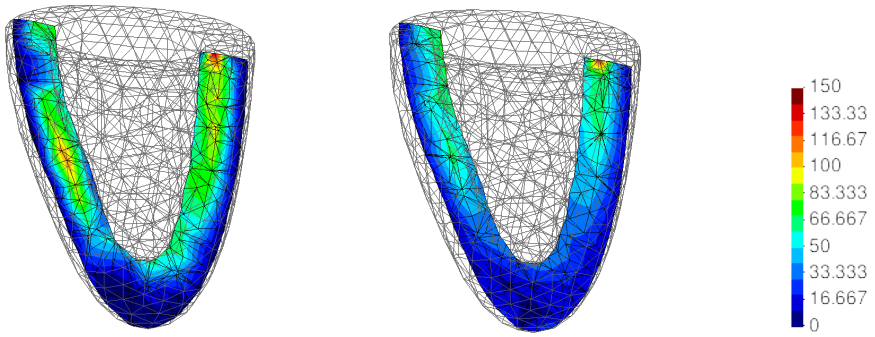

(a) **(b)**

Figure 8.11: The computed active stress distribution using (a) a micromorphic formulation and (b) a classic formulation. The stress is computed at the peak pressures of the two cardiac simulations.

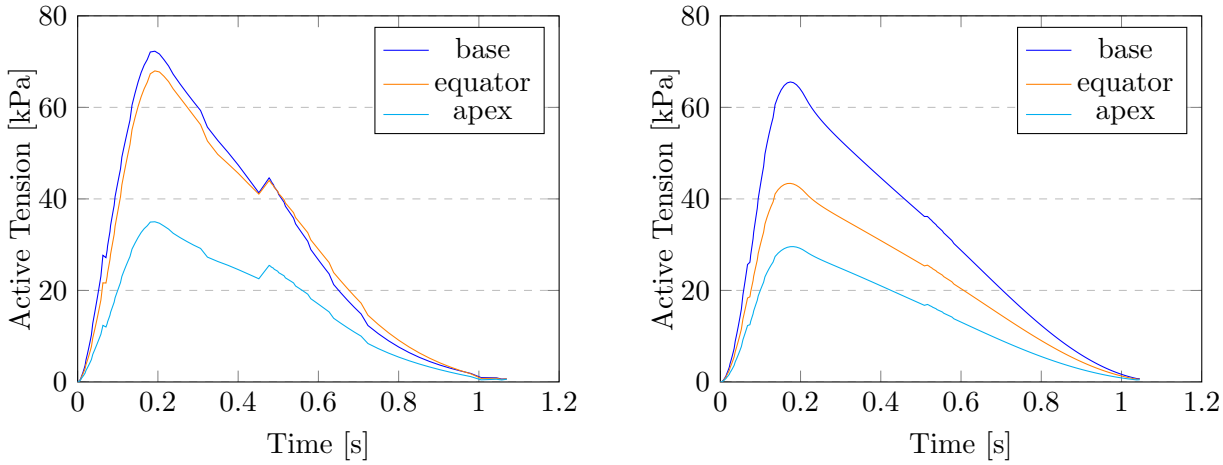

(a) **(b)**

Figure 8.12: The change in the active tension over time near the apex, equatorial region and base of the ventricle for (a) the micromorphic model and (b) the classical continuum model. The beginning of the time line corresponds to the start of systole.

During systole the active tension makes up a significant part of the total stress. Figures 8.11 and 8.12 compare the active tension obtained from the micromorphic model to the active tension computed with a classical continuum formulation. Figure 8.12 presents the evolution of the active tension during the cardiac cycle for three different locations along the ventricle. For both formulations the active tension is highest at the base of the ventricle and lowest near the apex. In general, the active stress is higher in the micromorphic case since, as mentioned in Section 8.3.1, the classical approach uses a much lower value for the model parameter T_{max}.

The sarcomere lengths for the same three locations are plotted in Figure 8.13. Overall, the sarcomeres in the micromorphic continuum are slightly longer. This adds to the discrepancy between the active stress distributions in Figure 8.11.

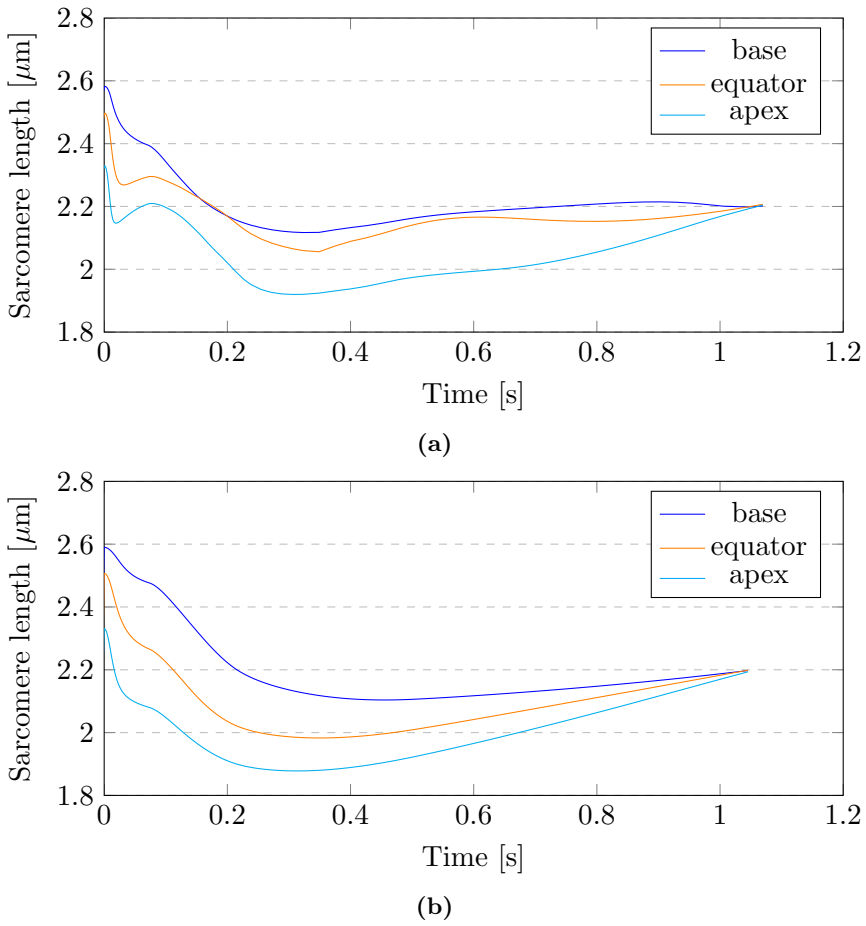

Figure 8.13: The change in sarcomere length over time near the apex, equatorial region and base of the ventricle for (a) micromorphic model and (b) classical continuum model. The beginning of the time line corresponds to the start of systole.

8.4 Summary of Computational Results

In this work we modelled the ventricular myocardium as a micromorphic continuum and the aim of this chapter was to present our results from a computational study of the left ventricle. We also presented a mesh convergence study and discussed how suitable material parameters were obtained for the passive, active and Windkessel models. The micromophic model dealt well with irregular geometries, captured clinically observed behaviour and compared favourably to a classical continuum description.

Chapter 9

Concluding Remarks

In this study we investigated the suitability of a micromorphic formulation to model the behaviour of cardiac tissue. Together with an active-stress model and Windkessel model, the micromorphic model was used to simulate the behaviour of the left ventricle during the cardiac cycle. Below we present the main findings and also provide suggestions for future work.

9.1 Summary

Experimental studies show that cardiac tissue is an anisotropic material that exhibits non-linear viscoelastic behaviour. The tissue forms a helical arrangement in the heart with distinct behaviour in three mutually orthogonal directions: the fibre, sheet and sheet-normal directions. Classical continuum mechanics is one of the most popular tools to describe and predict the mechanical behaviour of the intact heart and several material models from the literature were presented in Chapter 4. Recent material models simulate passive cardiac tissue as either a transversely isotropic or an orthotropic material.

Literature indicates that some biological tissues exhibit non-affine deformation, that is, tissue fibres deform relative to the surrounding matrix material. One disadvantage of classical continuum models is that they lack the ability to describe this type of relative deformation. To overcome some of the limitations associated with classical continuum modelling, we chose a micromorphic continuum description for cardiac tissue. In the formulation presented, micro-directors were introduced to represent the deformation experienced by the cardiac muscle fibres. The constitutive model used to approximate the passive response of cardiac tissue was separated into three components. The first described the behaviour of the bulk material and was modelled with the orthotropic model by Usyk et al. [122]. The second characterised the relative deformation between the cardiac fibres and the bulk material and third the micro-deformation of the fibres.

As a working micromorphic model already existed, this study focussed on developing and implementing a model to describe the active stresses in cardiac tissue. For this, the elastance model proposed by Guccione et al. [47] was modified and coupled with the existing micromorphic model. All implementations were performed in the in-house finite element software, SESKA.

We utilised a patient-specific geometry of a human left ventricle segmented from magnetic resonance imaging scans. The pre- and post-processor GiD was used to discretise the geometry and

also to apply boundary and loading conditions. The boundary and loading conditions were chosen so as to replicate the different phases of the cardiac cycle, as presented in Chapter 7.

Apart from the micromorphic continuum acting slightly stiffer than the classical continuum, both models produced similar behaviour for the passive myocardium. During systole the difference between the two formulations was more noticeable. One reason is the approach used to compute the active tension. The micromorphic formulation and classical formulation use different methods to determine the sarcomere length, and hence also the active tension. Nevertheless, both approaches produced ventricular motions that were consistent with clinical observations, such as twisting and longitudinal motion.

One disadvantage of a micromorphic formulation is the running time. Since a larger number of degrees of freedom need to be solved, the micromorphic simulation required more computation time in comparison with the classical simulation. In this sense, if the simulation time is of great importance the classical continuum model is the more feasible approach. Additionally, the micromorphic model was very sensitive to changes in the material parameters during systole.

9.2 Recommendations and Future Work

9.2.1 Geometry

To model the full heart cycle, we assumed that the left ventricle is unloaded at the beginning of diastolic filling, i.e. the start of diastole was chosen as the reference configuration. However, the working heart is never truly unloaded as it is always subjected to some form of passive or active load. One possibility for future simulations is to explore the inclusion of residual stresses in the continuum model.

With the current model, we investigated the mechanics of the left ventricle without taking into account the right ventricle or the two atria. The addition of these chambers is expected to add to the overall stiffness of the body and will therefore alter the ventricular mechanics. Further studies are required whereby the other heart chambers are included in the cardiac model.

The pericardium was also excluded from the model. Its effect can be modelled with spring elements, as was done in [41], or the pericardium can also be included as a separate continuum body. The latter will require reconstructing the geometry of the pericardium and modelling its interaction with the ventricle.

The mesh convergence study in Chapter 8 indicates that a finer mesh than that used in this study would be more appropriate. Due to the computation time of the simulations, a relatively coarse mesh was chosen for the analysis. The calibration process in particular required a significant amount of runtime since multiple cardiac simulations had to be performed. In future work, a finer mesh should be used together with high-performance computers to improve the processing speed.

9.2.2 Passive Model

Micromorphic modelling of cardiac tissue is unfortunately limited by the lack of experimental data. Further experimental studies that elucidate the deformations experienced by the heart fibres are required. More specifically, to improve the calibration of the micromorphic model, we need experimental data that quantify the non-affine deformation of cardiac tissue during a heartbeat.

In the micromorphic formulation, one director, aligned with the fibre direction, was defined for each point particle. In this way, the fibre component of the strain energy function was modelled as a transversely isotropic material. The passive model may be further improved by introducing two additional directions to describe the sheet and sheet-normal directions. This will allow us to achieve a fully orthotropic material.

In Chapter 8 we focused on the macroscopic behaviour during a full heartbeat. We did not directly address one of the main aims of a micromorphic continuum description, which is to model multi-scale behaviour of materials. The effect of a micromorphic formulation on the microstructure might be better elucidated if one considers isolated cardiac tissue segments. This will allow investigators to observe the size effects of cardiac tissue.

9.2.3 Active Model

The elastance model remains a fairly simple model. To model a more complete response, it is recommended that an active model that incorporates crossbridge interactions be used. Furthermore, experimental studies indicate that active tension is present in the sheet directions. In our analysis the active tension was assumed to act only in the longitudinal direction of the fibre. Therefore, to enhance the active-stress model, the active stress tensor should include components in the sheet direction, see Equation (4.19).

In our model, we assumed that all the cardiac fibres contract simultaneously. This assumption is likely to reduce the twisting and shape change of the ventricle [125]. One way to account for the difference in activation time is to use an equation that describes the spatial distribution of the electrical impulse. In this way, the fibres near the base will contract before the fibres located in the apical region. Furthermore, the elastance model was calibrated to fit the pressure-volume curve of the left ventricle. Ideally, the active parameters should be based on active-tension experiments performed on isolated cardiac tissue specimens.

9.2.4 Heart Diseases

Generalised continuum approaches perform well when dealing with localised deformations. Research conducted by the CCM Group and their medical collaborators is currently under way to better understand rheumatic heart diseases. One goal is to use the micromorphic model to study the behaviour of diseased hearts. For instance, a micromorphic formulation will allow us to study stress and strain localisations that occur as a result of heart diseases. The model presented in this thesis is of a healthy heart and is therefore useful as a benchmark model. In this way, a diseased heart model can be compared to our healthy heart model to investigate the effect of the disease.

Lastly, tissue continuously adapts because of changes to the environment in which it operates. Another application of the micromorphic model is simulating the process of tissue remodelling and investigating how the microstructure changes over time.

References

[1] Alexander, A. L., Lee, J. E., Lazar, M., and Field, A. S. (2007). Diffusion tensor imaging of the brain. *Neurotherapeutics*, 4(3):316–329.

[2] Ambrosi, D. and Pezzuto, S. (2012). Active stress vs. active strain in mechanobiology: Constitutive issues. *Journal of Elasticity*, 107(2):199–212.

[3] Arts, T., Reneman, R. S., and Veenstra, P. C. (1979). A model of the mechanics of the left ventricle. *Annals of Biomedical Engineering*, 7(3):299–318.

[4] Bayer, J. D., Blake, R. C., Plank, G., and Trayanova, N. A. (2012). A novel rule-based algorithm for assigning myocardial fiber orientation to computational heart models. *Annals of Biomedical Engineering*, 40(10):2243–2254.

[5] Billiar, K. L. and Sacks, M. S. (1997). A method to quantify the fiber kinematics of planar tissues under biaxial stretch. *Journal of Biomechanics*, 30(7):753–756.

[6] Bovendeerd, P. H. M., Arts, T., Huyghe, J. M., Van Campen, D., and Reneman, R. (1992). Dependence of local left ventricular wall mechanics on myocardial fiber orientation: A model study. *Journal of Biomechanics*, 25(10):1129–1140.

[7] Brodland, G. W. (2015). How computational models can help unlock biological systems. *Seminars in Cell and Developmental Biology*, 47-48:62–73.

[8] Buchalter, M. B., Weiss, J. L., Rogers, W. J., Zerhouni, E. A., Weisfeldt, M. L., Beyar, R., and Shapiro, E. P. (1990). Noninvasive quantification of left ventricular rotational deformation in normal humans using magnetic resonance imaging myocardial tagging. *Circulation*, 81(4):1236–1244.

[9] Buckberg, G., Hoffmanand, J. I., Mahajan, A., Saleh, S., and Coghlan, C. (2009). Cardiac mechanics revisited the relationship of cardiac architecture to ventricular function. *Circulation*, 118:2571–2587.

[10] Buckberg, G. D., Clemente, C., Cox, J. L., Coghlan, H. C., Castella, M., Torrent-Guasp, F., and Gharib, M. (2001). The structure and function of the helical heart and its buttress wrapping. iv. concepts of dynamic function from the normal macroscopic helical structure. *Seminars in Thoracic and Cardiovascular Surgery*, 13(4):342–357.

[11] Buechner, P. M. and Lakes, R. S. (2003). Size effects in the elasticity and viscoelasticity of bone. *Biomechanics and Modeling in Mechanobiology*, 1(4):295–301.

[12] Campbell, K. B., Lee, L. C., Frasch, H. F., and Noordergraaf, A. (1989). Pulse reflection sites and effective length of the arterial system. *The American Journal of Physiology*, 256:H1684–H1689.

[13] Carter, T. and Ellis, K. (2005). Right ventricular infarction. *Critical Care Nurse*, 25(2):52–62.

[14] Chandran, P. L. and Barocas, V. H. (2006). Affine versus non-affine fibril kinematics in collagen networks: Theoretical studies of network behavior. *Journal of Biomechanical Engineering*, 128(2):259–270.

[15] Clerc, L. (1976). Directional differences of impulse spread in trabecular muscle from mammalian heart. *The Journal of Physiology*, 255(2):335–346.

[16] Cleutjens, J. P. M. (1996). The role of matrix metalloproteinases in heart disease. *Cardiovascular Research*, 32:816–821.

[17] Codreanu, I., Robson, M. D., Golding, S. J., Jung, B. A., Clarke, K., and Holloway, C. J. (2010). Longitudinally and circumferentially directed movements of the left ventricle studied by cardiovascular magnetic resonance phase contrast velocity mapping. *Journal of Cardiovascular Magnetic Resonance*, 12(48).

[18] Cosserat, E. and Cosserat, F. (1909). *Théorie des corps déformables*. Hermann, Paris.

[19] Costa, K. D., Holmes, J. W., and Mcculloch, A. D. (2001). Modelling cardiac mechanical properties in three dimensions. *Philosophical Transactions of the Royal Society of London A: Mathematical, Physical and Engineering Sciences*, 359(1783):1233–1250.

[20] Creswell, L. L., Wyers, S. G., Pirolo, J. S., Perman, W. H., Vannier, M. W., and Pasque, M. K. (1992). Mathematical modeling of the heart using magnetic resonance imaging. *IEEE Transactions on Medical Imaging*, 11(4):581–589.

[21] Demer, L. L. and Yin, F. C. (1983). Passive biaxial mechanical properties of isolated canine myocardium. *Journal of Physiology*, 339:615–630.

[22] Demiray, H. (1976). Stresses in ventricular wall. *Journal of Applied Mechanics*, 43.

[23] Dokos, S., Smaill, B. H., Young, A. A., and LeGrice, I. J. (2002). Shear properties of passive ventricular myocardium. *American Journal of Physiology-Heart and Circulatory Physiology*, 283(6):H2650–H2659.

[24] Dollery, D., Skatulla, S., and Ntusi, N. (2018). A micromorphic approach modelling the anisotropic material behaviour of the human heart. *South African Conference on Computational and Applied Mechanics*, 11:47–58.

[25] Eghbali, M. and Weber, K. T. (1990). Collagen and the myocardium: fibrillar structure, biosynthesis and degradation in relation to hypertrophy and its regression. *Molecular and Cellular Biochemistry*, 96(1):1–14.

[26] Eringen, A. C. (1967). *Theory of Micropolar Elasticity*. Springer, New York.

[27] Eringen, A. C. (1999). *Microcontinuum Field Theories: I. Foundations and Solids*. Springer, New York.

[28] Eringen, A. C. (2004). Electromagnetic theory of microstretch elasticity and bone modeling. *International Journal of Engineering Science*, 42(3):231–242.

[29] Eringen, A. C. and Suhubi, E. S. (1964). Nonlinear theory of simple microelastic solids. *International Journal of Engineering Science*, 2(2):389–404.

[30] Essack, M. A. (2014). Material parameter identification for modelling the left ventricle in the healthy state. Master's thesis, University of Cape Town.

[31] Finsberg, H., Xi, C., Tan, J. L., Zhong, L., Genet, M., Sundnes, J., Lee, L. C., and Wall, S. T. (2018). Efficient estimation of personalized biventricular mechanical function employing gradient-based optimization. *International Journal for Numerical Methods in Biomedical Engineering*, 34(7).

[32] Forest, S. (2013). Micromorphic media. In *Generalized Continua from the Theory to Engineering Applications*, pages 249–300. Springer, Vienna.

[33] Fox, S. I. (1996). *Human physiology*. Wm. C. Brown, London, 5 edition.

[34] Frank, O. (1899). *Die Grundform des arteriellen pulses: Mathematische Analyse. Erste Abhandlung*. Zeitschrift für Biologie. Offprint.

[35] Froeling, M., Strijkers, G. J., Nederveen, A. J., Chamuleau, S. A., and Luijten, P. R. (2014). Diffusion tensor mri of the heart – in vivo imaging of myocardial fiber architecture. *Current Cardiovascular Imaging Reports*, 7.

[36] Fung, Y. C. (1970). Mathematical representation of the mechanical properties of the heart muscle. *Journal of Biomechanics*, 3(4):381–404.

[37] Fung, Y. C. (1993). *Biomechanics: Mechanical Properties of Living Tissues*. Springer, New York.

[38] Fung, Y. C., Fronek, K., and Patitucci, P. (1979). Pseudoelasticity of arteries and the choice of its mathematical expression. *American Journal of Physiology-Heart and Circulatory Physiology*, 237(5):H620–H631.

[39] Geerts, L., Bovendeerd, P., Nicolay, K., and Arts, T. (2002). Characterization of the normal cardiac myofiber field in goat measured with mr-diffusion tensor imaging. *American Journal of Physiology. Heart and Circulatory physiology*, 283:H139–H145.

[40] Gilbert, S. H., Benson, A. P., Li, P., and Holden, A. V. (2007). Regional localisation of left ventricular sheet structure: integration with current models of cardiac fibre, sheet and band structure. *European Journal of Cardiothoracic Surgery*, 32(2):231–249.

[41] Göktepe, S., Acharya, S. N. S., Wong, J., and Kuhl, E. (2011). Computational modeling of passive myocardium. *International Journal for Numerical Methods in Biomedical Engineering*, 27:1–12.

[42] Göktepe, S., Menzel, A., and Kuhl, E. (2014). The generalized hill model: A kinematic approach towards active muscle contraction. *Journal of the Mechanics and Physics of Solids*, 72:20 – 39.

[43] Gray, R. A. and Pathmanathan, P. (2018). Patient-specific cardiovascular computational modeling: Diversity of personalization and challenges. *Journal of Cardiovascular Translational Research*, 11(2):80–88.

[44] Grimm, A. F., Lin, H. L., and Grimm, B. R. (1980). Left ventricular free wall and intraventricular pressure-sarcomere length distributions. *American Journal of Physiology-Heart and Circulatory Physiology*, 239(1):H101–H107.

[45] Guccione, J. and McCulloch, A. D. (1993). Mechanics of active contraction in cardiac muscle: Part i—constitutive relations for fiber stress that describe deactivation. *Journal of Biomechanical Engineering*, 115:72–81.

[46] Guccione, J., McCulloch, A. D., and Waldman, L. (1991). Passive material properties of intact ventricular myocardium determined from a cylindrical model. *Journal of Biomechanical Engineering*, 113:42–55.

[47] Guccione, J., Waldman, L., and McCulloch, A. D. (1993). Mechanics of active contraction in cardiac muscle: Part ii—cylindrical models of the systolic left ventricle. *Journal of Biomechanical Engineering*, 115:82–90.

[48] Hall, J. E. (2016). *Guyton and Hall Textbook of Medical Physiology*. Elsevier, 13 edition.

[49] Hepworth, D. G., Steven-fountain, A., Bruce, D. M., and Vincent, J. F. V. (2001). Affine versus non-affine deformation in soft biological tissues, measured by the reorientation and stretching of collagen fibres through the thickness of compressed porcine skin. *Journal of Biomechanics*, 34(3):341–346.

[50] Hill, A. V. (1938). The heat of shortening and the dynamic constants of muscle. *Proceedings of the Royal Society of London B: Biological Sciences*, 126(843):136–195.

[51] Holt, J. P., Allensworth, J., Diana, J., Collins, D., and Kines, H. (1957). Regulation of the degree of emptying of the left ventricle by the force of ventricular contraction. *Circulation Research*, 5(3):281–287.

[52] Holzapfel, G. A. (2000). *Nonlinear solid mechanics*. John Wiley and Sons, Chichester.

[53] Holzapfel, G. A. and Ogden, R. W. (2009). Constitutive modelling of passive myocardium: a structurally based framework for material characterization. *Philosophical Transactions of the Royal Society of London A: Mathematical, Physical and Engineering Sciences*, 367(1902):3445–3475.

[54] Hopkins, G. (2017). Growth, modelling and remodelling of cardiac tissue: A multiphase approach. Master's thesis, University of Cape Town.

[55] Humphrey, J. D. and McCulloch, A. D. (2003). The cardiovascular system - anatomy, physiology and cell biology. In *Biomechanics of Soft Tissue in Cardiovascular Systems*, pages 1–14. Springer Vienna.

[56] Humphrey, J. D. and Yin, F. C. P. (1987). On constitutive relations and finite deformations of passive cardiac tissue: I. a pseudostrain-energy function. *Journal of Biomechanical Engineering*, 109:298–304.

[57] Humphrey, J. D. and Yin, F. C. P. (1989). Constitutive relations and finite deformations of passive cardiac tissue ii: stress analysis in the left ventricle. *Circulation Research*, 65(3):805–817.

[58] Huxley, A. F. (1957). Muscle structure and theories of contraction. *Progress in biophysics and biophysical chemistry*, 7:255–318.

[59] Janz, R. F. and Grimm, A. F. (1972). Finite-element model for the mechanical behavior of the left ventricle. *Circulation Research*, 30(2):244–252.

[60] Johnston, P. R. (2003). A cylindrical model for studying subendocardial ischaemia in the left ventricle. *Mathematical Biosciences*, 186(1):43–61.

[61] Jung, B., Markl, M., Föll, D., and Hennig, J. (2006). Investigating myocardial motion by mri using tissue phase mapping. *European Journal of Cardiothoracic Surgery*, 29:S150–S157.

[62] Katz, A. M. (2011). *Physiology of the Heart*. Lippincott Williams and Wilkins.

[63] Kelly, P. (2018). *Solid Mechanics Lecture Notes*. The University of Auckland, Available from http://homepages.engineering.auckland.ac.nz/∼pkel015/SolidMechanicsBooks/.

[64] Kerckhoffs, R. (2003). *Depolarization wave and mechanics in the paced heart: model and experiment*. PhD thesis, Tehcnical University of Eindhoven.

[65] Klabunde, R. (2011). *Cardiovascular Physiology Concepts*. Medicine Series. Wolters Kluwer Health.

[66] Krasny, W., Magoariec, H., Morin, C., and Avril, S. (2018). Kinematics of collagen fibers in carotid arteries under tension-inflation loading. *Journal of the Mechanical Behavior of Biomedical Materials*, 77:718–726.

[67] Lai, W. M., Rubin, D., and Krempl, E. (2010). *Introduction to continuum mechanics*. Butterworth-Heinemann, Amsterdam.

[68] Lake, S. P., Cortes, D. H., Kadlowec, J. A., Soslowsky, L. J., and Elliott, D. M. (2012). Evaluation of affine fiber kinematics in human supraspinatus tendon using quantitative projection plot analysis. *Biomechanics and Modeling in Mechanobiology*, 11(1):197–205.

[69] Laks, M. M., Nisenson, M. J., and Swan, H. J. C. (1967). Myocardial cell and sarcomere lengths in the normal dog heart. *Circulation Research*, 21:671–678.

[70] Lanzer, P. and Topol, E. (2002). *Pan Vascular Medicine: Integrated Clinical Management*. Springer, Berlin.

[71] Lee, J. D., Chen, Y., and Wang, X. (2010). Extending micromorphic theory to atomic scale. In *Mechanics of Generalized Continua: One Hundred Years After the Cosserats*, pages 109–117. Springer, New York.

[72] LeGrice, I. J., Smaill, B. H., Chai, L. Z., Edgar, S. G., Gavin, J. B., and Hunter, P. J. (1995a). Laminar structure of the heart: Ventricular myocyte arrangement and connective tissue architecture in the dog. *American Journal of Physiology*, 269:H571–H582.

[73] LeGrice, I. J., Takayama, Y., and Covell, J. W. (1995b). Transverse shear along myocardial cleavage planes provides a mechanism for normal systolic wall thickening. *Circulation Research*, 77(1):182–193.

[74] Lin, D. H. S. and Yin, F. C. P. (1998). A multiaxial constitutive law for mammalian left ventricular myocardium in steady-state barium contracture or tetanus. *Journal of Biomechanical Engineering*, 120.

[75] Logan, D. L. (2011). *A First Course in the Finite Element Method*. Cengage Learning.

[76] Lopez-Perez, A., Sebastian, R., and Ferrero, J. M. (2015). Three-dimensional cardiac computational modelling: methods, features and applications. *Biomedical Engineering Online*, 14.

[77] Madeo, A. (2015). *Generalized Continuum Mechanics and Engineering Applications*. Elsevier Science.

[78] Marieb, E. and Hoehn, K. (2013). *Human Anatomy & Physiology*. Pearson.

[79] McHale, P. A. and Greenfield, J. C. (1973). Evaluation of several geometric models for estimation of left ventricular circumferential wall stress. *Circulation Research*, 33(3):303–312.

[80] Mindlin, R. D. (1964). Micro structure in linear elasticity. *Archive for Rational Mechanics and Analysis*, 16:51–78.

[81] Mirsky, I. (1973). Ventricular and arterial wall stresses based on large deformation analyses. *Biophysical Journal*, 13(11).

[82] Nakatani, S. (2011). Left ventricular rotation and twist: Why should we learn? *Journal of Cardiovascular Ultrasound*, 19(1):1–6.

[83] Nardinocchi, P. and Teresi, L. (2007). On the active response of soft living tissues. *Journal of Elasticity*, 88(1):27–39.

[84] Nash, M. P. and Hunter, P. J. (2000). Computational mechanics of the heart. *Journal of Elasticity and the Physical Science of Solids*, 61(1):113–141.

[85] Netter, F. H. (2014). *Atlas of Human Anatomy*. Elsevier, 6 edition.

[86] Nikou, A., Dorsey, S. M., McGarvey, J. R., Gorman, J. H., Burdick, J. A., Pilla, J. J., Gorman, R. C., and Wenk, J. F. (2015). Computational modeling of healthy myocardium in diastole. *Annals of Biomedical Engineering*, 44(4):980–992.

[87] O'Donnell, L. J. and Westin, C. F. (2011). An introduction to diffusion tensor image analysis. *Neurosurgery Clinics of North America*, 22(2):185–196.

[88] Ordas, S., Oubel, E., Leta, R., Carreras, F., and Frangi, A. F. (2007). A statistical shape model of the heart and its application to model-based segmentation. *Proceedings of SPIE - The International Society for Optical Engineering*, 6511.

[89] Ovalle, W. K. and Nahirney, P. C. (2013). *Netter's essential histology*. Elsevier, Philadelphia.

[90] Park, H. C. and Lakes, R. S. (1986). Cosserat micromechanics of human bone: Strain redistribution by a hydration sensitive constituent. *Journal of Biomechanics*, 19(5):385–397.

[91] Peyrat, J. M., Sermesant, M., Pennec, X., Delingette, H., Xu, C., McVeigh, E. R., and Ayache, N. (2007). A computational framework for the statistical analysis of cardiac diffusion tensors: Application to a small database of canine hearts. *IEEE Transactions on Medical Imaging*, 26:1500–1514.

[92] Pezzuto, S., Ambrosi, D., and Quarteroni, A. (2014). An orthotropic active–strain model for the myocardium mechanics and its numerical approximation. *European Journal of Mechanics - A/Solids*, 48:83 – 96.

[93] Pluijmert, M., Delhaas, T., de la Parra, A. F., Kroon, W., Prinzen, F. W., and Bovendeerd, P. H. M. (2017). Determinants of biventricular cardiac function: a mathematical model study on geometry and myofiber orientation. *Biomechanics and Modeling in Mechanobiology*, 16(2):721–729.

[94] Pullan, A. J., Cheng, L. K., and Buist, M. L. (2005). *Mathematically Modelling the Electrical Activity of the Heart: From Cell to Body Surface and Back Again*. World Scientific.

[95] Quarteroni, A., Lassila, T., Rossi, S., and Ruiz-Baier, R. (2017). Integrated heart – coupling multiscale and multiphysics models for the simulation of the cardiac function. *Computer Methods in Applied Mechanics and Engineering*, 314:345 – 407.

[96] Rademakers, F. E., Buchalter, M. B., Rogers, W. J., Zerhouni, E. A., Weisfeldt, M. L., Weiss, J. L., and Shapiro, E. P. (1992). Dissociation between left ventricular untwisting and filling. accentuation by catecholamines. *Circulation*, 85:1572–1581.

[97] Rama, R. R. (2017). *Proper Orthogonal Decomposition with Interpolation-based Real-time Modelling of the Heart*. PhD thesis, University of Cape Town.

[98] Reddy, J. N. (2013). *An Introduction to Continuum Mechanics*. Cambridge University Press, 2 edition.

[99] Rice, J. J. and de Tombe, P. P. (2004). Approaches to modeling crossbridges and calcium-dependent activation in cardiac muscle. *Progress in Biophysics and Molecular Biology*, 85(2):179–195.

[100] Rice, J. J., Wang, F., Bers, D. M., and de Tombe, P. P. (2008). Approximate model of cooperative activation and crossbridge cycling in cardiac muscle using ordinary differential equations. *Biophysical Journal*, 95(5):2368–2390.

[101] Robinson, T. F., Geraci, M. A., Sonnenblick, E. H., and Factor, S. M. (1988). Coiled perimysial fibers of papillary muscle in rat heart: Morphology, distribution, and changes in configuration. *Circulation Research*, 63(3):577–592.

[102] Rodbard, S., Williams, F., and Williams, C. (1959). The spherical dynamics of the heart (myocardial tension, oxygen consumption, coronary blood flow and efficiency. *American Heart Journal*, 57(3):348–360.

[103] Rodriguez, E. K., Hunter, W. C., Royce, M. J., Leppo, M. K., Douglas, A. S., and Weisman, H. F. (1992). A method to reconstruct myocardial sarcomere lengths and orientations at transmural sites in beating canine hearts. *American Journal of Physiology-Heart and Circulatory Physiology*, 263(1):H293–H306.

[104] Rogers, W. J., Shapiro, E. P., Weiss, J. L., Buchalter, M. B., Rademakers, F. E., Weisfeldt, M. L., and Zerhouni, E. A. (1991). Quantification of and correction for left ventricular systolic long-axis shortening by magnetic resonance tissue tagging and slice isolation. *Circulation*, 84(2):721–731.

[105] Rosenberg, J. and Cimrman, R. (2003). Microcontinuum approach in biomechanical modeling. *Mathematics and Computers in Simulation*, 61(3):249–260.

[106] Sachse, F. B. (2004). *Computational Cardiology: Modeling of Anatomy, Electrophysiology, and Mechanics*. Lecture Notes in Computer Science. Springer.

[107] Sack, K. (2014). Biological tissue mechanics with fibres modelled as one dimensional cosserat continua. applications to cardiac tissue in healthy and diseased states. Master's thesis, University of Cape Town.

[108] Sack, K. L., Skatulla, S., and Sansour, C. (2016). Biological tissue mechanics with fibres modelled as one-dimensional cosserat continua. applications to cardiac tissue. *International Journal of Solids and Structures*, 81:84–94.

[109] Sansour, C., Skatulla, S., and Zbib, H. (2010). A formulation for the micromorphic continuum at finite inelastic strains. *International Journal of Solids and Structures*, 47(11):1546–1554.

[110] Sengupta, P. P., Korinek, J., Belohlavek, M., Narula, J., Vannan, M. A., Jahangir, A., and Khandheria, B. K. (2006). Left ventricular structure and function. *Journal of the American College of Cardiology*, 48(10):1988–2001.

[111] Skatulla, S. and Sansour, C. (2016). On a path-following method for non-linear solid mechanics with applications to structural and cardiac mechanics subject to arbitrary loading scenarios. *International Journal of Solids and Structures*, 96:181–191.

[112] Soares, J. M., Marques, P., Alves, V., and Sousa, N. (2013). A hitchhiker's guide to diffusion tensor imaging. *Frontiers in Neuroscience*, 7.

[113] Sommer, G., Schriefl, A. J., Andrä, M., Sacherer, M., Viertler, C., Wolinski, H., and Holzapfel, G. A. (2015). Biomechanical properties and microstructure of human ventricular myocardium. *Acta Biomaterialia*, 24:172–192.

[114] Streeter, D. D. and Hanna, W. T. (1973). Engineering mechanics for successive states in canine left ventricular myocardium i. cavity and wall geometry. *Circulation Research*, 33(6):639–655.

[115] Streeter, D. D., Spotnitz, H. M., Patel, D. P., Ross, J., and Sonnenblick, E. H. (1969). Fiber orientation in the canine left ventricle during diastole and systole. *Circulation Research*, 24(3):339–347.

[116] Streeter, D. D., Vaishnav, R. N., Patel, D. J., Spotnitz, H. M., Ross, J., and Sonnenblick, E. H. (1970). Stress distribution in the canine left ventricle during diastole and systole. *Biophysical Journal*, 10(4):345–363.

[117] Taber, L. A. and Perucchio, R. (2000). Modeling heart development. *Journal of Elasticity and the Physical Science of Solids*, 61(1):165–197.

[118] Thurieau, N., Jehl, J. P., Nijwa, K. R., Tran, N., and Maureira, P. (2017). Modeling heart tissue as a micromorphic medium: a numerical investigation. *Journal of Mechanics in Medicine and Biology*, 17(5).

[119] Tözeren, A. (1985). Continuum rheology of muscle contraction and its application to cardiac contractility. *Biophysical Journal*, 47(3):303–309.

[120] Trayanova, N. A. (2011). Whole-heart modeling applications to cardiac electrophysiology and electromechanics. *Circulation research*, 108(1):113–128.

[121] Ubbink, S. W., Bovendeerd, P. H., Delhaas, T., Arts, T., and Van de Vosse, F. N. (2006). Towards model-based analysis of cardiac mr tagging data: Relation between left ventricular shear strain and myofiber orientation. *Medical Image Analysis*, 10.

[122] Usyk, T. P., Mazhari, R., and McCulloch, A. D. (2000). Effect of laminar orthotropic myofiber architecture on regional stress and strain in the canine left ventricle. *Journal of Elasticity and the Physical Science of Solids*, 61(1):143–164.

[123] Van Campen, D. H., Huyghe, J. M., Bovendeerd, P. H., and Arts, M. G. (1994). Biomechanics of the heart muscle. *European Journal of Mechanics. A, Solids*, 13(4):19–41.

[124] Van de Vosse, F. N. and Stergiopulos, N. (2011). Pulse wave propagation in the arterial tree. *Annual Review of Fluid Mechanics*, 43(1):467–499.

[125] Van Den Broek, J. H. and Van Den Broek, M. H. (1979). Application of an ellipsoidal heart model in the studying of left ventricular contractions. *Journal of Biomechanics*, 13:493–503.

[126] Van Den Broek, J. H. and Van Der Gon, J. J. (1980). A model study of isovolumic and non-isovolumic left ventricular contractions. *Journal of Biomechanics*, 13:77–87.

[127] Van Heuningen, R., Rijnsburger, W. H., and Ter Keurs, H. E. (1982). Sarcomere length control in striated muscle. *American Journal of Physiology*, 242(3):H411–H420.

[128] Vinson, C. A., Gibson, D. G., and Yettram, A. L. (1979). Analysis of left ventricular behaviour in diastole by means of finite element method. *British Heart Journal*, 41(1):60–67.

[129] von Hoegen, M., Skatulla, S., and Schröder, J. (2017). A generalized micromorphic approach accounting for variation and dispersion of preferred material directions. *Computers and Structures*.

[130] Walker, J. C., Ratcliffe, M., Zhang, P., Wallace, A. W., Fata, B., Hsu, E. W., Saloner, D., and Guccione, J. M. (2005). Mri-based finite-element analysis of left ventricular aneurysm. *American journal of physiology. Heart and circulatory physiology*, 289:H692–H700.

[131] Wang, H. M., Luo, X. Y., Gao, H., Ogden, R. W., Griffith, B. E., Berry, C., and Wang, T. J. (2014). A modified holzapfel-ogden law for a residually stressed finite strain model of the human left ventricle in diastole. *Biomechanics and Modeling in Mechanobiology*, 13(1):99–113.

[132] Westerhof, N., Lankhaar, J. W., and Westerhof, B. E. (2009). The arterial windkessel. *Medical & Biological Engineering & Computing*, 47(2):131–141.

[133] Wong, A. Y. K. (1973). Myocardial mechanics: Application of sliding-filament theory to isovolumic concentration of the left ventricle. *Journal of Biomechanics*, 6(5):565–581.

[134] Wong, J., Göktepe, S., and Kuhl, E. (2013). Computational modeling of chemo-electro-mechanical coupling: A novel implicit monolithic finite element approach. *International journal for numerical methods in biomedical engineering*, 29:1104–1133.

[135] Wong, J. and Kuhl, E. (2014). Generating fibre orientation maps in human heart models using poisson interpolation. *Computer Methods in Biomechanics and Biomedical Engineering*, 17(11):1217–1226.

[136] Wriggers, P. (2008). *Nonlinear Finite Element Methods*. Springer, Berlin.

[137] Yamada, H. and Tanaka, E. (2000). Active stress models of cardiac muscle, smooth muscle and skeletal muscle. In *Human Biomechanics and Injury Prevention*, pages 161–166. Springer Japan.

[138] Yang, J. F. P. and Lakes, R. S. (1982). Experimental study of micropolar and couple stress elasticity in compact bone in bending. *Journal of Biomechanics*, 15(2):91–98.

[139] Yin, F. C. P., Strumpf, R. K., Chew, P. H., and Zeger, S. L. (1987). Quantification of the mechanical properties of noncontracting canine myocardium under simultaneous biaxial loading. *Journal of Biomechanics*, 20:577–589.

[140] Young, A. A., Legrice, I. J., Young, M. A., and Smaill, B. H. (1998). Extended confocal microscopy of myocardial laminae and collagen network. *Journal of Microscopy*, 192:139–150.

Appendix A

Finite Element Method in Voigt Notation

In Chapter 3 we discussed the finite element method as it relates to non-linear elastic problems. In this chapter we derive the finite element stiffness matrix and the force vectors in Voigt notation. Voigt notation exploits the symmetry of tensors and offers a more compact form of writing tensors. This chapter is heavily based on the work of Wriggers [136].

A.1 Discretisation of the Weak Form

Consider the weak formulation,

$$\int_{\mathcal{B}_0} \mathbf{S} : \delta\mathbf{E}\, \mathrm{d}V - \int_{\partial\mathcal{B}_0} \bar{\mathbf{t}}^{(\mathbf{n})} \cdot \delta\mathbf{u}\, \mathrm{d}A - \int_{\mathcal{B}_0} \rho_0 \mathbf{b} \cdot \delta\mathbf{u}\, \mathrm{d}V = 0\,. \tag{A.1}$$

Since $\mathbf{S}$ and $\mathbf{E}$ are symmetric tensors, both of these tensors contain only six independent components. Using Voigt notation, the second Piola-Kirchhoff stress is

$$\bar{\mathbf{S}} = [S_{11}, S_{22}, S_{33}, S_{12}, S_{23}, S_{13}]^T \tag{A.2}$$

and similarly

$$\delta\bar{\mathbf{E}} = [E_{11}, E_{22}, E_{33}, 2E_{12}, 2E_{23}, 2E_{13}]^T\,, \tag{A.3}$$

where the bar indicates Voigt notation.

We approximate the displacement as well as the gradient of the displacement with the following,

$$\mathbf{u}_{exact} \approx \sum_{I=1}^{n} N^I(\mathbf{X})\mathbf{u}^I\,, \qquad \mathrm{Grad}\mathbf{u}_{exact} \approx \sum_{I=1}^{n} \mathbf{u}^I \otimes \frac{\partial N^I(\mathbf{X})}{\partial \mathbf{X}}\,, \tag{A.4}$$

where $\mathbf{u}^I$ are the unknown displacements at the nodes of an element with n nodes and N^I are the shape functions. With the Galerkin formulation, the virtual displacement is approximated using

the same shape functions, that is

$$\delta\mathbf{u}_{exact} \approx \sum_{I=1}^{n} N^I(\mathbf{X})\delta\mathbf{u}^I \,, \qquad \text{Grad}\delta\mathbf{u}_{exact} \approx \sum_{I=1}^{n} \delta\mathbf{u}^I \otimes \frac{\partial N^I(\mathbf{X})}{\partial \mathbf{X}} \,. \tag{A.5}$$

Using the definition of the Green-Lagrange strain tensor, the virtual strain $\delta\mathbf{E}$ in index notation is written as

$$\delta E_{ik} = \frac{1}{2}\left(F_{ji}\frac{\partial \delta u_j}{\partial X_k} + \frac{\partial \delta u_j}{\partial X_i}F_{jk}\right) . \tag{A.6}$$

If we introduce the shape functions, we obtain the following approximation of the strain tensor,

$$\delta E_{ik} \approx \sum_{I=1}^{n} \frac{1}{2}\left(F_{ji}\frac{\partial N^I}{\partial X_k} + \frac{\partial N^I}{\partial X_i}F_{jk}\right)\delta u_{Ij} \,. \tag{A.7}$$

We use the previous expression to write the virtual strain in Voigt notation as

$$\delta\bar{\mathbf{E}} = \begin{bmatrix} \delta E_{11} \\ \delta E_{22} \\ \delta E_{33} \\ 2\delta E_{12} \\ 2\delta E_{23} \\ 2\delta E_{13} \end{bmatrix} = \sum_{I=1}^{n} \mathbf{B}^I \delta\mathbf{u}^I \,, \tag{A.8}$$

where $\mathbf{B}^I$ is given by

$$\mathbf{B}_I = \begin{bmatrix} F_{11}\frac{\partial N^I}{\partial X_1} & F_{21}\frac{\partial N^I}{\partial X_1} & F_{31}\frac{\partial N^I}{\partial X_1} \\ F_{12}\frac{\partial N^I}{\partial X_2} & F_{22}\frac{\partial N^I}{\partial X_2} & F_{32}\frac{\partial N^I}{\partial X_2} \\ F_{13}\frac{\partial N^I}{\partial X_3} & F_{22}\frac{\partial N^I}{\partial X_3} & F_{32}\frac{\partial N^I}{\partial X_3} \\ F_{11}\frac{\partial N^I}{\partial X_2} + F_{12}\frac{\partial N^I}{\partial X_1} & F_{21}\frac{\partial N^I}{\partial X_2} + F_{22}\frac{\partial N^I}{\partial X_1} & F_{31}\frac{\partial N^I}{\partial X_2} + F_{32}\frac{\partial N^I}{\partial X_1} \\ F_{12}\frac{\partial N^I}{\partial X_3} + F_{13}\frac{\partial N^I}{\partial X_2} & F_{22}\frac{\partial N^I}{\partial X_3} + F_{23}\frac{\partial N^I}{\partial X_2} & F_{32}\frac{\partial N^I}{\partial X_3} + F_{33}\frac{\partial N^I}{\partial X_2} \\ F_{11}\frac{\partial N^I}{\partial X_3} + F_{13}\frac{\partial N^I}{\partial X_1} & F_{21}\frac{\partial N^I}{\partial X_3} + F_{23}\frac{\partial N^I}{\partial X_1} & F_{31}\frac{\partial N^I}{\partial X_3} + F_{33}\frac{\partial N^I}{\partial X_1} \end{bmatrix} . \tag{A.9}$$

Using Voigt notation, we can rewrite the weak form in Equation (A.1) as

$$\int_{\mathcal{B}_0} \delta\bar{\mathbf{E}}^T\bar{\mathbf{S}}\,\mathrm{d}V - \int_{\partial\mathcal{B}_0} \delta\mathbf{u}^T\bar{\mathbf{t}}^{(\mathbf{n})}\,\mathrm{d}A - \int_{\mathcal{B}_0}\rho_0\delta\mathbf{u}^T\mathbf{b}\,\mathrm{d}V = 0 \,. \tag{A.10}$$

Discretising the above expression, we arrive at

$$\bigcup_{e=1}^{n_e}\sum_{I=1}^{n}\delta\mathbf{u}^{IT}\int_{\Omega_e}\mathbf{B}^{IT}\bar{\mathbf{S}}\,\mathrm{d}\Omega - \bigcup_{r=1}^{n_r}\sum_{I=1}^{m}\delta\mathbf{u}^{IT}\int_{\Gamma_r}N^I\bar{\mathbf{t}}^{(\mathbf{n})}\,\mathrm{d}\Gamma - \bigcup_{e=1}^{n_e}\sum_{I=1}^{n}\delta\mathbf{u}^{IT}\int_{\Omega_e}\rho_0 N^I\mathbf{b}\,\mathrm{d}\Omega = 0 \,, \tag{A.11}$$

where $\bigcup$ denotes an assembly process. As in Chapter 3, n_e is the number of elements, Ω_e is the e^{th} element, n_r is the number of boundaries with traction loads and m is the number of nodes on the traction surface Γ_r.

Because the virtual displacement is arbitrary we can write

$$\bigcup_{e=1}^{n_e}\sum_{I=1}^{n}\int_{\Omega_e}\mathbf{B}^{I^T}\bar{\mathbf{S}}\,\mathrm{d}\Omega-\bigcup_{r=1}^{n_r}\sum_{I=1}^{m}\int_{\Gamma_e}N^I\bar{\mathbf{t}}^{(\mathbf{n})}\,\mathrm{d}\Gamma-\bigcup_{e=1}^{n_e}\sum_{I=1}^{n}\int_{\Omega_e}\rho_0 N^I\mathbf{b}\,\mathrm{d}\Omega=0\,. \tag{A.12}$$

The discretised weak formulation in Equation (A.12) is a set of non-linear algebraic equations that need to be solved using an iterative scheme.

A.2 Linearisation of the Weak Formulation

To find an approximate solution to the weak formulation we first consider the residual G,

$$\mathrm{G}(\mathbf{u})=\int_{\Omega_0}\mathbf{S}:\delta\mathbf{E}\,\mathrm{d}V-\int_{\partial\Omega_0}\bar{\mathbf{t}}^{(\mathbf{n})}\cdot\delta\mathbf{u}\,\mathrm{d}A-\int_{\Omega_0}\rho_0\mathbf{b}\cdot\delta\mathbf{u}\,\mathrm{d}V=0\,. \tag{A.13}$$

The objective is to find $\mathbf{u}$ such that the residual is minimised. To find a solution that satisfies the above, we consider a first-order Taylor expansion of the residual,

$$\mathrm{G}(\mathbf{u}_{k+1})=\mathrm{G}(\mathbf{u}_k)+\frac{\partial\mathrm{G}(\mathbf{u}_k)}{\partial\mathbf{u}}\cdot\Delta\mathbf{u}_k=\mathrm{G}(\mathbf{u}_k)+\Delta\mathrm{G}_k\,, \tag{A.14}$$

where $\Delta\mathbf{u}$ is the displacement increment, k the current iteration step and ΔG is the variation in the residual. The updated displacement is the sum of the current displacement and the displacement increment, i.e.

$$\mathbf{u}_{k+1}=\mathbf{u}_k+\Delta\mathbf{u}_k\,. \tag{A.15}$$

If we assume that the traction and body forces are conservative, i.e. do not depend on the displacement, then the last two terms in G($\mathbf{u}$) are independent of $\Delta\mathbf{u}$ and the variation in the residual is given as

$$\Delta\mathrm{G}=\frac{\partial\mathrm{G}(\mathbf{u})}{\partial\mathbf{u}}\cdot\Delta\mathbf{u}\;\;=\;\;\int_{\Omega_0}\Delta\mathbf{S}:\delta\mathbf{E}\,\mathrm{d}V+\int_{\Omega_0}\mathbf{S}:\Delta\delta\mathbf{E}\,\mathrm{d}V\,, \tag{A.16}$$

where $\Delta\delta\mathbf{E}=\frac{\partial\delta\mathbf{E}}{\partial\mathbf{u}}\Delta\mathbf{u}$ and $\Delta\mathbf{S}=\frac{\partial\mathbf{S}}{\partial\mathbf{u}}\Delta\mathbf{u}$ are the variations in the virtual strain and the stress respectively. Again using Voigt notation, we write the integrand of the first term in Equation (A.16) as

$$\Delta\mathbf{S}:\delta\mathbf{E}=\Delta\bar{\mathbf{S}}\cdot\delta\bar{\mathbf{E}}=(\bar{\mathbf{D}}\Delta\bar{\mathbf{E}})\cdot\delta\bar{\mathbf{E}}=\delta\bar{\mathbf{E}}^T(\bar{\mathbf{D}}\Delta\bar{\mathbf{E}})\,, \tag{A.17}$$

where the bar denotes Voigt notation and $\bar{\mathbf{D}}$ is the matrix form of the fourth-order constitutive tensor $\mathbb{D}=\frac{\partial\mathbf{S}}{\partial\mathbf{E}}$. Discretising the above and using Equation (A.9), we have that

$$\Delta\bar{\mathbf{S}}\cdot\delta\bar{\mathbf{E}}\approx\sum_{I=1}^{n}\sum_{J=1}^{n}(\bar{\mathbf{D}}\mathbf{B}^I\Delta\mathbf{u}^I)\cdot(\mathbf{B}^J\delta\mathbf{u}^J)=\sum_{I=1}^{n}\sum_{J=1}^{n}(\delta\mathbf{u}^{I^T}\mathbf{B}^{I^T})(\bar{\mathbf{D}}\mathbf{B}^J\Delta\mathbf{u}^J)\,. \tag{A.18}$$

The integrand of the second term in Equation (A.16) can be written as

$$\begin{aligned}\mathbf{S} : \Delta\delta\mathbf{E} = \mathbf{S} : \frac{1}{2}\left(\frac{\partial\Delta\mathbf{u}}{\partial\mathbf{X}}^T\frac{\partial\delta\mathbf{u}}{\partial\mathbf{X}} + \frac{\partial\Delta\mathbf{u}}{\partial\mathbf{X}}\frac{\partial\delta\mathbf{u}}{\partial\mathbf{X}}^T\right) &= \mathbf{S} : \left(\frac{\partial\Delta\mathbf{u}}{\partial\mathbf{X}}^T\frac{\partial\delta\mathbf{u}}{\partial\mathbf{X}}\right) \\ &= \frac{\partial\Delta\mathbf{u}}{\partial\mathbf{X}}\mathbf{S} : \frac{\partial\delta\mathbf{u}}{\partial\mathbf{X}} \\ &= \underbrace{(\Delta\mathbf{u}\otimes\nabla_X)\mathbf{S}}_{\mathbf{A}} : (\underbrace{\delta\mathbf{u}}_{\mathbf{a}}\otimes\underbrace{\nabla_X}_{\mathbf{b}}) \\ &= \delta\mathbf{u}\cdot(\Delta\mathbf{u}\otimes\nabla_X)\mathbf{S}\nabla_X\,, \end{aligned} \tag{A.19}$$

where we have utilised the definition of the Green-Lagrange strain tensor and the fact that the scalar product of a symmetric and a skew-symmetric tensor is zero. We also made use of the rule $\mathbf{A} : \mathbf{a}\otimes\mathbf{b} = \mathbf{a}\cdot\mathbf{A}\mathbf{b}$. With the shape function approximations, we obtain

$$\mathbf{S} : \Delta\delta\mathbf{E} \approx \sum_{I=1}^{n}\sum_{J=1}^{n}\delta\mathbf{u}^I\cdot\left(\Delta\mathbf{u}^J\otimes\frac{\partial N^J}{\partial\mathbf{X}}\right)\mathbf{S}\frac{\partial N^I}{\partial\mathbf{X}} = \sum_{I=1}^{n}\sum_{J=1}^{n}\delta\mathbf{u}^{I^T}\left(\underbrace{\Delta\mathbf{u}^J}_{\mathbf{a}}\otimes\underbrace{\frac{\partial N^J}{\partial\mathbf{X}}}_{\mathbf{b}}\right)\underbrace{\mathbf{S}\frac{\partial N^I}{\partial\mathbf{X}}}_{\mathbf{c}}\,. \tag{A.20}$$

We apply the rule $(\mathbf{a}\otimes\mathbf{b})\mathbf{c} = (\mathbf{c}\cdot\mathbf{b})\mathbf{a}$ to obtain the following,

$$\mathbf{S} : \Delta\delta\mathbf{E} \approx \sum_{I=1}^{n}\sum_{J=1}^{n}\delta\mathbf{u}^{I^T}\left(\left(\mathbf{S}\frac{\partial N^I}{\partial\mathbf{X}}\right)\cdot\frac{\partial N^J}{\partial\mathbf{X}}\right)\Delta\mathbf{u}^J = \sum_{I=1}^{n}\sum_{J=1}^{n}\delta\mathbf{u}^{I^T}\left(\left(\frac{\partial N^I}{\partial\mathbf{X}}\right)^T\mathbf{S}\frac{\partial N^J}{\partial\mathbf{X}}\right)\Delta\mathbf{u}^J\,. \tag{A.21}$$

Substituting Equations (A.18) and (A.21) back into Equation (A.16), the variation in the residual becomes

$$\Delta\mathrm{G}_k = \bigcup_{e=1}^{n_e}\sum_{I=1}^{n}\sum_{J=1}^{n}\int_{\Omega_e}\delta\mathbf{u}^{I^T}\mathbf{B}^{I^T}\bar{\mathbf{D}}\mathbf{B}^J\Delta\mathbf{u}^J\,\mathrm{d}\Omega + \bigcup_{e=1}^{n_e}\sum_{I=1}^{n}\sum_{J=1}^{n}\int_{\Omega_e}\delta\mathbf{u}^{I^T}\left(\left(\frac{\partial N^I}{\partial\mathbf{X}}\right)^T\mathbf{S}\frac{\partial N^J}{\partial\mathbf{X}}\right)\Delta\mathbf{u}^J\,\mathrm{d}\Omega\,. \tag{A.22}$$

From Equation (A.11) we know that

$$\mathrm{G}(\mathbf{u}_k) = \bigcup_{e=1}^{n_e}\sum_{I=1}^{n}\delta\mathbf{u}^{I^T}\int_{\Omega_e}\mathbf{B}^{I^T}\bar{\mathbf{S}}\,\mathrm{d}\Omega - \bigcup_{r=1}^{n_r}\sum_{I=1}^{m}\delta\mathbf{u}^{I^T}\int_{\Gamma_r}N_I\bar{\mathbf{t}}^{(\mathbf{n})}\,\mathrm{d}\Gamma - \bigcup_{e=1}^{n_e}\sum_{I=1}^{n}\delta\mathbf{u}^{I^T}\int_{\Omega_e}\rho_0 N^I\mathbf{b}\,\mathrm{d}\Omega = 0\,. \tag{A.23}$$

Finally, substitution of the above into Equation (A.14) leads to

$$\begin{aligned}\mathrm{G}(\mathbf{u}_{k+1}) = \delta\mathbf{u}^{I^T}\underbrace{\left\{\bigcup_{e=1}^{n_e}\sum_{I=1}^{n}\int_{\Omega_e}\mathbf{B}^{I^T}\bar{\mathbf{S}}\,\mathrm{d}\Omega\right\}}_{\mathbf{F}_{int}} - \delta\mathbf{u}^{I^T}\underbrace{\left\{\bigcup_{r=1}^{n_r}\sum_{I=1}^{m}\int_{\Gamma_r}N^I\bar{\mathbf{t}}^{(\mathbf{n})}\,\mathrm{d}\Gamma + \bigcup_{n=1}^{n_e}\sum_{I=1}^{n}\int_{\Omega_e}\rho_0 N^I\mathbf{b}\,\mathrm{d}\Omega\right\}}_{\mathbf{F}_{ext}} \\ + \delta\mathbf{u}^{I^T}\underbrace{\left\{\bigcup_{e=1}^{n_e}\sum_{I=1}^{n}\sum_{J=1}^{n}\int_{\Omega_e}\mathbf{B}^{I^T}\bar{\mathbf{D}}\mathbf{B}^J\,\mathrm{d}\Omega + \bigcup_{e=1}^{n_e}\sum_{I=1}^{n}\sum_{J=1}^{n}\int_{\Omega_e}\left(\left(\frac{\partial N^I}{\partial\mathbf{X}}\right)^T\mathbf{S}\frac{\partial N^J}{\partial\mathbf{X}}\right)\mathbf{I}\,\mathrm{d}\Omega\right\}}_{\mathbf{K}}\Delta\mathbf{u}^J\,. \end{aligned} \tag{A.24}$$

In Equation (A.24) we have indicated the internal force vector $\mathbf{F}_{int}$, the external force vector $\mathbf{F}_{ext}$ and the stiffness matrix $\mathbf{K}$. In terms of the stiffness matrix and the force vectors, the residual is given as

$$\mathrm{G}(\mathbf{u}_{k+1}) = \delta\mathbf{u}^{I^T}\left(\mathbf{F}(\mathbf{u}_k)_{ext} - \mathbf{F}(\mathbf{u}_k)_{int} + \mathbf{K}(\mathbf{u}_k)\Delta\mathbf{u}^J\right). \tag{A.25}$$

Appendix B

Ethical Considerations

Ethical clearance for the use of the MRI scans was provided by the Faculty of Health Sciences, University of Cape Town.

UNIVERSITY OF CAPE TOWN
Faculty of Health Sciences
Human Research Ethics Committee

Room E53-46 Old Main Building
Groote Schuur Hospital
Observatory 7925
Telephone [021] 406 6626
Email: shuretta.thomas@uct.ac.za
Website: www.health.uct.ac.za/fhs/research/humanethics/forms

22 November 2018

HREC REF: 679/2018

Prof Ntobeko Ntusi
Cardiology
Medicine
J46.53

Dear Prof Ntusi

PROJECT TITLE: ACTIVE CONTRACTION OF THE LEFT VENTRICLE WITH CARDIAC TISSUE MODELLED AS A MICROMORPHIC MEDIUM (SUB-STUDY LINKED TO 554/2017 & R055/2015) (MSc Candidate - M. Kamper)

Thank you for submitting your study to the Faculty of Health Sciences Human Research Ethics Committee.

It is a pleasure to inform you that the HREC has **formally approved** the above-mentioned study.

Approval is granted for one year until the 30 November 2019.

Please submit a progress form, using the standardised Annual Report Form if the study continues beyond the approval period. Please submit a Standard Closure form if the study is completed within the approval period.
(Forms can be found on our website: www.health.uct.ac.za/fhs/research/humanethics/forms)

Please quote the HREC REF in all your correspondence.

Please note that the ongoing ethical conduct of the study remains the responsibility of the principal investigator.

Please note that for all studies approved by the HREC, the principal investigator **must** obtain appropriate institutional approval, where necessary, before the research may occur.

The HREC acknowledge that the student, Marina Kamper will also be involved in this study.

Yours sincerely

signature removed to avoid exposure online

PROFESSOR M BLOCKMAN
CHAIRPERSON, FHS HUMAN RESEARCH ETHICS COMMITTEE
Federal Wide Assurance Number: FWA00001637.
Institutional Review Board (IRB) number: IRB00001938

This serves to confirm that the University of Cape Town Human Research Ethics Committee complies to the Ethics Standards for Clinical Research with a new drug in patients, based on the Medical Research Council (MRC-SA), Food and Drug Administration (FDA-USA), International Convention on Harmonisation Good Clinical Practice (ICH GCP), South African Good Clinical Practice Guidelines (DoH 2006), based on the Association of the British Pharmaceutical Industry Guidelines (ABPI), and Declaration of Helsinki (2013) guidelines.
The Human Research Ethics Committee granting this approval is in compliance with the ICH Harmonised Tripartite Guidelines E6: Note for Guidance on Good Clinical Practice (CPMP/ICH/135/95) and FDA Code Federal Regulation Part 50, 56 and 312.